Modelling the interaction of X-rays with the Interstellar Medium

Margherita Molaro

München 2016

Modelling the interaction of X-rays with the Interstellar Medium

Margherita Molaro

Dissertation
an der Fakultät für Physik
der Ludwig–Maximilians–Universität
München

vorgelegt von
Margherita Molaro
aus Trieste

München, den 26.02.2016

Erstgutachter: Prof. Dr. Rashid Sunyaev
Zweitgutachter: Prof. Dr. Gerhard Börner
Tag der mündlichen Prüfung: 31.05.2016

Contents

List of Figures

List of Tables

Zusammenfassung

Die Wechselwirkung von Röntgenstrahlen aus diskreten Quellen mit dem interstellaren Medium (ISM), durch welches sie sich ausbreiten, führt zu charakteristischen Strahlungssignaturen im keV-Bereich. Diese Signaturen enthalten eine Fülle an Informationen, sowohl über die Gasstrukturen, die für die Modulation der Strahlung verantwortlich sind, als auch über die Röntgenquellen, die sie ursprünglich abstrahlten. Diese Arbeit veranschaulicht, wie die Untersuchung dieser beobachtbaren Signaturen auf eine Vielzahl astrophysikalischer Probleme (auf allen galaktischen Skalen) angewandt werden und wie sie sich gegenüber direkten Beobachtungen von Quellen oder ISM als vorteilhaft erweisen kann.

Zu diesem Zweck wiederholt Kapitel 1 die wichtigsten Wechselwirkungsprozesse zwischen Röntgenstrahlung und Materie, welche die Signaturen in der transmittierten Strahlung bestimmen.

Kapitel 2 zeigt, wie der ISM-Durchgang der Strahlung einer ausgesprochen leuchtkräftigen Klasse galaktischer Röntgenquellen, Röntgendoppelsterne (*X-ray binaries*, XBs), zur Emission aus dem sog. *Galactic Ridge* betragen sollte. Der Ursprung dieser Röntgenemission auf galaktischen Größenskalen stellte lange ein Problem in der Röntgenastrophysik dar. Das Studium dieses Beitrags kann, über die Verbesserung unseres Verständnisses der *Ridge*-Emission hinaus, als indirekte Methode zur Untersuchung allgemeiner Eigenschaften galaktischer XBs genutzt werden, deren direkte Beobachtung eine extreme Herausforderung darstellt.

Kapitel 3 erörtert den Effekt, den die Wechselwirkung mit Röntgenstrahlung auf das beleuchtete Gas selbst hat, indem der Beitrag durch Röntgenabsorption zur Aufheizung des Gases diskutiert, und dieser Beitrag mit anderen, häufiger berücksichtigten Heizquellen verglichen wird.

In Kapitel 4 wird diskutiert, wie das Studium der reflektierten Röntgenemission von *Giant Molecular Clouds* (GMCs) in der galaktischen Zentralregion, welche auf Beleuchtung durch helle *flares* von Sgr A*, dem supermassereichen Schwarzen Loch im Zentrum der Galaxie, folgen, genutzt werden kann um die interne Struktur dieser massereichen molekularen Komplexe zu untersuchen. Da gerade in dichten Regionen innerhalb von GMCs prästellare Kerne gebildet werden, ist das Verständnis ihrer Eigenschaften ein essentieller Schritt um den Prozess der Sternentstehung in Galaxien zu verstehen.

Kapitel 5 liefert eine Abschätzung der Verzerrungen, die im Spektrum des kosmischen Röntgenhintergrunds (extragalaktischen Ursprungs) zu erwarten sind, wenn dieser sich durch verschiedene Regionen des ISM ausbreitet.

Summary

The interaction between X-rays emitted by discrete sources and the interstellar medium (ISM) through which they propagate results in characteristic radiative signatures in the keV regime. These signatures contain a wealth of information both on the gas structures responsible for reprocessing the radiation, and on the X-ray sources that originally emitted them. This thesis illustrates how the study of these observational signatures can be applied to a wide range of astrophysical problems, on all galactic scales, and how it can prove to be advantageous over the direct observation of either sources or the ISM.

Towards this goal, Chapter 1 reviews the main processes of interaction between X-rays and matter, which determine the signatures imprinted on the reprocessed radiation.

Chapter 2 demonstrates how the reprocessing by the ISM of radiation produced by a particularly luminous class of Galactic X-ray sources, X-ray binaries (XBs), should be contributing towards the Galactic Ridge X-ray emission. The origin of this Galactic-scale X-ray emission has been a long-standing problem in X-ray astrophysics. The study of this contribution, beyond furthering our understanding of the origin of the Ridge emission, can be used as an indirect method for studying overall properties of the Galactic XB population, whose probe through direct observations is extremely challenging.

Chapter 3 discusses the effect that the interaction of X-ray radiation has on the gas it illuminates itself, by discussing the contribution that the absorption of X-rays has on the heating of the gas, and how this contribution compares to that of other, more commonly considered, sources of heating.

Chapter 4 discusses how the study of the reflected X-ray emission from Giant Molecular Clouds (GMCs) in the Galactic center region, following illumination by past, bright flares of Sgr A*, the supermassive black hole at the centre of the Galaxy, can be used to study the internal structure of these massive molecular complexes. As it is in dense regions inside GMCs that prestellar cores are formed, understanding their properties is a fundamental step towards understanding the process of star formation in galaxies.

Chapter 5 provides an estimate of the distorsions that should be expected in the Cosmic X-ray Background spectrum, of extra-galactic origin, as it propagates through different regions of the ISM.

To my father

Chapter 1

Introduction

"*There are two ways of spreading light: to be the candle or the mirror that reflects it.*"
Edith Wharton

Ever since the first extra-solar X-ray source, Scorpion X-1, was discovered in 1962 (Giacconi et al., 1962), we have known that the Milky Way is sprinkled with X-ray "candles", sources illuminating our Galaxy with light in the keV band. Numerous satellite missions have since allowed us to reveal the great variety, both in nature and radiative properties, of sources emitting light at these wavelengths.

Not all the X-ray radiation emitted by these sources, however, is observed by us directly: part of it is reflected towards us by the gas in the interstellar medium (ISM). Far from acting like a perfect mirror, the ISM - due to its non-uniform distribution and composition, as well as its interaction with the incoming X-ray radiation - heavily distorts the image that is reflected towards us.

The process of reconstructing the source emission from the reflected light can help us reveal a great deal about the gas structures responsible for reprocessing the radiation, as well as the radiative properties of the sources themselves. It can, in fact, often prove to be advantageous over the direct observation of either gas structures or X-ray sources.

In this thesis, I will demonstrate just how powerful the study of the observational signatures of the interaction of X-rays with matter can be, by applying it to several problems of extremely different scale and scope.

1.1 Processes of X-rays interaction with matter

I begin by reviewing the physical processes that describe the interaction of X-rays with matter, and the secondary radiative phenomena that arise from it. Both will determine the spectral characteristics of the X-ray emission reflected towards us by the intervening ISM.

1.1.1 Scattering

Scattering on free electrons

The interaction of low-energy radiation ($h\nu \ll mc^2$) with free stationary charges is described by the classical case of Thomson scattering. For the case of unpolarised incident light, the differential cross section of this interaction takes the following form:

$$h\nu_1 = h\nu_2 \tag{1.1}$$

$$\frac{\mathrm{d}\sigma_T}{\mathrm{d}\Omega} = \frac{1}{2} r_e^2 (1 + \cos^2\theta) \tag{1.2}$$

where σ_T is the Thomson cross section, Ω is the solid angle, r_e is the classical electron radius, θ is the angle at which the photon is scattered, and the subscripts 1 and 2 refer to the photon prior and following the interaction respectively. In the classical limit of low photon energies, the photon momentum ($= h\nu/c$) is negligible. Since no recoil takes place during this interaction, the incoming and outgoing energy of the photon remains constant.

As the energy of the photons increases, however, the momentum of the photon starts affecting the kinematics of the scattering process: the scattering is no longer elastic, and the charge will recoil following interaction with the high frequency radiation (Rybicki & Lightman, 1986). From momentum and energy conservation, it can be shown that the change in energy of the photon can be expressed in the following form:

$$h\nu_2 = \frac{h\nu_1}{1 + \frac{h\nu_1}{mc^2}(1 - \cos\theta)} \tag{1.3}$$

which reduces to $h\nu_1 = h\nu_2$ for $h\nu \ll mc^2$ as expected.

Quantum effects however do not only affect the kinematics of the process, but the cross section too. In a fully quantum electrodynamic framework (Heitler, 1954) the differential cross section takes the following form, known as the Klein-Nishina formula:

$$\frac{\mathrm{d}\sigma_{KN}}{\mathrm{d}\Omega} = \frac{1}{2} r_e^2 \left(\frac{\nu_2^2}{\nu_1^2}\right)\left(\frac{\nu_1}{\nu_2} + \frac{\nu_2}{\nu_1} - \sin^2\theta\right) \tag{1.4}$$

which again, for the $h\nu_1 = h\nu_2$ case reduces to the classic formula.

Because the energy of the outgoing photon is uniquely constrained by the scattering angle θ, it is possible to substitute Eq 1.3 in the above expression and integrate to obtain the total Klein-Nishina cross section, given by:

$$\sigma_{KN} = \sigma_T \frac{3}{4}\left[\frac{1+x}{x^3}\left(\frac{2x(1+x)}{1+2x} - \ln(1+2x)\right) + \frac{1}{2x}\ln(1+2x) - \frac{1+3x}{(1+2x)^2}\right] \tag{1.5}$$

where $x = h\nu/mc^2$. In an extreme relativistic regime ($x \gg 1$) this expression reduces to:

$$\sigma_{KN} = \frac{3}{8}\sigma_T x^{-1}\left(\ln 2x + \frac{1}{2}\right) \tag{1.6}$$

Relativistic corrections to the cross section, therefore, have the effect of reducing it from its classical (Thomson) value as the energy of the photon increases.

Scattering on neutral matter

In the previous section, the physical processes discussed described the interaction of X-ray photons with free charges. However, X-rays may also interact with electrons bound in atoms, with important consequences to the cross section.

One of the most immediate differences compared to the case of free electron scattering is that electrons bound in atoms occupy discrete energy levels. Depending on the initial (i) and final (f) state of the electron in the atom before and after interaction, the interaction process can be classified as either: Rayleigh or elastic scattering, involving a change in the direction of the incoming photon at constant frequency ($i = f$), Raman scattering, resulting in the excitation of the bound electron (f = excited state) and Compton scattering, resulting in the ionisation of the atom or molecule (f= continuum state).

Another difference, due to the Heisenberg uncertainly principle, is that the position and momentum of the bound electrons are not constrained, but are rather distributed over a probability density (Eisenberger & Platzman, 1970; Sunyaev & Churazov, 1996; Vainshtein et al., 1998). This implies that the energy of the scattered photon is not unambiguously constrained by the scattering angle, and therefore that the Klein-Nishina (KN) formulation for the change in energy undergone by the photon during the interaction, described in Eq. 1.3, is no longer sufficient.

Accounting for these two additional effects, the interaction of X-ray photons with light atoms is then described by the following expression (Vainshtein et al. (1998)):

$$\frac{\mathrm{d}\sigma}{\mathrm{d}\Omega \mathrm{d}h\nu} = r_e^2 \left(\frac{\nu_2}{\nu_1}\right) (\mathbf{e_1}\mathbf{e_2})^2 \sum_f |\langle f|e^{i\chi\mathbf{r}}|i\rangle|^2 \delta(\Delta E_{if} - \Delta h\nu), \tag{1.7}$$

where $\chi = (\mathbf{k_1} - \mathbf{k_2})/\hbar$, $\mathbf{k_1}$ and $\mathbf{k_2}$ are the initial and final electron momenta, ΔE_{if} denotes the energy change in the final and initial state of the atom or molecule, and $\mathbf{e}$ is the direction of polarisation. Notice that, for completely unpolarised incident light, the factor $(\mathbf{e}_1\mathbf{e}_2)^2$ reduces to the $\frac{1}{2}(1 + \cos^2\theta)$ term in the Klein-Nishina expression when averaged over all possible polarisation directions.

In the case of atoms and molecules heavier than atomic hydrogen, the most relevant differences with respect to free-electron scattering are found in the elastic scattering cross section. These can be described as follows:

- Bound electrons can coherently scatter photons, enhancing the scattering at small angles by a factor of Z^2 (where Z is the number of bound electrons). This implies that even heavy elements with a low relative abundance can significantly contribute to the elastic scattering of X-ray radiation, which dominates at small scattering angles. As shown in Table 1.1, in the Rayleigh scattering limit ($\theta = 0°$), metals - defined as elements heavier than He - can contribute up to 10% in this extreme case. This is, of course, an upper limit, as the actual contribution, when suitably averaged over different scattering angles, would be smaller compared to the values quoted in the table.

- The range of angles and energies at which the elastic scattering remains dominant also increases with additional electrons, due to the decreasing characteristic size of the electron distribution, D. The condition that the elastic scattering dominates is in fact determined by $\chi \mathbf{r} \lesssim 1$, which in the small angle approximation can be rewritten as $\theta 2\pi D/\lambda \lesssim 1$, where λ is the photon's wavelength (Sunyaev et al., 1999b).

- The range of scattering angles over which Rayleigh scattering dominates, however, also rapidly decreases with increasing energy, as shown in Figs. 1.1 and 1.2. The enhancement of the total scattering cross section due to coherence effects therefore mostly contributes to the scattering in the softer energy band.

While for atomic hydrogen, due to its simple electronic structure, all calculations of the matrix term in Eq. 1.7 can be performed analytically, for bound systems, with a higher number of electrons, approximations to the wave functions or numerical integration tools must be introduced.

One of the most commonly used methods in computing the interaction is the impulse approximation (IA), which is relevant in the case of a decrease in the photon energy due to scattering much larger than the binding energy (Eisenberger & Platzman, 1970; Sunyaev & Churazov, 1996). In this approximation, each electron is assumed to be in the field of the nucleus and in an average field due to the other electrons, and the interaction with the atom is assumed to take place through one electron only, leaving the wave functions of the electrons not interacting with the X-ray photon unaltered during the scattering process. This approximation has been used, for example, to describe the departure of the singly differential cross section from the KN prescription. This allows the implementation of the singly differential case by computing corrections to the KN formulation via an incoherent scattering factor $S(x)$ (Bergstrom et al. (1993)), such that:

$$\left(\frac{\mathrm{d}\sigma}{\mathrm{d}\Omega}\right)_{\mathrm{Compt}} = S(x)\left(\frac{\mathrm{d}\sigma}{\mathrm{d}\Omega}\right)_{\mathrm{KN}} \tag{1.8}$$

where $x(\theta)$ is the momentum transfer and θ is the scattering angle.

More recently, numerical methods implemented in the ATOM program were used to calculate the terms in this matrix Vainshtein et al. (1998).

Table 1.1: Elements by maximal contribution to Rayleigh scattering if all hydrogen is in atomic form (or molecular form, given in parentheses). n_H is the total number density of hydrogen atoms in HI or H2 form. Solar photospheric abundances from Asplund et al. (2009) are assumed.

Element	$Z^2 \times n_Z/n_H$
HI (H2)	1 (2)
He	0.340
O	0.031
Fe	0.021
C	0.010
Ne	0.008
Si	0.006
Mg	0.006
Total	1.42 (2.42)
Other elements (total)	$\lesssim 0.01$

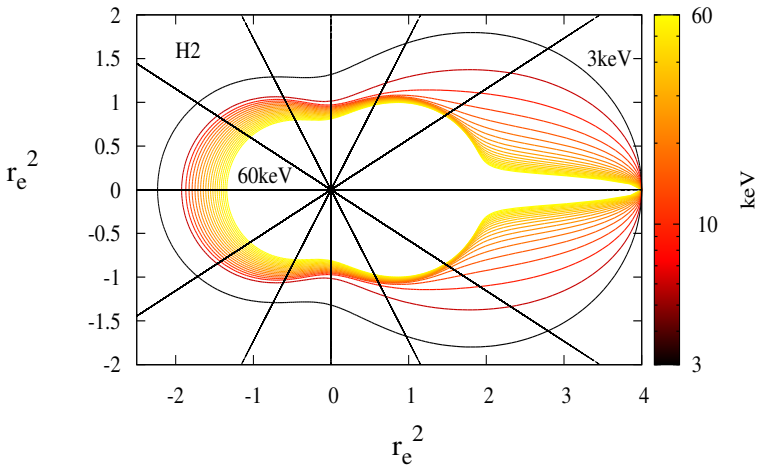

Figure 1.1: Cross section (Rayleigh + Compton) of H2 in polar coordinates, $\sigma(\theta)e^{i\theta}$, where σ is the amplitude of the cross section in units of r_e^2 for the scattering angle θ and r_e is the classical electron radius. The enhancement of Rayleigh scattering, which mainly contributes to the scattering at low scattering angles, due to coherence effects is clearly visible at low energies. While the cross section remains constant with energy at angles close to zero, the contribution of Rayleigh scattering is shown to quickly decrease with increasing energy. Compton scattering is also suppressed by relativistic effects.

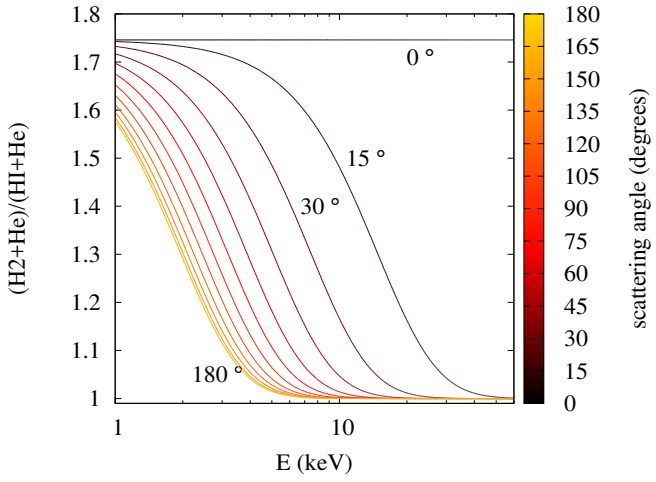

Figure 1.2: Ratio of the total (Rayleigh + Compton) differential cross section of H2 + He to HI + He (where each element is weighted by relative abundance) as a function of energy for different scattering angles. The total cross section approaches that of unbound electrons as the importance of coherence effects decreases with energy, because of the suppression of Rayleigh scattering.

1.1.2 Photoabsorption

X-rays further interact with matter through the process of photoionisation: photons are absorbed by atoms and molecules and consequentially ionise tightly bound electrons in their innermost shells, destabilising their electron configuration (see section 1.1.3).

A complete set of analytic fits to the photoionisation cross sections for all sub-shells of atoms and ions of elements with atomic number $Z \leq 30$ was estimated by Verner & Yakovlev (1995) using Hartree-Dirac-Slater (HDS) calculations. Using these fits, it is possible to estimate a total photoionisation cross section for the ISM, where the contribution of each element is weighed by its relative abundance compared to neutral hydrogen, as illustrated in Fig. 1.3. The cross section, in this case, is dominated by the HI contribution, and rapidly decreases with energy, roughly as E^{-3}. The contribution of other elements is close to negligible, with the exception of Fe, whose contribution to the photoabsorption, despite its very low abundance in comparison to neutral hydrogen ($n_Z/n_{HI} \sim 3 \times 10^{-5}$ in Lodders (2003)), is comparable to that of HI above the 7.1 keV ionisation threshold (see Fig. 1.3).

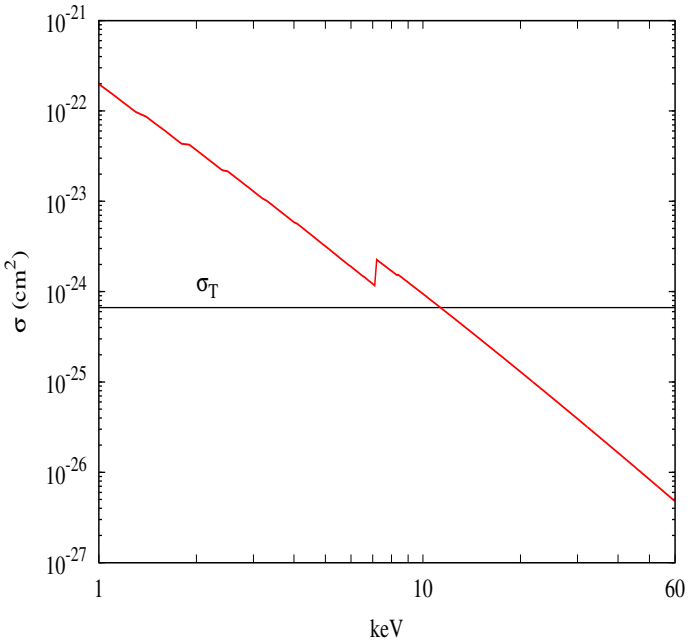

Figure 1.3: Photoionisation cross section for an ISM composition given by the Lodders (2003) protosolar abundance, compared to the Thomson scattering cross section (σ_T). The contribution of neutral iron above its ionisation threshold (7.1 keV) is clearly visible in the plot.

1.1.3 Fluorescence and Auger effect

The unstable electron configuration of the ionised atom following X-ray photoionisation prompts the filling of the vacancy by an electron from one of the higher energy levels,

which causes a release of energy. This energy can either be released through the emission of a photon in the X-ray range (fluorescence) or be transferred to another electron, which is then ejected from the atom (Auger effect).

Fluorescent lines are classified according to: i) the lower electron shell involved in the electron transition; ii) the difference in quantum number between the higher and lower electron shells involved in the transition (this is referred to with a Greek letter, such that α corresponds to a difference of 1, β to 2, etc); iii) the doublet energy level in the np orbital, due to spin-orbit interaction, originally occupied by the electron. A fluorescent photon resulting from the transition of an electron from $L_3(2p_{3/2})$ to K(1s), for example, is classified as a K-α_1 photon.

The intrinsic probability of fluorescent emission, otherwise known as the yield, varies depending on the electron configuration of the atom as well as on the type of transition of the electron. In particular, it rapidly increases with the number of electrons in the fluorescent atom. The yield of each line is estimated experimentally as $Y_K = I_K/n_K$, where I_K is the total number of K photons produced from a large sample of atoms, and n_K is the number of K-shell vacancies produced in the sample (Bambynek et al., 1972). The typical timescale of the entire fluorescence process is measured in billionths of a second, and can therefore be approximated as instantaneous in most astrophysical applications.

In the case of fluorescent emission following photoionisation, the strength of the lines in the spectrum is related both to the intrinsic yield of each line, and to the probability of photoabsorption by the fluorescent atoms. The high yield of the Fe K-α emission, together with the relatively large contribution of iron to the ISM photoionisation cross section, makes this line a particularly visible and well studied one in reflected X-ray spectra. The inelastic scattering of some of the fluorescent photons down to lower energies can, in the case of particularly strong fluorescent emission, be visible as a line's "shoulder", a characteristic increase in the continuum in the proximity of the fluorescent features. The ratio of the shoulder's equivalent width (EW) to that of the line is therefore only dependent on the column density of the surrounding material, and not on the spectral property of the source. It therefore represents a powerful tool in the study of gas structures reflecting X-ray emission from nearby X-ray sources.

Chapter 2

A truly diffuse component of the Galactic Ridge X-ray emission

2.1 Origin of the GRXE: a diffuse or discrete emission?

The unresolved or apparently diffuse X-ray sky is composed of two large-scale features. One is an isotropic (on subarcsec scales) emission, known as the cosmic X-ray background (CXB) (Giacconi et al., 1962), which results from the superposition of a large number of extragalactic sources such as active galactic nuclei (AGN) (eg. Giacconi et al., 2002). The other is a component confined mostly to the plane of our Galaxy, known as the Galactic Ridge X-ray emission (GRXE) (Worrall et al., 1982). Despite having been known for over thirty years, the origin of the latter emission has still not been conclusively resolved.

Because of the difficulty in resolving the GRXE into point sources, it was initially believed that its nature might be truly diffuse, and that a Galactic plasma, rather than discrete stellar sources, might be its origin. The spectrum of this emission in fact presents prominent lines at 6-7 keV, which could be explained by the emission of highly ionised elements in a thermal plasma of extremely high temperature, close to tens of millions of Kelvin (Koyama et al., 1986). It was soon realised, however, that a plasma with such high temperatures could not remain gravitationally confined to the Galactic plane, and would instead escape the Galaxy at supersonic speed. The resulting energy-loss rate due to this outflow would be $\sim 10^{43}$ erg/s. Since there is no energy source in the Galaxy available to replenish such a high energy loss, the thermal origin of the emission was soon excluded (Koyama et al., 1986; Sunyaev et al., 1993; Tanaka et al., 1999; Tanaka, 2002; Muno et al., 2004; Revnivtsev, 2003).

It was therefore suggested (Koyama et al., 1986) that the GRXE might be composed of a large number of faint X-ray sources, which due to their low flux cannot be as easily resolved as more luminous X-rays sources in our Galaxy. Although at the time it was not possible to see them, the hope was that with the increasing sensitivity of new X-ray satellites, a multitude of faint X-ray sources could one day be fully resolved, and its discrete

nature unveiled.

Today, strong evidence, both direct and indirect, in support of a discrete origin to the emission has led the community to reach a general consensus on the point source origin of the emission. The mystery of the origin of the GRXE thus seemed to have been conclusively solved. In Molaro et al. (2014), however, we showed that this may not be the whole story, and that the GRXE might have a truly diffuse component after all. In particular, we suggested that the reprocessing by the ISM of X-ray photons emitted by luminous X-ray sources could contribute an important fraction of the GRXE on the plane of the Galaxy, which would therefore constitute a truly diffuse component of the GRXE.

2.1.1 Evidence for a discrete component of the GRXE

One of the strongest pieces of evidence in support of a discrete nature of the emission comes from the direct resolution of the low-luminosity sources which produce it. Ever since the GRXE was first observed, there have been a number of attempts to directly resolve discrete low-luminosity stellar sources within it using the Chandra and X-ray Multi-Mirror Mission (XMM-Newton) observatories (Ebisawa et al., 2001; Muno et al., 2004; Ebisawa et al., 2005; Revnivtsev et al., 2006, 2009; Morihana et al., 2013). In 2009, Revnivtsev et al. (2009) finally succeeded in resolving, at a flux sensitivity of $F_{2-8\mathrm{keV}} \sim 10^{-16}$ erg s^{-1} cm^{-2}, $\sim 80-90\%$ of the emission in a narrow band around 6.7 keV. The observation was carried out in a small region of the sky (16×16 arcmin) centred just below the Galactic plane, at $l = 0.08°, b = -1.42°$. The resolution of the GRXE into point sources *in* the Galactic plane itself, on the other hand, has proven more difficult, due to the difficulty in separating out extragalactic sources and insufficient sensitivity and angular resolution to resolve the weak but densely populated Galactic sources.

Along with the direct resolution of the sources, other indirect probes have strengthened the case for a discrete origin of the GRXE. These include the similarity of the large-scale morphology of the emission with that of the Galactic near-infrared (NIR) brightness (Revnivtsev et al., 2006). This should be expected in the case where weak stellar X-ray sources such as cataclysmic variables (CVs) and coronally active stars and binaries (ASBs) should contribute a significant component of the GRXE. These sources should in fact trace the old stellar population, which represents the main emitter of NIR radiation in the Galaxy. Revnivtsev et al. (2006) used data from the Rossi X-Ray Timing Explorer - Proportional Counter Array (RXTE/PCA) to show that the 3-20keV component of the emission traces the stellar mass distribution and is well fitted by models of the Galactic stellar bulge and disk from Dwek et al. (1995), Bahcall & Soneira (1980), Kent et al. (1991), Freudenreich (1996), and Dehnen & Binney (1998). Using results from Sazonov et al. (2006), Revnivtsev et al. (2006) also found that the GRXE broad-band spectrum is very similar to the superposition of the spectra of low-luminosity X-ray sources in the solar neighbourhood. Further studies on the similarity of the GRXE spectrum with the one produced by the superposition of the spectra of the low X-ray luminosity sources expected to contribute to the emission have also shown good agreement (Ebisawa et al., 2001, 2005; Revnivtsev et al., 2006; Morihana et al., 2013; Warwick, 2014). These results

agree with the studies of the hard (17-60keV) component using the IBIS telescope on-board of INTErnational Gamma-Ray Astrophysics Laboratory (INTEGRAL) by Krivonos et al. (2007a). We refer to the contribution of low luminosity (in X-rays) stellar sources to the GRXE as *stellar GRXE*.

2.1.2 An indirect contribution from Galactic X-ray binaries

The strong evidence in support of a discrete origin of the GRXE seemed to indicate that the nature of the GRXE had finally been solved.

Sunyaev et al. (1993), however, first suggested that part of the GRXE may be composed of radiation originally emitted by luminous X-ray sources and later reprocessed by the ISM. Our Galaxy is in fact sprinkled with very bright X-ray sources, which could not be directly contributing towards the GRXE due to their high flux, but which do illuminate the gas in the ISM with abundant X-ray radiation. Free electrons, atomic and molecular hydrogen, helium, and heavier elements present in the interstellar medium then scatter these illuminating photons, and give rise to a Galactic scale emission which should constitute a truly diffuse component of the GRXE.

This component of the GRXE, which we refer to as *scattered GRXE*, should be characterised by the presence of a K-α line resulting from the photoionisation of neutral iron in the ISM. Evidence in support of the presence of this line in the GRXE was indeed found by Koyama et al. (1996) who, using observations from ASCA, first resolved what was initially thought to be a 6.7 keV iron K-α line from the Galactic centre into a 7 keV and a 6.7 keV line from highly ionised H-like and He-like iron, respectively, and a 6.4 keV line from neutral iron. This was later confirmed using Suzaku observations by Koyama et al. (2007) and Ebisawa et al. (2008).

In this work, we estimate the contribution of the scattered GRXE by considering the brightest class of X-ray sources in the Galaxy, X-ray binaries (XBs), which dominate the 2-10 keV emission of the Milky Way, and compare it to the direct contribution of discrete faint sources. In our calculations, we consider two XB populations: one based on observations, and one simulated from theoretical models. We also consider two ISM models, one assuming smooth disk components, and one accounting for the clumping of gas in the form of molecular clouds.

We also take into account the scattering of the X-ray radiation on multi-electron species such as H2 and He, and heavy elements. As discussed in Chapter 1, coherent scattering by multi-electron atoms and molecules significantly increases the scattering cross section at small angles, with important consequences for X-rays emitted by sources which lie on the plane of the Galaxy, which would only need to be scattered by a small angle in order to reach an observer at the Sun's position. Molecular clouds, which in addition to being located on the plane of the Galaxy have a molecular composition and high density, should therefore greatly contribute to the scattered GRXE component, and should be detected as regions of high X-ray intensity in the GRXE.

2.2 Modelling the scattered GRXE

In this section, I discuss the models used to simulate the scattered GRXE, including the XB populations (Section 2.2.1) and ISM distributions (Section 2.2.2) assumed. In Section 2.2.3, I discuss the possible contribution of Galactic sources other than XBs to the scattered GRXE, in particular that of the faint X-ray sources which directly contribute to the GRXE, which will be accounted for in our calculations for completeness. Finally, in Section 2.2.4, I discuss the details of the algorithm used to compute the contribution of the GRXE at different positions on the sky.

2.2.1 XBs in the Milky Way

XBs are binary systems in which a compact object, either a black hole (BH) or a neutron star (NS), accretes matter from a companion star, either through Roche-lobe overflow or stellar winds. The nature of the companion can vary widely, going from a brown dwarf (BW) Bildsten & Chakrabarty (2001), to a main sequence (MS) star or a white dwarf (WD) Tutukov et al. (1987). Finely tuned conditions are required for these systems to form: the two objects must be separated enough not to merge in a common envelope but close enough for a relatively stable mass transfer to take place after the supernova explosion has taken place (Grimm, 2003). This implies that a very small fraction of the numerous binary systems in which most stars are found end up forming an X-ray binary (Illarionov & Sunyaev, 1975). Despite the low number of sources expected, which is of order a few thousand systems in the Galaxy in total (eg Dalton & Sarazin (1995); Iben et al. (1995)), the extreme conditions under which matter is accreted in these systems are such that X-ray emission from XBs actually dominates the 2-10 keV luminosity of galaxies like the Milky Way. The amount of scattered X-ray radiation observed on these scales will therefore be closely related to the total luminosity of the XB population, $L_{\rm XBs}$.

Due to their diverse nature, a variety of different classifications exist for these sources (eg. Reig, 2011), either based on the nature of the donor star or on the radiative properties of the system. For the purposes of this thesis, the most useful classification is the one based on the mass of the donor star, which determines both the total luminosity of the sources and their distribution in the Galaxy given global galactic properties such as the stellar mass (M_*) of a galaxy and its star formation rate (SFR), as discussed below.

Besides the total luminosity of the XB population, in fact, another important factor determining how "efficiently" the radiation emitted by these sources is scattered towards the observer is the distribution of the sources in the Galaxy compared to that of the gas. This is important for two reasons. First, the further away the source from the gas, the lower the flux F reaching the gas, since:

$$F = \frac{L}{4\pi D^2} \tag{2.1}$$

where L is the source luminosity and D is the distance between the source and the gas.

Second, that the relative position of the source with respect to the gas and the observer determines the average angle at which radiation from that source will have to be scattered in order to be detected. Because most of the gas, as discussed in Section 2.2.2, is concentrated on the disk of the Galaxy where the observer (the Sun) is located, the angle at which radiation has to be scattered by the gas in order to reach the observer is on average lower for sources located on the plane of the Galaxy than if the emitting sources are located above the plane. As discussed in Section 1.1.1, scattering at low angles will be enhanced in the case of interaction with neutral matter due to coherence effect.

The evolutionary timescale of the binary system is strongly defined by the life-time of the donor star, since the time spent on the main sequence by the star is ($\propto M^2$). XBs with a donor star of mass $M > 5M_{\odot}$, known as high-mass XBs (HMXBs) are relatively short lived, and have a typical lifetime of of 10-100 Myr. XBs with a donor star of low mass ($M < 1M_{\odot}$), known as low-mass XBs (LMXBs) are on the other hand long lived, with a typical lifetime of 1-10 Gyr. Binary systems with donor masses in the intermediate range, $1 - 5M_{\odot}$, called intermediate-mass XBs (IMXBs) are extremely rare in the Milky Way.

Grimm et al. (2002) first pointed out that, due to the different evolutionary timescale of the two populations, the properties of LMXBs and HMXBs populations should be related to different properties of the host galaxy. The long evolutionary timescales of low-mass donor stars, in fact, imply that LMXBs are expected to follow the older stellar population, while the short lifetime of the high-mass donors in HMXBs means that these should trace the younger stellar population of the Galaxy, which in turn traces the galactic gas. We should therefore also expect a relationship between the spatial distribution (van Paradijs & White, 1995; White & van Paradijs, 1996; Koyama et al., 1990) and total luminosity (Grimm et al., 2002) of XBs with M_* in the case of LMXBs, and with the *SFR* in the case of HMXBs.

Total luminosity of XBs in the Milky Way

Grimm et al. (2002) in fact first suggested that the total luminosity of these sources should be related to the global galactic properties M_* and *SFR* as:

$$L_{\rm LMXBs} = \alpha \times M_{\star} \tag{2.2}$$

$$L_{\rm HMXBs} = \beta \times SFR \tag{2.3}$$

They calculated the $2 - 10$ keV luminosity of Galactic X-ray binary sources averaged over the period 1996-2000, using Rossi X-ray Timing Explorer (RXTE) All-Sky Monitor (ASM) data. The total luminosity of the sources in this sample (using updated distance estimates for each source as compiled by Molaro et al. (2014)) is 2.6 $\times 10^{39}$ erg/s and 5.5×10^{37} erg/s for LMXBs and HMXBs respectively (referred to as "observed" luminosities in Table 2.1). Because the sample is severely affected by flux limitations, and therefore by incompleteness issues, Grimm et al. (2002) corrected the observed luminosity using models for the Galaxy's gas and stellar mass distribution, which HMXBs and LMXBs respectively are expected to follow, and estimated the expected total luminosity of the sources in the

Galaxy to be $2-3\times10^{39}$ erg/s in the case of LMXBs and $2-3\times10^{38}$ erg/s in the case of HMXBs (referred to as "estimated" luminosities in Table 2.1). This estimate, besides the uncertainties arising from corrections to the flux limitation of the sample, is also severely affected by large uncertainties in determining the location of the individual sources in the Galaxy, or alternatively their distance along the line of sight, from their optical counterpart, due to the high-column density for observations in our Galaxy, which result in the sever absorption of the optical emission of these sources.

Assuming a *SFR* in the Milky Way of 4 $M_\odot$/yr and a M^* of $5\times10^{10}M_\odot$ they were then able to estimate scaling parameters α and β as:

$$\begin{aligned}\alpha &\sim 5\times10^{28}\mathrm{erg}/(\mathrm{s}M_\odot)\\ \beta &\sim 5\times10^{37}\mathrm{erg}/(\mathrm{s}M_\odot\mathrm{yr}^{-1})\end{aligned} \tag{2.4}$$

The study of these parameters α and β has since been widely investigated in other galaxies in Grimm et al. (2003); Ranalli et al. (2003); Gilfanov (2004); Colbert et al. (2004); Persic & Rephaeli (2007); Lehmer et al. (2010); Mineo et al. (2012, 2014) and up to redshift $z\sim1.3$ using 66 galaxies in Mineo et al. (2014). The study of these relations in external populations avoids issues of incompleteness and distance uncertainties which are important in the study of local XBs. These studies find values:

$$\begin{aligned}\alpha &\sim 8\times10^{28}\mathrm{erg}/(\mathrm{s}M_\odot)\\ \beta &\sim 2.2-2.6\times10^{39}\mathrm{erg}/(\mathrm{s}M_\odot\mathrm{yr}^{-1})\end{aligned} \tag{2.5}$$

Assuming the values in Eq. 2.5, we can then estimate what the expected total luminosity for the XB population in the Milky Way would be in the case where our galaxy's XB population scales with $M_\star$ and *SFR* in a similar way to the one observed in other galaxies. Using the parameter values in Eq. 2.5, and assuming updated estimates for the stellar mass and *SFR* of the Milky Way of $M_\star=6\times10^{10}M_\odot$ (McMillan, 2011) and $SFR\sim1M_\odot$/yr (Robitaille & Whitney, 2010), we obtain a luminosity of 5×10^{39}erg/s for LMXBs and $2-3\times10^{39}$erg/s for HMXBs (referred to as "expected" luminosities in Table 2.1).
Comparing these with the estimated luminosities by Grimm et al. (2002) (see Table 2.1), we can see that even accounting for catalogue incompleteness, the Milky Way appears to be under luminous by a factor of 2 in its LMXB luminosity, and by a factor of 10 in its HMXB luminosity.

Notice that the difference in the estimated and expected luminosities for HMXBs is lower than the difference in the parameters β given in Eq. 2.4 and Eq. 2.5. This discrepancy is due to the fact that the *SFR* assumed in Grimm et al. (2002) of $4M_\odot\mathrm{yr}^{-1}$ (McKee & Williams, 1997) has been shown to be a clear overestimate of the rate of star formation in the Milky Way by more recent studies (see Robitaille & Whitney (2010) for a discussion).

Is the Milky Way subluminous in X-rays compared to other galaxies?

The Milky Way therefore appears to be subluminous in LMXBs by a factor of ~2, consistent with the original results of Gilfanov (2004), and by a factor of ~10 in the luminosity of HMXBs compared with other galaxies.

$L_{2-10keV}$	LMXBs (erg/s)	HMXBs (erg/s)
Observed[(1)]	2.6 $\times 10^{39}$	5.5×10^{37}
Estimated[(2)]	2-3 $\times 10^{39}$	2-3 $\times 10^{38}$
Expected[(3)]	4.7 $\times 10^{39}$	1.7×10^{39}

Table 2.1: Total luminosities of the LMXB and HMXB Galactic population in the 2-10 keV range. [(1)] Observed ASM source sample studied in Grimm et al. (2002) with updated distances, as compiled in Molaro et al. (2014). [(2)] Grimm et al. (2002) estimates, which consider the ASM source sample and account for incompleteness issues in the latter. [(3)] Luminosities expected for the Milky Way assuming α and β parameters as observed in other galaxies, and $M_\star$ and SFR values of $M_\star = 6 \times 10^{10} M_\odot$ (McMillan, 2011) and $SFR \sim 1 M_\odot$/yr (Robitaille & Whitney, 2010)

One of the possible explanations for the large discrepancy in the HMXB luminosity is the difficulty in estimating the *SFR* in the Milky Way, whose value therefore includes large uncertainties. Furthermore, the values for the *SFR* assumed do not take into account that there is a delay of $10^6 - 10^7$ years between the time of starburst and appearance of HMXBs (Gilfanov, 2004; Shtykovskiy & Gilfanov, 2007), corresponding to the evolutionary timescale of the donor star. This implies that the relevant SFR is not the present one, but that of a million years ago.

Another possible explanation, advanced by Gilfanov (2004) and Mineo et al. (2014), is that the apparent discrepancy in the total luminosity is due to issues of low-number statistics in the Milky Way. Due to the relatively low start formation activity in our Galaxy compared to that of other galaxies, few HMXB sources contribute to the total luminosity in the Milky Way at any given time. Because the total luminosity is dominated by a small number extremely bright objects, and due to the strong temporal variability of HM sources, we expect different such objects will contribute at different times. Therefore, it is possible that due to strong temporal variations in L_{HMXB}, we happen to be undergoing an exceptionally low-luminosity phase, but that the time-averaged total luminosity could be more similar, when scaled by *SFR*, to that observed in other galaxies. This is supported by the scatter of more than an order of magnitude in the luminosity-*SFR* relations (Mineo et al., 2014) and by the broad probability distributions for the X-ray luminosity at low star formation rates (Gilfanov et al., 2004).

If we assume, optimistically for our purpose, that the discrepancy is due to the fact that we happen to live in a time where the observed X-ray luminosity of our Galaxy is below average, we can conclude that if averaged over a time-scale of $10^3 - 10^4$ years our Galaxy would turn out to have an average luminosity consistent with that that would be expected based on observations of XBs in other galaxies.

Because of time-delays, the contribution of scattered X-rays to the GRXE is sensitive

not only to the present luminosity of XBs, but to the average X-ray activity of the Galaxy in the past 1000-10000 years. Studies of the scattered component of the GRXE therefore allow us to probe the time-averaged activity of the XB population.

In our calculations, we consider two models of the Galactic XB population, discussed in the next two sections. First, one based on a catalogue of observed XB sources which, due to the incompleteness issue discussed earlier, allows us to place a lower bound on the contribution of the scattered GRXE. Second, one based on a catalogue of Monte-Carlo-simulated sources which reproduces the total XB luminosity expected from observations of other galaxies. This case, in particular, allows us to test whether the scattered GRXE component obtained for this case is consistent with observations of the emission, and therefore whether on average, the Milky Way XB population could be more similar to those observed in other galaxies.

Observed XB population

We use time-averaged X-ray flux measurements from different surveys to compile a catalogue of X-ray binary sources with known flux and position in different energy bands (2-10keV and 17-60keV). References for distance estimates for each source are taken from the SIMBAD database. The full catalogue of data for the observed sources can be accessed from `http://www.mpa-garching.mpg.de/~molaro`.

For the energy range $17-60$keV we combine different INTEGRAL surveys (Krivonos et al., 2007a, 2012; Lutovinov et al., 2013) from which we select 86 LMXB and 70 HMXB Galactic sources for a total 17-60keV luminosity of 1.97×10^{38}erg/s and 6.2×10^{37}erg/s, respectively, for which distance and best-fit spectral parameters data are available. We also consider the contribution in this range of four very luminous extragalactic HMXB sources (SMC X-1, LMC X-1, LMC X-4, IGR J05007-7047), which is, however, close to negligible.

For the lower energy range (2-10keV) we use the list of sources given in Grimm et al. (2002)[1] for which distance and flux measurements from RXTE/ASM, which provides all-sky flux measurements averaged over $\sim$ 5 yr, are available. We also use the relation $L_{2-10\mathrm{keV}}\sim0.5L_{17-60\mathrm{keV}}$ valid for NS binary sources (Filippova et al., 2005) to infer the 2-10keV luminosity from the harder X-ray range catalogue for 20 HMXB sources for which low-energy data are not available. In total, the number of sources considered in this energy range is 61 for the HMXBs, for a total 2-10keV luminosity of 5.5×10^{37} erg/s, and 81 for the LMXBs, with a total luminosity of 2.56×10^{39} erg/s. The energy output of these sources in the 3-20 keV range is modelled using the following model spectrum:

$$F(E)\propto E^{-\Gamma}\mathrm{e}^{-\frac{E}{E_0}}\ \ \mathrm{s}^{-1}\mathrm{keV}^{-1}, \tag{2.6}$$

with parameters $\Gamma=1$, $E_0=20\,$keV for HMXBs (Lutovinov et al., 2005) and $\Gamma=1$, $E_0=4.6\,$keV for LMXBs, which is a fit to the observed spectrum of GX 340+0 (Gilfanov et al., 2003). In the 17-60 keV range, on the other hand, we use the best-fit photon index

[1]See `http://edoc.ub.uni-muenchen.de/1279/1/Grimm_Hans-Jakob.pdf` for the full list of sources and associated data.

from Integral surveys (Krivonos et al., 2007b) and in some cases from the literature on individual sources when the former is not available. In general, we expect variations in the photon spectrum in the 2-10 keV range from source to source and also with time. Given the uncertainties in the time-averaged spectral properties of Galactic X-ray binaries, our description of the average spectrum should be adequate. To turn the problem around, if the diffuse component of GRXE can be separated from point sources using high angular resolution observations, then the scattered GRXE measurement will directly give us the average spectrum of X-ray sources in the Galaxy, after correcting for the effect of energy dependence of Rayleigh scattering, which makes the scattered spectrum softer than the incident spectrum and the effect of X-ray absorption. The distribution of the catalogue sources used in the calculations is shown in Fig. 2.1 in Galactic angular coordinates and in Fig. 2.2 as a projection on the Galactic plane.

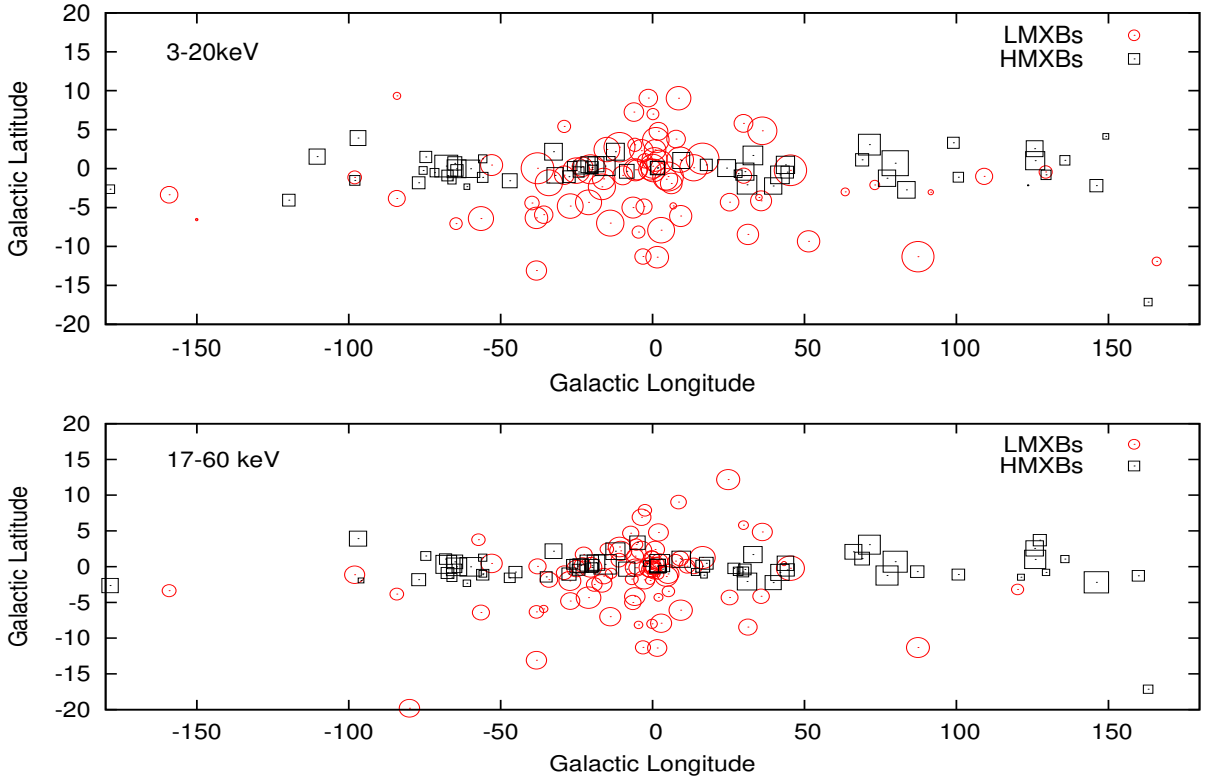

Figure 2.1: Distribution on the sky of observed LMXBs and HMXBs sources used in the calculations for energy ranges 3-20keV and 17-60keV with the symbol size proportional to their luminosity in the indicated energy range. A concentration of HMXBs can be seen along the lines of sight tangential to the spiral arms.

Simulated XB population

We simulate the case of a Galactic XB population whose total luminosity is that expected from observations of other galaxies (see Table 2.1) by populating the Galaxy with a Monte-

Carlo-simulated population of HMXBs and LMXBs. The probability density function (pdf) for the distribution of LMXBs in the Galaxy is taken to be proportional to the mass density of stars, whereas the pdf of HMXBs is taken to be proportional the mass density of the ISM; both the stars and ISM density distributions are modelled using the mass models in Dehnen & Binney (1998) and Binney & Tremaine (2008) (Eq. 2.7) with stellar disk parameters $z_{\rm d} = 325$ pc, $R_{\rm d} = 2.5$ kpc and $R_{\rm m} = 0$. HMXBs are therefore expected to be concentrated in the plane of the Galaxy, a fact that becomes important when we include the Rayleigh scattering at small angles on multi-electron atoms and molecules. We populate the Galaxy with 300 LMXBs and 100 HMXBs using Monte Carlo sampling from these distributions, which is consistent with observations taking into account the incompleteness of catalogue at the low-flux end (Ritter & Kolb, 2003; Liu et al., 2007, 2006). The sources are assigned luminosities sampled randomly from the luminosity functions of Gilfanov (2004) for LMXBs and Grimm et al. (2003) for HMXBs. The total $2-10$keV luminosity of the Galaxy in our calculation is $\sim 4.7 \times 10^{39}$ ergs/s for simulated LMXBs and $\sim 1.7 \times 10^{39}$ ergs /s for simulated HMXBs, which is consistent with the expectations from observations of other galaxies (Grimm et al., 2002, 2003; Gilfanov, 2004; Lehmer et al., 2010; Mineo et al., 2012, 2014). The spectral properties assumed for the simulated sources are modelled using the same model spectrum assumed for the observed XB catalogue (see previous section).

2.2.2 ISM model

Gas phases

The gas in the interstellar medium in the disk of the Galaxy has a multiphase character (McKee & Ostriker, 1977) loosely classified into atomic (neutral or ionised) gas and molecular gas, with the atomic gas further classified into cold neutral medium (CNM), warm neutral medium (WNM), warm ionised medium (WIM) and hot ionised medium (HIM) (see Kalberla & Kerp, 2009, for a recent review), while a significant part of the molecular gas is concentrated in giant molecular clouds (GMCs). The total ISM mass in both atomic and molecular form within a Galactocentric radius $R \lesssim 20$ kpc of the Galaxy is approximately 9.5×10^9 $\rm M_\odot$ (Kalberla & Kerp, 2009), with hydrogen (HI and H2) accounting for 71% of this mass. The ratio of average atomic to molecular gas is 4.9 within $R \lesssim 20$ kpc (Draine, 2011), giving a total HI mass of 5.6×10^9 $\rm M_\odot$ and a total H2 mass of 1.15×10^9 $M_\odot$ within this radius.

Most of the mass in the neutral atomic gas is confined to the disk of the Galaxy and is clearly traced by HI 21 cm emission. The maps of the HI 21 cm emission in the Galaxy (Kalberla et al., 2005; McClure-Griffiths et al., 2009) can only provide the total column density in parts of the sky, for example toward the Galactic centre, where the velocity information cannot be used to infer the three-dimensional gas distribution. The CNM, which contains most of the HI, is clumped into clouds that have a volume filling factor of $\sim 10-20\%$ in the plane of the Galaxy in the solar neighbourhood (Kalberla & Kerp, 2009). Any given line of sight should therefore intersect many clouds, making the column density much smoother. A smooth disk model therefore suffices for our calculation and we

use the models of Dehnen & Binney (1998) and Binney & Tremaine (2008) for the HI gas distribution.

The situation is slightly different for GMCs. These molecular structures, mainly concentrated near the Galactic centre region and in the spiral arms, have sizes of $\sim 10 - 100$ pc and average densities on the order of $10^2 - 10^3$ cm^{-3} with mean separation between the clouds 10 times the mean size (Blitz, 1993; McKee & Ostriker, 2007), giving a volume-filling factor in the plane of the Galaxy of $\sim 0.1\%$. They are therefore compact enough to significantly influence the morphology of the X-ray signal. The full-sky maps of the molecular gas distribution using CO lines (Dame et al., 2001) do not resolve and provide distances to individual clouds (Dame et al., 2001), although high-resolution studies of many important GMCs are available. Recently, high-resolution data with kinematic distances have been made available from the Boston University-Five College Radio Astronomy Observatory Galactic Ring Survey (GRS) (Jackson et al., 2006; Rathborne et al., 2009; Roman-Duval et al., 2009, 2010), which covers the very important molecular ring structure in the inner Milky Way. This survey, which span the longitude range $18^\circ \leq \ell \leq 55.7^\circ$ and latitude range $-1^\circ \leq b \leq 1^\circ$, only covers about 10% of the Galactic plane.

Because of the incompleteness of the GRS, we use a smooth disk model for the mass distribution of HI and H2 for full Galactic plane calculations, and use H2 data from the GRS (Jackson et al., 2006; Roman-Duval et al., 2009, 2010) for calculations limited to the longitude range covered by the survey. The latter case is used to study the effect of clumpiness and small volume-filling factor of the molecular clouds on the observed X-ray intensity morphology (see Section 2.3.2). Although limited to the $18^\circ \leq \ell \leq 55.7^\circ$ range, these results are easily extendable to and are valid for the full sky, and in particular clearly show the spatial morphology and features in the GRXE that should be expected from GMCs.

Atomic Hydrogen

The average density distribution of the interstellar HI gas in the Galactic disk can be described by an exponential disk (Dehnen & Binney, 1998; Binney & Tremaine, 2008). The ISM mass density distribution at a Galactocentric distance R and Galactic plane height z used in this model is given by

$$\rho_{\rm HI}(R,z) \propto \frac{1}{2z_{\rm d}} \exp\left(-\frac{R_m}{R} - \frac{R}{R_{\rm d}} - \frac{|z|}{z_{\rm d}}\right), \tag{2.7}$$

with parameters $R_m = 4$kpc, $R_d = 6.4$ kpc and $z_d = 80$ pc.

Notice that the scale height of the gaseous disk, $z_d = 80$ pc, is considerably lower than that of the stellar disk, which is of 130 pc (Dehnen & Binney, 1998; Binney & Tremaine, 2008). Because the morphology of the scattered X-rays will closely follow the distribution of gas in the Galaxy, we can therefore expect the scale height of the scattered and stellar GRXE components to be characteristically different.

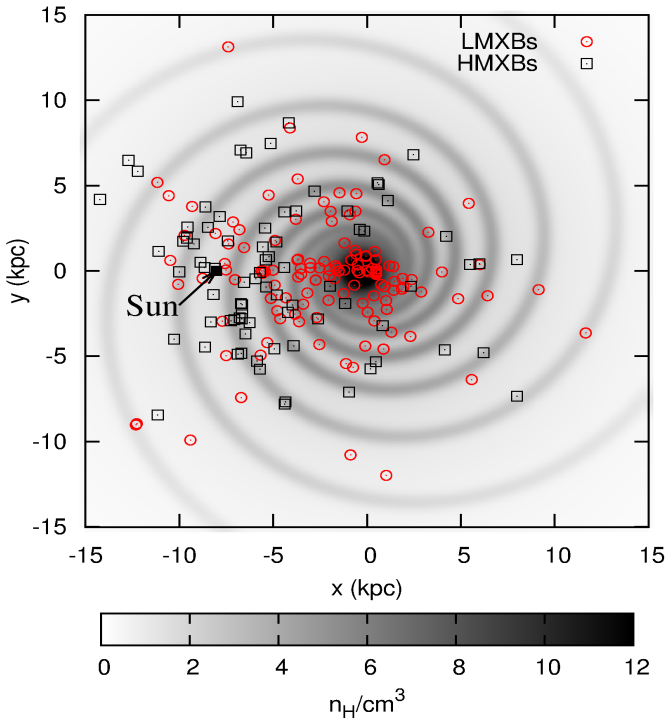

Figure 2.2: Projected distribution on the Galactic plane of persistent X-ray sources observed during the past 40 years used in our calculations, shown against the spiral structure of the Galaxy.

Molecular Hydrogen

The lack of HI gas in the central region of the plane, due to the central depression of radius 4 kpc in the HI disk, is compensated for by the concentration in this region of most of the H2 component, which gives a significant fraction of the scattering at low longitude values. The average H2 distribution in the Galaxy is given by Misiriotis et al. (2006) as

$$\rho_{\rm H2}(R,z) \propto \exp(-R/R_{\rm H2} - |z|/z_d) \tag{2.8}$$

with parameters $R_{\rm H2} = 2.57$ kpc and $z_d = 80$ pc as in Eq. 2.7. The GRS provides data for the spatial distribution, size and average density of 750 molecular clouds in the Galactic plane in the latitude range $-1^\circ \leq b \leq 1^\circ$ and the longitude range $18^\circ \leq \ell \leq 55.7^\circ$. This survey covers a part of one of the most significant concentrations of molecular gas in the Galaxy that is roughly distributed in a ring-like structure about 4 kpc from the Galactic centre (Stecker et al., 1975; Cohen & Thaddeus, 1977), although it may just be a spiral arm misinterpreted as a molecular ring (Dobbs & Burkert, 2012). We assume that the density of each individual cloud is constant throughout the object. The total H2 mass of the clouds in the GRS is 3.5×10^7 $M_\odot$.

Spiral structure

We also account for the concentration of matter in the Galactic disk into spiral arms. This is particularly important because HMXBs are also concentrated in the Galactic spiral arms: the combined effect of concentration of HMXBs as well as atomic and molecular clouds in these structures means that we expect an enhancement of scattered X-ray intensity in the directions tangential to the spiral arms. We describe the spiral structure of the Galaxy following the prescription given in Vallee (1995), where the location of the density wave maxima of the nth spiral arm is given by

$$m\left[\theta - \theta_0 - \ln(R/R_0)\tan(p)^{-1}\right] = (n-1)2\pi, \tag{2.9}$$

where $m = 4$ is the total number of spiral arms, $p = 12^\circ$ (inward) is the pitch angle and $R_0 = 2.5$ kpc. We have verified that the lines of sight tangential to the spiral arms in the model are consistent with the location of the tangential directions based on different observations, as summarised in Vallée (2008). We model the density around the spiral maxima as a Gaussian probability distribution with respect to the projected distance from the spiral arms' maxima on the Galactic plane d:

$$\rho_{Spiral} \propto \sum_{n=1}^{m} \exp(-(d_n/w)^2), \tag{2.10}$$

where the typical width w of the spiral arm is assumed to be 500 pc for the gas component. The density of the wave is assumed to be three times higher than the inter-arm density (Levine et al., 2006). The overall density distribution including the spiral structure is therefore given by

$$\rho_{\rm H}(R, z, \theta) \propto \left[1 + 3 \times \rho_{Spiral}(R, \theta)\right] \rho_{\rm H}(R, z) \tag{2.11}$$

for both $\rho_{\rm H} = \rho_{\rm HI}$ and $\rho_{\rm H} = \rho_{\rm H2}$. The distribution of gas in the Galaxy in our model is shown in Fig. 2.2. We assume constant abundances for heavier elements throughout the Galaxy with abundances taken to be same as the present-day solar photosphere from Asplund et al. (2009).

2.2.3 Contribution from sources other than XBs

Indirect contribution of low-luminosity X-ray sources

The X-ray emission from the low-luminosity sources which form the stellar GRXE will also be scattered by the ISM, adding to the diffuse scattered X-rays from X-ray binary sources. This effect can be accounted for by considering the scattering by the ISM of the observed GRXE, assumed to be of stellar origin. We use the models for the three-dimensional luminosity of the bulge and disk components of the GRXE based on infrared distribution of the Galaxy given in Revnivtsev et al. (2006) for the 3-20 keV range and apply it to the 17-60keV range by normalising the distribution to the GRXE luminosity in this range as

measured by Krivonos et al. (2007a). For the harder range we also assume the same ratio between the disk and bulge luminosity of ~ 2.5 measured in the 3-20 keV range. This ratio is consistent with the disk-to-bulge stellar mass ratio and therefore implies a uniform GRXE emissivity per unit stellar mass throughout the Galaxy. The bulge component is described by

$$\rho_{\mathrm{GRXE},bulge} \propto r^{-1.8}\exp[-r^3], \tag{2.12}$$

where

$$r = \left[(y/y_0)^2 + (z/z_0)^2 + (z/z_0)^2\right]^{1/2}$$

with $x_0 = 3.4 \pm 0.6$ kpc, $y_0 = 1.2 \pm 0.3$ kpc, $z_0 = 1.12 \pm 0.04$ kpc with the $x-y$ axes on the Galactic plane rotated by an angle $\alpha = 29 \pm 6^\circ$. The disk component, on the other hand, is described as

$$\rho_{\mathrm{GRXE},disk} \propto \exp\left[-(R/R_m)^3 - R/R_{disk} - z/z_{disk}\right], \tag{2.13}$$

with parameters $R_{disk} = 2$ kpc, $z_{disk} = 0.13$ kpc and fixed $R_m = 3$ kpc. The total bulge+disk luminosities considered are $\sim 1.39 \times 10^{38}$ erg/s and $\sim 4.2 \times 10^{37}$ erg/s in the 3-20 and 17-60 keV bands, respectively.

Contribution of Sgr A*

At present, XBs contribute the bulk of the Milky Way emission in the 2-10 keV range. An important feature of the scattered component, however, is that since the scattered X-rays travel a longer path to reach us from the original source, the X-rays seen by us today probe the past X-ray activity of the Galaxy. This implies that even sources currently undergoing a low quiescent phase may contribute to the average X-ray Galactic output, if they have experienced a higher level of activity in the past. An important example is the supermassive black hole Sgr A* situated at the Galactic centre, which currently radiates at least eight orders of magnitude below its Eddington limit with a quiescent $2-10$ keV luminosity of $\sim 10^{33-34}$ ergs/s (e.g. Narayan et al., 1998; Baganoff et al., 2003). The scattering of the hard X-ray continuum radiation of Sgr A* by an individual molecular cloud (Sgr B2) was first observed by Revnivtsev et al. (2004). Studies of the recent history of Sgr A*'s activity through the reflected X-rays from the massive molecular clouds in its vicinity (first proposed by Sunyaev et al. (1993) and followed by Koyama et al. (1996); Murakami et al. (2000); Revnivtsev et al. (2004); Muno et al. (2007); Inui et al. (2009); Ponti et al. (2010); Terrier et al. (2010); Capelli et al. (2012); Nobukawa et al. (2011); Gando Ryu et al. (2012); Clavel et al. (2013)) suggest that the source experienced much more luminous phases in the past than currently observed (see Ponti et al. (2013) for a review). The past activity of the currently low quiescent source Sgr A* might therefore have significantly contributed to the cumulative X-ray output of the Galaxy, and hence to the diffuse GRXE component. In this work we ignore the contribution of this source and focus only on the contribution of XBs. We show in Fig. 2.3 the minimum luminosity required for the flux from this source

to outshine the contribution of the entire XB population at different positions $(x, y, z = 0)$ on the Galactic plane, estimated as

$$L_{SgrA^*}(x, y, z = 0) = 4\pi R^2_{SgrA^*} \times \sum_i \frac{L_i(\nu)}{4\pi R_i^2} \tag{2.14}$$

where R_{SgrA^*} is the distance from Sgr A* to the point $(x, y, z = 0)$, R_i is the distance from the XB source of luminosity L_i to the same point. This is shown in Fig. 2.3 for the case of observed XBs. Near the Galactic centre, a luminosity of $\gtrsim 10^{37}$ ergs/s from Sgr A* would be enough to become comparable with the illumination from X-ray binaries. On the outskirts of the Galaxy, on the other hand, Sgr A*, or some other ultra-luminous source near the Galactic centre, can be ignored as long as its luminosity is $\lesssim 10^{39-40}$ ergs/s.

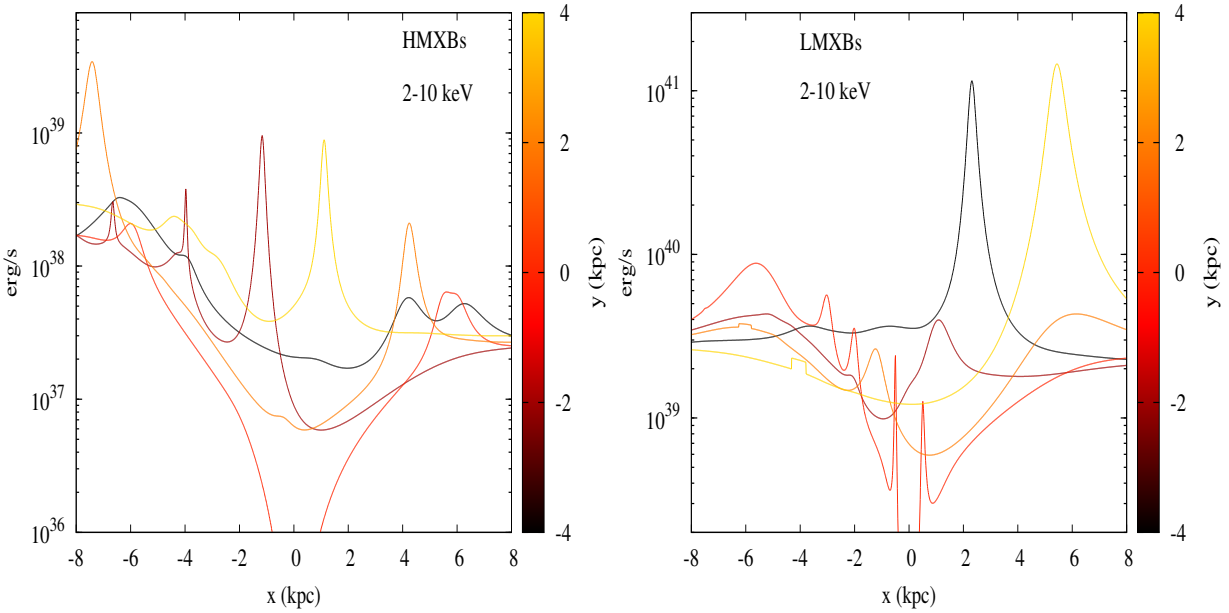

Figure 2.3: Minimum Sgr A* luminosity required for the source's flux to be higher than the total HMXBs (*left panel*) and LMXBs (*right panel*) contribution at different positions on the Galactic plane.

2.2.4 Scattered X-rays' ISM volume emissivity

The total volume emissivity per steradian, $\epsilon_{\rm XBs}$, of the gas due to illumination by Galactic X-ray binary sources at a distance s from the observer along the line of sight (l, b) is given by

$$\epsilon_{\rm XBs}(s, \nu) = \sum_Z \sum_i \frac{L_i(\nu)}{4\pi R_i^2(s)} \left(\frac{{\rm d}\sigma}{{\rm d}\Omega}(s, \nu) \right)_Z n_Z(s), \tag{2.15}$$

where the sum is computed over the X-ray sources i and elements Z contributing to the scattering, R_i is the distance of the source with luminosity L_i from the scattering point,

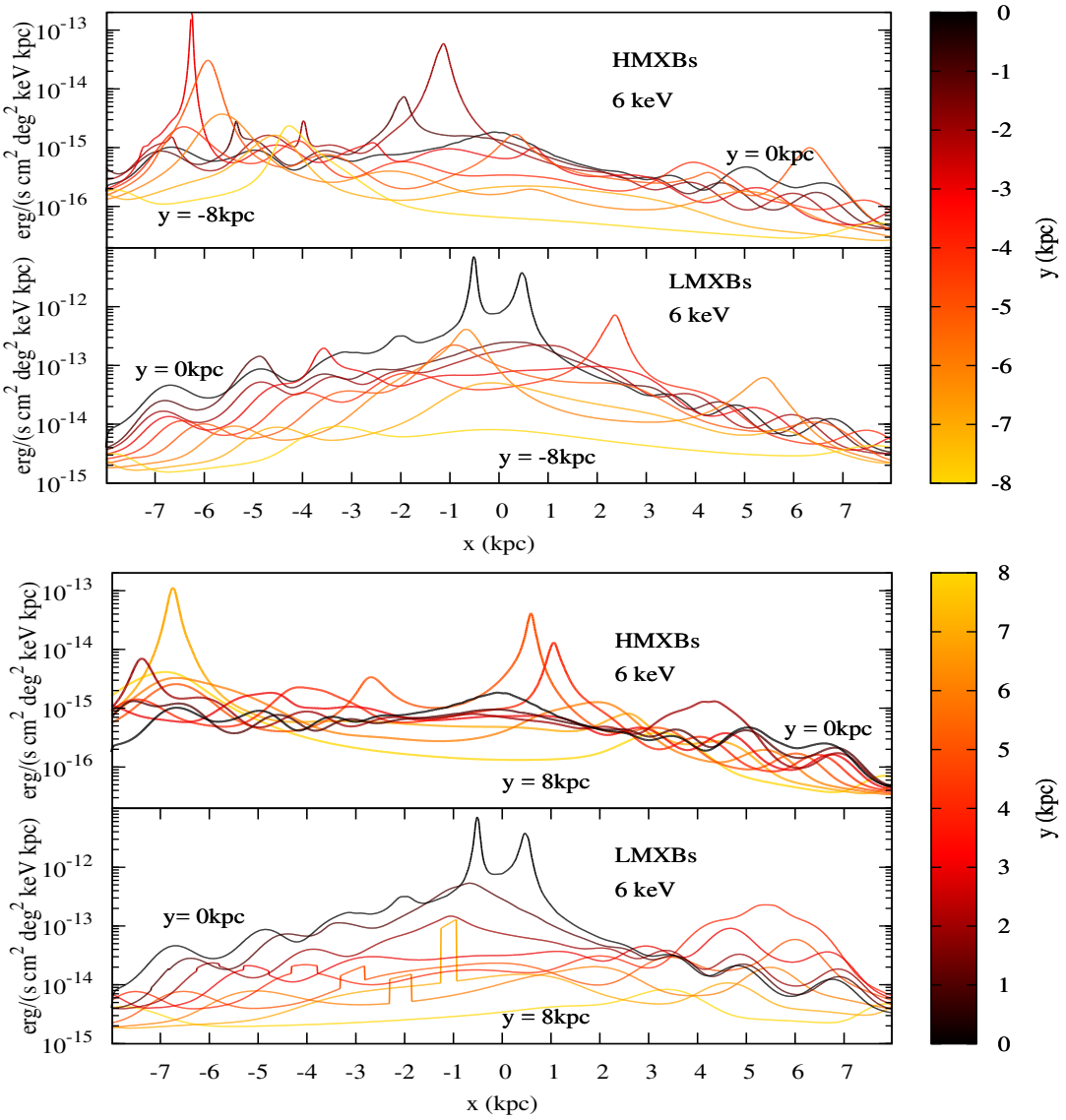

Figure 2.4: Profiles of the volume emissivity per deg^2 in our direction on the Galactic plane due to the observed sources used in our calculations, at different distances from the Galactic centre (Sun's position (-8 kpc, 0, 0.015 kpc)). Units were chosen so that if this emissivity is integrated over 1 kpc it is numerically equal to the observed flux. Proximity effects in the vicinity of sources are clearly visible. The concentration of LMXBs in the Galactic bulge results in a steady decrease in the overall profile of the volume emissivity from these sources away from the Galactic centre. This is not the case for HMXBs because of their distribution along the Galactic disk. Discontinuities in the LMXBs profiles in the positive y-range are caused by temporal constraints in the illumination of its surroundings by the very bright source GRS 1915+105 (located at $(-0.27\text{kpc}, 7.83\text{kpc}, -27\text{pc})$), which was not observed during 1970-1992 and is assumed to have been absent before 1992.

$(\mathrm{d}\sigma/\mathrm{d}\Omega)$ is the differential scattering cross section including Rayleigh and Compton scattering, and n_Z is the number density distribution of the element Z. The total differential cross section is computed as a function of the position along the line of sight s as well as of the radiation energy, since the angle at which radiation from a given source is to be scattered to reach the observer will depend on the position at which the scattering occurs. Because of the low optical depth, the contribution of radiation that undergoes multiple scatterings before reaching the observer is assumed to be negligible, and we therefore use a single-scattering approximation. The volume emissivity per unit solid angle in the Galactic plane is plotted in Fig. 2.4 using observed data. From Eq. 2.15 we expect proximity zones near individual sources where the flux peaks sharply, as clearly seen in Fig. 2.4. Scattering of X-rays in these proximity zones will result in X-ray halos around each source, similar to the dust halos observed around many X-ray sources (Overbeck, 1965; Trümper & Schönfelder, 1973; Rolf, 1983; Predehl & Schmitt, 1995) at angles $< 1^\circ$ but extending to much larger angles. The profile is sharply peaked if the source is in the Galactic plane and the slice through the plane crosses the source. If, on the other hand, the source is above or below the plane, the profile is broader, as expected from the geometry. LMXBs dominate in the centre of the Galaxy because they are concentrated in the bulge, while in the disk and near the spiral arms HMXBs are dominant.

As discussed in Section 2.2.3, we also include the scattering of the stellar GRXE in our calculations. The volume emissivity per unit solid angle due to scattering of this radiation at a distance s from the observer along the line of sight (l, b) is given in this case by:

$$\epsilon_{\mathrm{stellar}}(s,\nu) = \sum_Z \iiint_V \frac{\rho_{\mathrm{GRXE}}(x,y,z) f(\nu)}{4\pi d^2(x,y,z,s)} \times \left(\frac{\mathrm{d}\sigma}{\mathrm{d}\Omega}(s,\nu)\right)_Z n_Z(s)\mathrm{d}V, \tag{2.16}$$

where ρ_{GRXE} is given in units of erg/cm^3, $d(x, y, z, s)$ is the distance from any point (x, y, z) in the Galaxy to the scattering point, and $f(E)$ is the normalised spectral energy density taken from the GRXE spectrum given in Revnivtsev et al. (2006) and Krivonos et al. (2007a).

2.3 Results

The contribution of the scattered intensity is expected to be most significant at low latitudes where the interstellar gas is concentrated. We therefore present the results in the form of longitude profiles of the total scattered intensity along the Galactic plane ($b = 0^\circ$), in energy ranges 3 - 10, 10-20, 17-25 and 25-60 keV, chosen to allow comparison with the RXTE and Integral observations of GRXE and future observations of Nuclear Spectroscopic Telescope Array (NuSTAR) (Harrison et al., 2013) and hard X-ray telescopes onboard Astro-H (Tajima et al., 2010) and ART-XC onboard Spectrum-RG (Pavlinsky et al., 2008) satellites.

Current observations of the GRXE do not have a high enough angular resolution to allow a direct comparison with the scattered profile. We therefore make use of the relation between the GRXE emission and the Galactic stellar distribution first studied in Revnivtsev et al. (2006) to compare the diffuse scattered component with the GRXE of stellar origin, as discussed below.

We use the relation between the GRXE's surface brightness and the extinction-corrected near-infrared emission found by Revnivtsev et al. (2006):

$$I_{3-20\mathrm{keV}}(10^{-11}\mathrm{ergs}^{-1}\mathrm{cm}^{-2}\mathrm{deg}^{-2}) = 0.26 \times I_{3.5\mu\mathrm{m}}(\mathrm{MJy/sr}) \tag{2.17}$$

and Krivonos et al. (2007a):

$$F_{17-60\mathrm{keV}} = (7.52 \pm 0.33) \times 10^{-5} F_{4.9\mu\mathrm{m}} \tag{2.18}$$

in the 3-20 and 17-60keV ranges, respectively, to model the stellar GRXE component at different positions on the sky. Full-sky infrared maps are available from the Cosmic Background Explorer's Diffuse Infrared Background Experiment (COBE/DIRBE) experiment. We use the zodi-subtracted mission average map available on the LAMBDA archive at `http://lambda.gsfc.nasa.gov`. To account for interstellar extinction in the infrared data, we use the method followed in Krivonos et al. (2007a) based on the assumption that the ratio of intrinsic surface brightness in different infrared bands is uniform over the sky. This in effect is equivalent to the assumption that the average spectrum of the infrared sources is the same in all directions, or that the average relative population of different types of stars in different regions of the Milky Way is the same. The 'true value' of the ratio under this assumption can be estimated from the lines of sight at which the extinction is negligible and the contribution from the extragalactic sources is not important. We use this method because most of the publicly available extinction maps account for the total extinction in our Galaxy and are useful only in the case of extragalactic sources. For the Galactic sources the extinction, in addition to direction, would also depend upon how far away the sources are from the observer. The extinction coefficient for emission at wavelength λ can be calculated, following Krivonos et al. (2007a), as

$$A(l,b) = \frac{-2.5}{A_{1.25\mu\mathrm{m}}/A_\lambda - 1}\left[\log_{10}\frac{I_{1.25\mu\mathrm{m}}}{I_\lambda} - \log_{10}\frac{I^0_{1.25\mu\mathrm{m}}}{I^0_\lambda}\right], \tag{2.19}$$

where the "true" value of the ratio is estimated by averaging all measurements for 1° around $b \sim 30^\circ$ and A_λ/A_V values are taken from Rieke & Lebofsky (1985).

We show our results for both the observed (Fig. 2.5 and 2.6) and simulated (Fig. 2.7) source catalogs. In each plot, we distinguish the contribution of scattered HMXBs, LMXBs and stellar GRXE radiation, and compare this with the direct stellar GRXE contribution in each energy band. From these plots, we can make the following observations:

- The contribution of HMXBs along the Galactic disk and of LMXBs around the Galactic bulge, which would be expected from the distribution of these sources in the Galaxy, is clearly recognisable.

- Proximity effects in the vicinity of bright sources are also visible. The sources contributing the most to the scattered components are clearly detectable and marked as peaks in the profiles. The peaks appear to be sharper for sources in the Galactic plane and broader for sources significantly above or below the plane. Note that when the line of sight crosses a source, the sharpness of peaks is limited by the angular resolution of the calculation, which is $5'$ for these plots. A list of the observed LMXBs and HMXBs that are responsible for some of the brightest peaks in the scattered GRXE profiles (Fig. 2.5) are listed in Table 2.2.

- The combined concentration of both gas and HMXB sources in spiral arms results in a visible increase in the scattered GRXE emission at lines of sight tangential to these structures (see for example the line of sight tangential to the Scutum-Crux spiral arm at $l \sim -60^{\circ}$).

- The profiles drop sharply toward the Galactic anti-centre, reflecting the decrease in the ISM column density.

- The softer spectrum of LMXBs compared to that of HMXBs results in a more evident drop in the reflected intensity in the 10-20 keV range then for the former class of XBs.

- The intensity of the scattered GRXE emission in each band is proportional to the total luminosity of the corresponding X-ray sources in that energy range. We take for example the case of the scattered stellar GRXE. The luminosity of the stellar GRXE in the 3-20 keV range is $\approx 1.4 \times 10^{38}$ erg/s (Revnivtsev et al., 2006), which is lower than the luminosity of LMXBs ($\approx 2.43 \times 10^{39}$ erg/s), but higher than the luminosity of HMXBs ($\approx 9 \times 10^{37}$ erg/s). This is clearly reflected in the relative emission of the scattered profiles in Fig. 2.5. In the 17-60 keV energy range, on the other hand, the luminosity of the stellar GRXE is 3.7×10^{37} erg/s (Krivonos et al., 2007a), which is a factor of ~ 5 lower than the luminosity of LMXBs (1.9×10^{38} erg/s) and a factor of ~ 2 lower than the luminosity of HMXBs (6.2×10^{37} erg/s). We would therefore expect the scattered stellar GRXE to be subdominant in this range, as is indeed evident in the plot for this range (see Fig. 2.6).

In order to quantify the relative contribution of the scattered emission to the stellar GRXE, we show the ratio of the scattered emission to the GRXE inferred from near-infrared data. We show this separately for observed (Fig. 2.8) and simulated (Fig. 2.9) sources respectively.

In the case of observed sources, the scattered X-rays contribute $10 - 30\%$ over most of the Galaxy, with a contribution as high as 40% near the most luminous sources in the 3-20 keV energy range. The diffuse component in the 17-60 keV range contributes, on the other hand, $\sim 10\%$ or less, which is lower but still non-negligible.

In the case of the simulated catalog, the scattered X-rays from the Monte Carlo XBs account for almost all of the GRXE in the Galactic plane in the 3-20 keV range. This

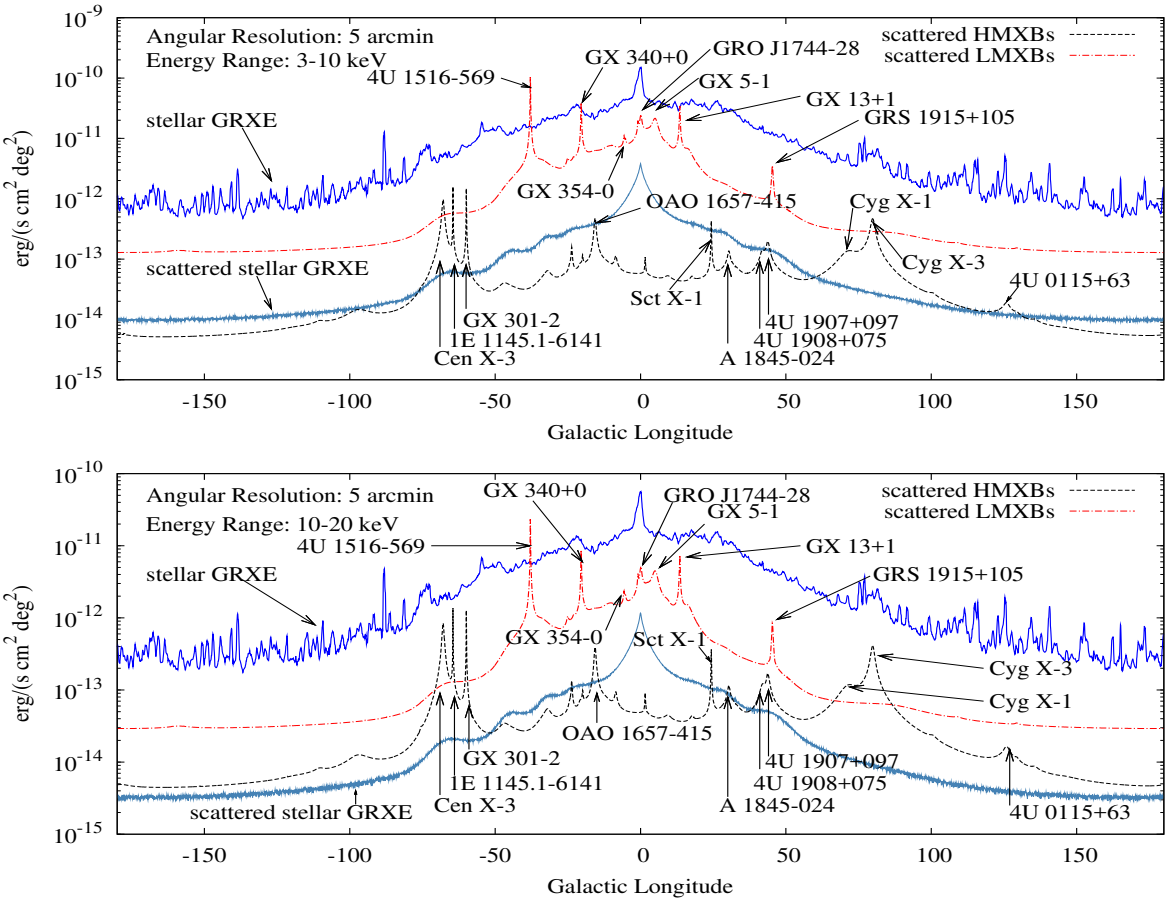

Figure 2.5: Longitude profiles of scattered XB radiation in comparison with a near-infrared-inferred GRXE profile in energy ranges 3-10 and 10-20 keV for observed sources. The sum of the scattered component is 10-30% of the stellar contribution to the GRXE. Data for the sources responsible for the labelled peaks are listed in Table 2.2.

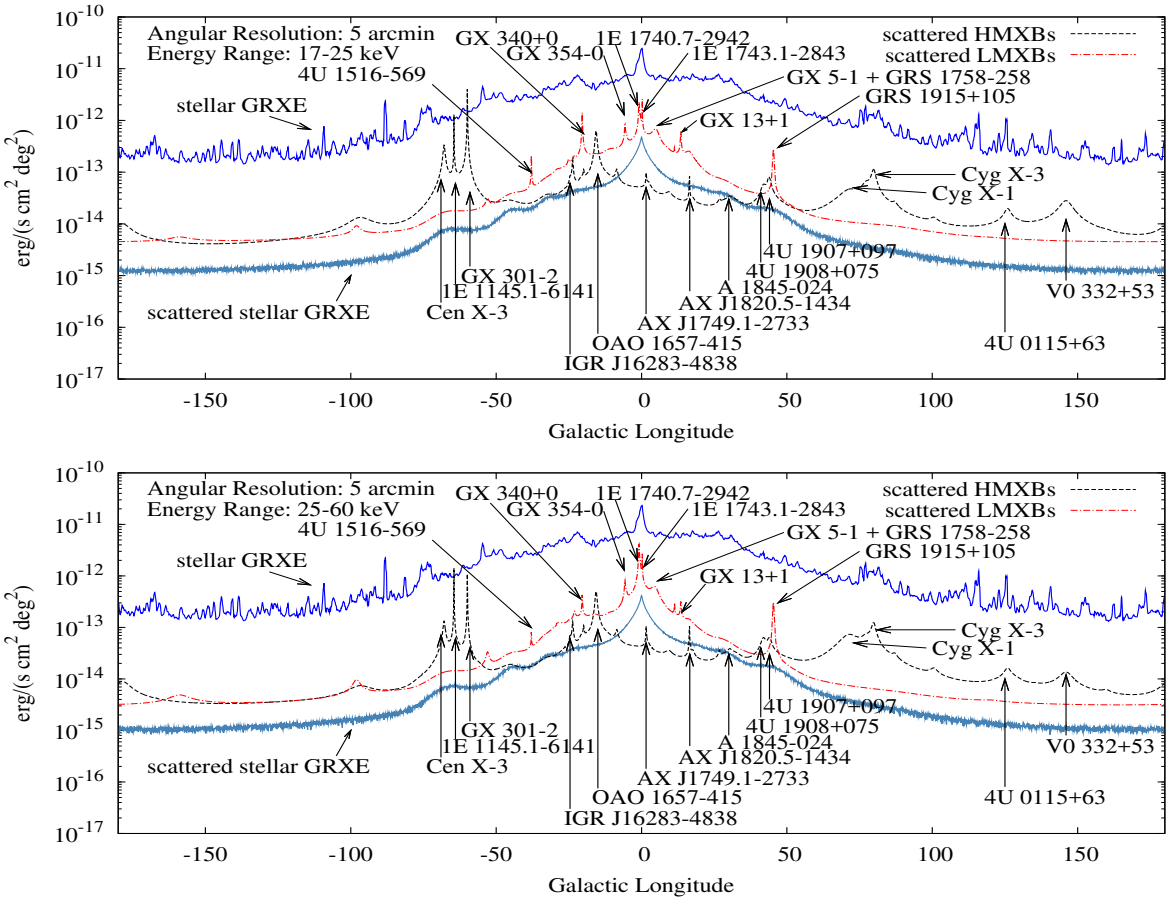

Figure 2.6: Longitude profiles of scattered XB radiation in comparison with a near-infrared-inferred GRXE profile in energy ranges 17-25 and 25-60 keV for observed sources. Data for the sources responsible for the labelled peaks are listed in Table 2.2.

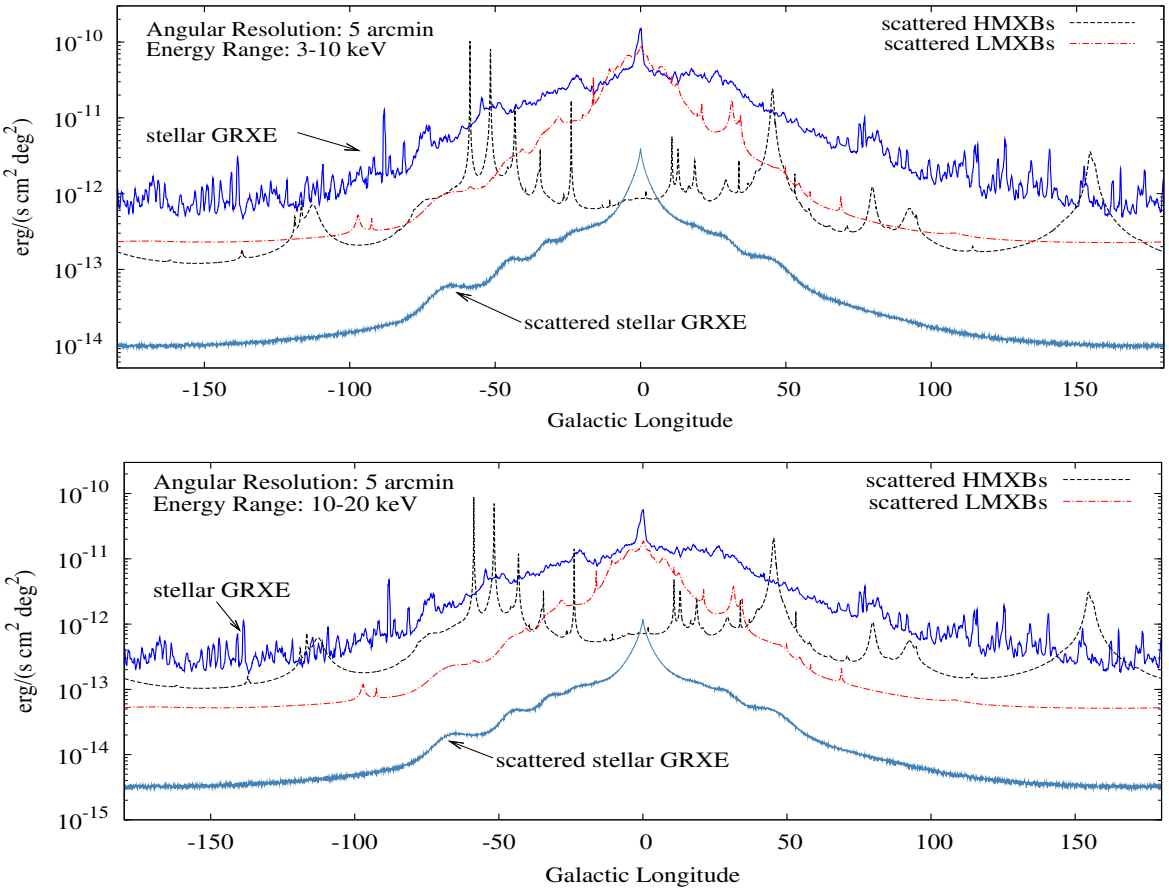

Figure 2.7: Longitude profiles of scattered XB radiation in comparison with near-infrared-inferred GRXE profile, in energy ranges 3-10 and 10-20 keV for Monte Carlo sources. If our Galaxy was on average more luminous in X-rays during the last several thousand years compared with the present, then the scattered component of the GRXE could be as bright as the stellar component. In reality, the scattered component strongly depends on the appearance of just a few new bright sources with luminosities close to the Eddington limit for a neutron star.

seems to suggest that the hypothesis that our Galaxy is on average more similar to other galaxies, and therefore significantly more luminous than the current observations of the X-ray sources in the Galaxy would suggest, contradicts the resolution of 80-90% of the emission into point sources by Revnivtsev et al. (2009). This is actually not the case, as discussed in the next section.

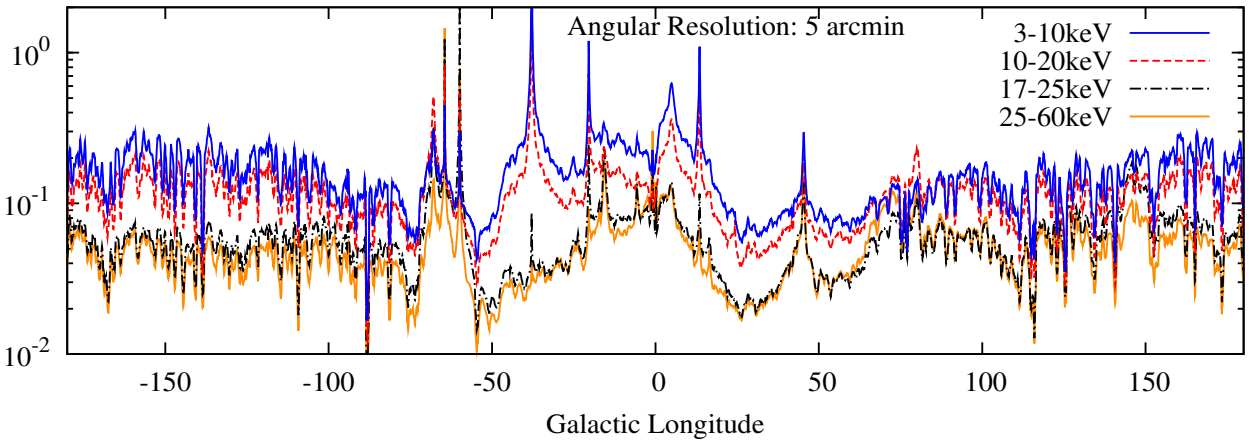

Figure 2.8: Ratio of scattered X-ray radiation (including HMXBs, LMXBs, and near-infrared-inferred low-luminosity sources) to the near-infrared-inferred GRXE profile for observed sources for the energy ranges (from top to bottom) 3-10 keV, 10-20keV, 17-25keV, and 25-60 keV. The average spectrum of the LMXB sources in our calculations is significantly softer than the GRXE spectrum observed by RXTE and Integral (Revnivtsev et al., 2006; Krivonos et al., 2007a). As a result, the contribution of the scattered component to GRXE decreases at energies above 10 keV.

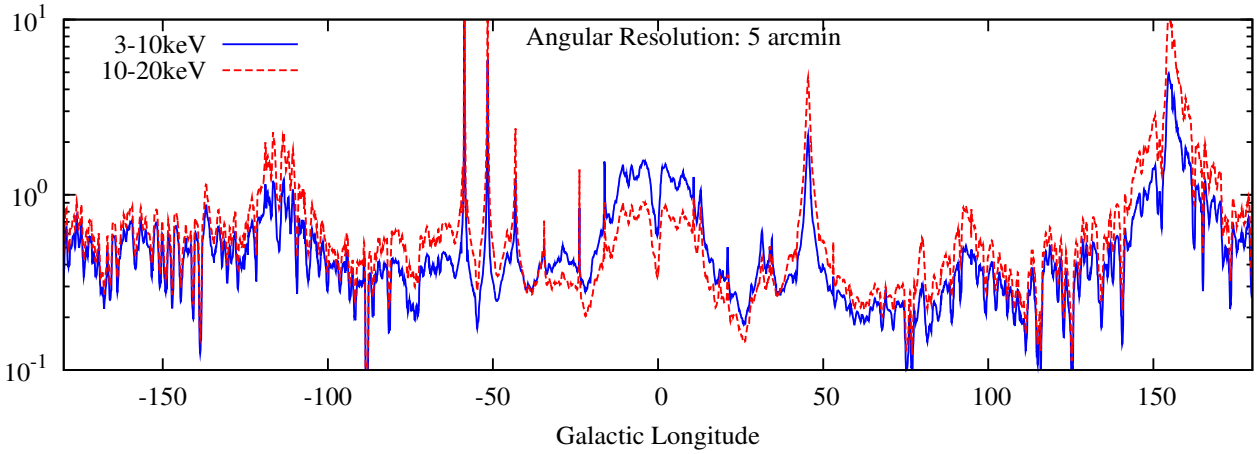

Figure 2.9: Ratio of scattered X-ray radiation (including HMXBs, LMXBs, and near-infrared-inferred low-luminosity sources) to the near-infrared-inferred GRXE profile for the Monte Carlo sources.

Table 2.2: List of sources responsible for peaks in the scattered GRXE longitude and latitude profiles, ranked by 2-10keV luminosity.

Source	l (°)	b (°)	D (kpc)	lumi. 2-10 keV (erg/s)	lumi. 17-60 keV (erg/s)	D	lumi. 2-10 keV	lumi. 17-60 keV
4U 1516-569	322.12	0.037	9.2	3.31×10^{38}	5.91×10^{35}	(4)	(3)	(1)
GRS 1915+105	45.36	-0.22	11	2.96×10^{38}	4.88×10^{37}	(4)	(3)	(1)
GX 5-1	5.079	-1.019	7.2	1.42×10^{38}	3.83×10^{36}	(7)	(3)	(1)
GX 340+0	339.59	-0.08	11	1.41×10^{38}	5.42×10^{36}	(7)	(3)	(1)
GX 13+1	13.52	0.106	7	4.32×10^{37}	8.03×10^{35}	(5)	(3)	(1)
Cyg X-3	79.85	0.7	7.2	2.43×10^{37}	1.01×10^{37}	(2)	(3)	(2)
GRO J1744-28	0.0445	0.301	8.5	1.57×10^{37}	-	(3)	(3)	-
GX 354-0	354.30	-0.15	5.3	7.17×10^{36}	1.89×10^{36}	(4)	(3)	(1)
Cen X-3	-67.9	0.33	5.7	6.09×10^{36}	2.45×10^{36}	(2)	(3)	(2)
GRS 1758-258	4.508	-1.362	8.5	5.90×10^{36}	5.67×10^{36}	(3)	(3)	(1)
1E1740.7-2942	-0.873	-0.105	8.5	5.03×10^{36}	3.85×10^{36}	(12)	(3)	(11)
Cyg X-1	71.34	3.07	1.86	4.01×10^{36}	3.90×10^{36}	(2)	(3)	(2)
OAO 1657-415	-15.63	0.32	7.1	1.88×10^{36}	4.87×10^{36}	(2)	(3)	(2)
4U 0115+63	125.922	1.029	8	1.27×10^{36}	2.88×10^{36}	(10)	(3)	(1)
1E 1145.1-6141	-64.5	-0.02	8.5	1.15×10^{36}	2.01×10^{36}	(2)	(3)	(2)
4U 1908+075	41.89	-0.81	7	1.06×10^{36}	9.66×10^{35}	(2)	(3)	(2)
GX 301-2	-59.9	-0.03	3.5	9.31×10^{35}	3.15×10^{36}	(2)	(3)	(2)
4U 1907+097	43.74	0.47	5	8.98×10^{35}	4.39×10^{35}	(2)	(3)	(2)
A 1845-024	30.4	-0.381	10	8.42×10^{35}	8.21×10^{34}	(7)	(3)	(1)
Sct X-1	24.34	0.066	10	7.50×10^{35}	-	(3)	(3)	-
V0 332+53	146.05	-2.194	7.5	1.03×10^{35}	1.11×10^{37}	(10)	(3)	(1)
1E 1743.1-2843	0.25	-0.026	8	-	4.54×10^{35}	(8)	-	(1)
XTE J1810-189	11.36	0.06	11.5	-	3.35×10^{35}	(6)	-	(1)

(1) Krivonos et al. (2012); (2) Lutovinov et al. (2013); (3) Grimm et al. (2002); (4) Jonker & Nelemans (2004); (5) Bandyopadhyay et al. (1999); (6) Markwardt et al. (2008); (7) Grimm et al. (2002); (8) Porquet et al. (2003b); (9) Sidoli et al. (1999); (10) Negueruela et al. (1999); (11) Krivonos et al. (2007a); (12) White & van Paradijs (1996).

2.3.1 Comparison with the deep survey region of Chandra

In the case of a Galactic XB population more similar to that of other galaxies, the scattered component should dominate the stellar GRXE on the plane of the Galaxy. This may seem to be inconsistent with the results of Revnivtsev et al. (2009), who resolved $80 - 90\%$ of the GRXE into point sources, suggesting that the average X-ray luminosity of our Galaxy should be lower than the one assumed in the simulated catalogue.

This apparent discrepancy is however resolved by considerations of the different scale heights of the scattered and stellar GRXE components. The field of view in which the emission was resolved was in fact located at latitude $b = -1.42°$. As discussed earlier (see Section 2.2.2), the scale height of the ISM, which the scattered GRXE is expected to follow, is much lower ($\sim 0.6°$). We therefore expect the diffuse component of the GRXE to be significantly smaller at this latitude than on the Galactic plane.

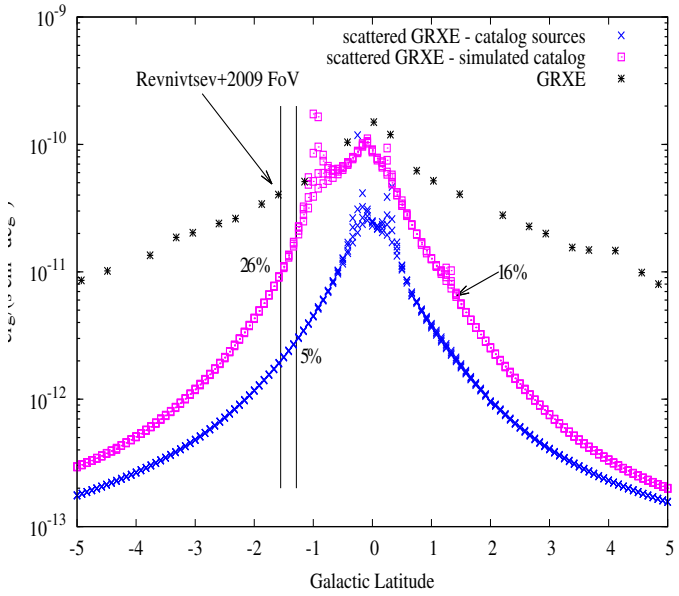

Figure 2.10: Latitude profiles of scattered XB radiation in comparison with the near-infrared-inferred GRXE profile in the energy range 3-10 keV for the field of view of 16×16 arcmin centered at $l = 0.08°$, $b = -1.42°$. In this region between 80 and 90 % of the GRXE has been resolved into point sources (Revnivtsev et al., 2009). Percentages quoted show the fractional contribution of the diffuse GRXE component in each case. Because of the coincidental presence near this field of view of a luminous simulated source, we also quote the same value on the other side of the Galactic plane in the case of Monte Carlo sources.

To illustrate this, we plot the latitude profile at $l = 0.08°$, corresponding to the observation direction of Revnivtsev et al. (2009), and compare the GRXE profile inferred from near-infrared data (see Fig. 2.10).

At $b = -1.42°$, the scattered GRXE due to observed and simulated sources makes up only 5% of the GRXE in the former case and $\sim 26\%$ in the latter. Because a luminous

Monte Carlo source appears to coincidentally be located nearby, giving a higher than average flux in this direction, we can actually consider the contribution on the other side of the Galactic plane, at $b = 1.42°$, to be a more representative value, suggesting the cumulative contribution of the simulated sources at this latitude should be $\sim 16\%$.

The simulated scattered GRXE in both the observed and simulated catalogue cases is hence consistent with the results of Revnivtsev et al. (2009). We can therefore conclude that an X-ray luminosity of the Milky Way significantly higher than what would be expected from current observations is therefore fully consistent with GRXE observations. The hypothesis that the average X-ray luminosity of our Galaxy is significantly higher than indicated by current data can be tested by studies similar to that of Revnivtsev et al. (2009), but conducted in the Galactic plane.

Recently, Morihana (2012) and Iso et al. (2012) have claimed that the resolved fraction in this field of view may be closer to 50%, allowing for a significantly larger contribution from the diffuse component. The analysis of Suzaku satellite data by Uchiyama et al. (2013) also allows for a contribution from the scattered radiation to the GRXE consistent with our predictions for the simulated optimistic case.

2.3.2 Effect of molecular clouds on the scattered GRXE's morphology

The GRS provides data for the spatial distribution, size and average density of 750 molecular clouds in the Galactic plane in the latitude range $-1° \leq b \leq 1°$ and the longitude range $18° \leq \ell \leq 55.7°$. This survey covers a part of one of the most significant concentrations of molecular gas in the Galaxy that is roughly distributed in a ring-like structure about 4 kpc from the Galactic centre (Stecker et al., 1975; Cohen & Thaddeus, 1977), although it may just be a spiral arm misinterpreted as a molecular ring (Dobbs & Burkert, 2012). We assume that the density of each individual cloud is constant throughout the object. The total H2 mass of the clouds in the GRS is 3.5×10^7 $M_\odot$.

We account for the absorption of X-rays in the molecular cloud using photoabsorption cross sections from Morrison & McCammon (1983). Scattering of X-rays from XBs on molecular clouds, which contain only a fraction of the total gas, gives a significant but patchy contribution to the GRXE. Part of the reason for this is that molecular clouds are dense and occupy a small volume (and angular area on the sky). Locally, along the lines of sight that intersect molecular clouds, they dominate the much smoother contribution from HI. In addition, there is a factor of 2 enhancement over atomic hydrogen (with same number density of H atoms) because of Rayleigh scattering for small scattering angles. We show the results after including the molecular clouds in the GRS instead of smooth distribution of molecular gas in Fig. 2.11. The molecular clouds are very obvious in these maps. This is even clearer in the latitude profiles shown in Fig. 2.12 along the direction tangent to the Scutum-Crux spiral arm of the Milky Way and the longitude profiles shown in Fig. 2.13. Even at relatively high latitudes, the molecular clouds are able to significantly contribute, locally, to the GRXE.

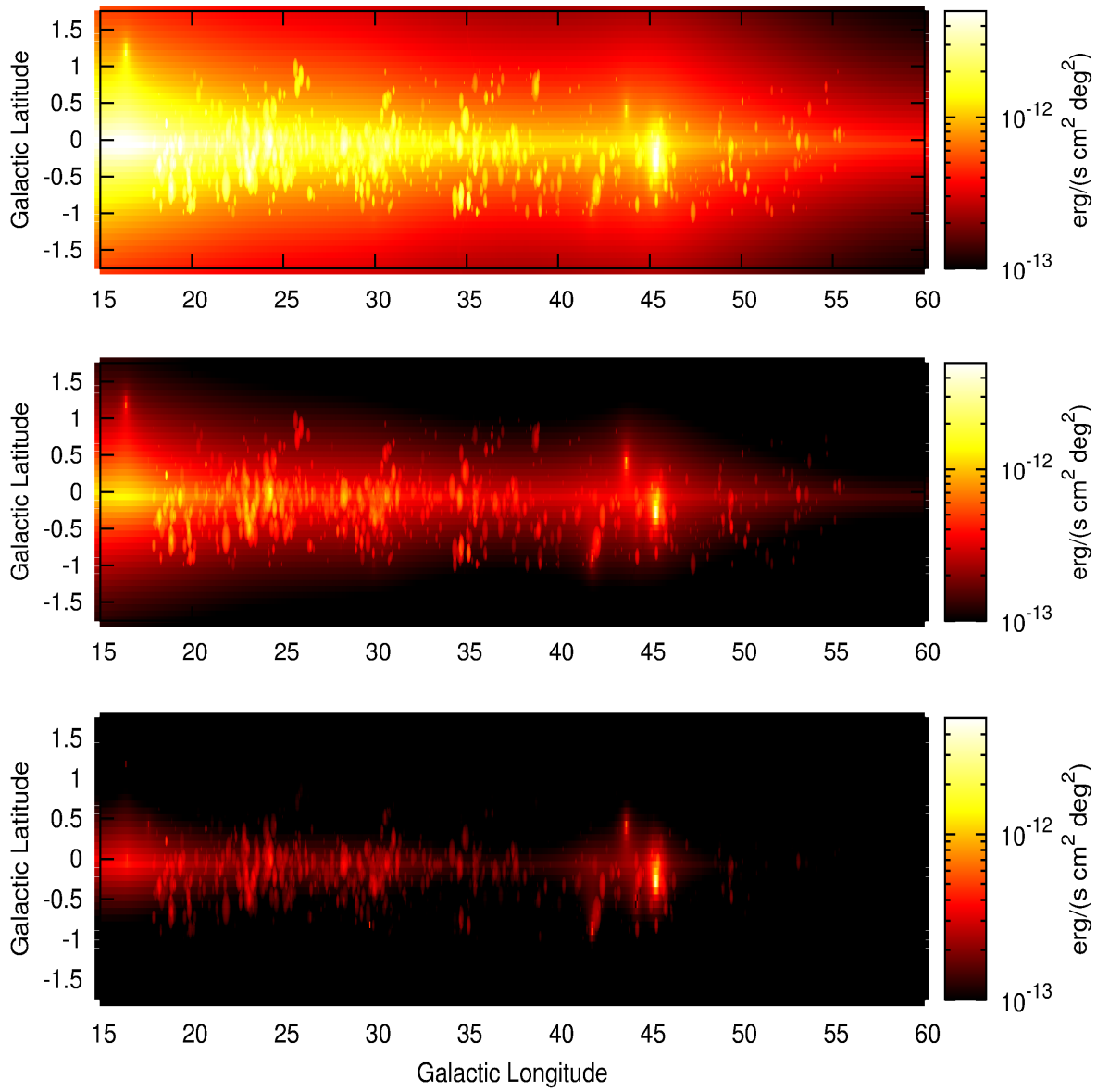

Figure 2.11: Maps of diffuse X-ray emission from the ISM with HI modelled as a smooth disk and H2 using data from the Galactic Ring Survey in the energy ranges 3-10 keV *(top panel)*, 10-20 keV *(middle panel)* and 17-60 keV *(bottom panel)*. Giant molecular clouds are immediately evident.

This suggests that at high angular resolution, where we can resolve the molecular clouds, there should be significant fluctuations in the diffuse component of the GRXE, which would encode information about the distribution of molecular clouds in the Galaxy. The comparison of their contribution to the near-infrared-inferred GRXE is given in Fig. 2.14. The molecular clouds are evident as narrow peaks on small scales, in addition to broader peaks from the presence of luminous X-ray sources, and locally they are responsible for an increase of a factor of more than 2 in the diffuse component of GRXE compared with the average background.
We compare in Table 2.3 the results for the scattered flux from molecular clouds with the Advanced Satellite for Cosmology and Astrophysics (ASCA) (Tanaka et al., 1994) measurement of X-ray flux in the field of view of GMCs (Cramphorn & Sunyaev, 2002). The ASCA measurements provide an upper limit to the X-ray flux that might be produced by the scattering process. The scattered X-ray component is well below the limit set by ASCA. The X-ray telescopes Chandra and XMM-Newton (and Athena+ in the future) are significantly more sensitive than ASCA, which observed the giant molecular clouds in the Galactic plane for a relatively short time.

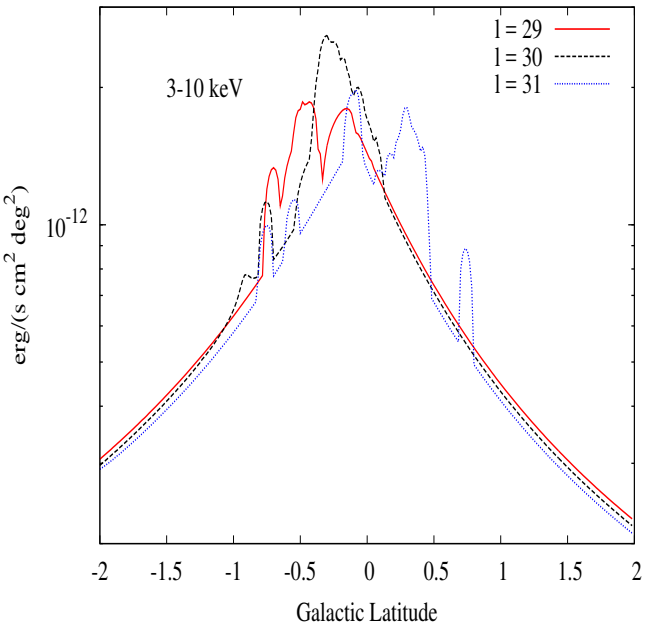

Figure 2.12: Latitude profile of scattered XB radiation near the line of sight tangential to one of the spiral arms (Scutum-Crux). The lines of sight passing through giant molecular clouds can receive a significantly higher contribution (than the average background) from the scattered X-rays.

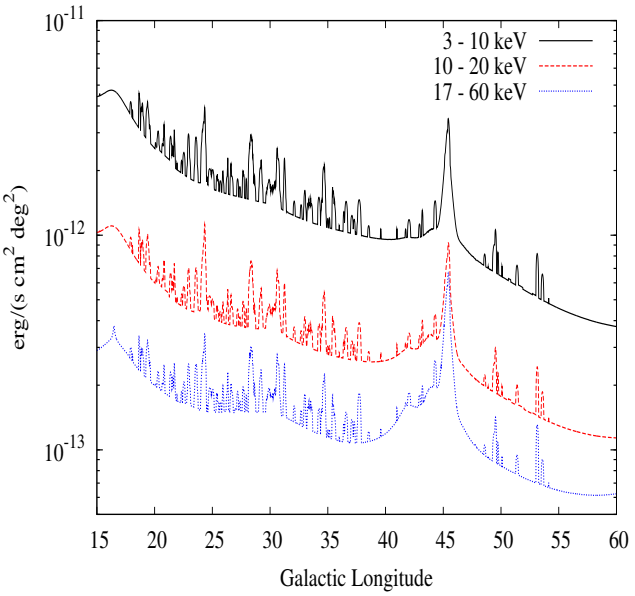

Figure 2.13: Comparison of longitude profiles of scattered XB radiation in different energy ranges including effects of molecular clouds (visible as narrow peaks in the profiles) for the energy ranges (from top to bottom) 3-10 keV, 10-20keV, 17-25keV and 25-60 keV.

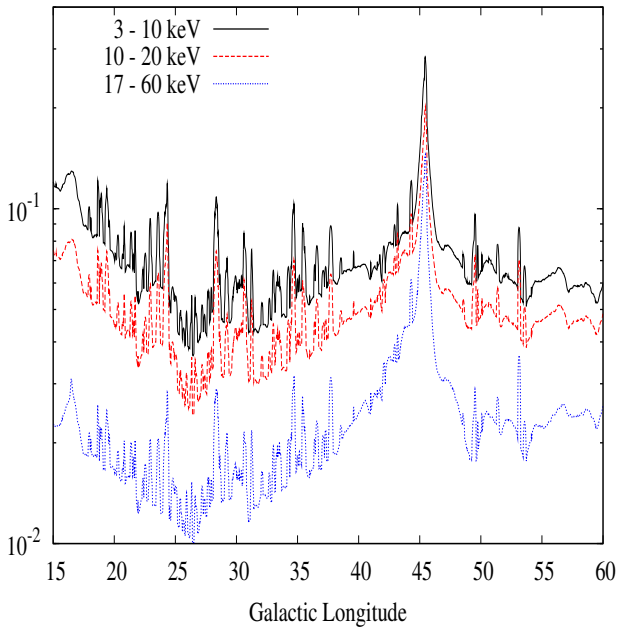

Figure 2.14: Ratio of longitude profiles of scattered XB radiation in different energy ranges including effects of molecular clouds (visible as narrow peaks in the profiles) to the near-infrared-inferred GRXE emission for the energy ranges (from top to bottom) 3-10 keV, 10-20keV, 17-25keV and 25-60 keV.

Table 2.3: Comparison of XB scattered flux (F_{scatt}) with ASCA measurements of 4-10keV flux (F_{ASCA}) in the field of view of 20 GMCs

GMC	F_{ASCA} (erg s^{-1} cm^{-2})	F_{scatt} (erg s^{-1} cm^{-2})	F_{scatt}/F_{ASCA}
003	1.9×10^{-11}	6.9×10^{-13}	0.036
014	1.5×10^{-11}	2.1×10^{-13}	0.014
059	1.7×10^{-11}	3.8×10^{-13}	0.022
080	1.5×10^{-11}	9.9×10^{-14}	0.0066
085	1.6×10^{-11}	1.8×10^{-13}	0.011
089	1.6×10^{-11}	3.0×10^{-13}	0.018
116	1.5×10^{-11}	6.1×10^{-14}	0.0041
122	1.8×10^{-11}	2.0×10^{-13}	0.011
128	1.7×10^{-11}	1.4×10^{-13}	0.008
151	1.4×10^{-11}	1.6×10^{-13}	0.011
152	1.4×10^{-11}	6.3×10^{-14}	0.0045
158	1.5×10^{-11}	1.0×10^{-13}	0.0067
162	1.5×10^{-11}	1.1×10^{-13}	0.0071
171	1.3×10^{-11}	2.9×10^{-13}	0.023
191	1.0×10^{-11}	7.2×10^{-14}	0.0072
193	1.0×10^{-11}	2.3×10^{-13}	0.023
201	9.1×10^{-11}	2.9×10^{-13}	0.0031
206	1.0×10^{-11}	1.6×10^{-13}	0.016
214	7.7×10^{-12}	3.1×10^{-13}	0.04
217	8.6×10^{-12}	1.1×10^{-13}	0.012

2.3.3 Luminosity

We calculate the luminosity/sr radiated in our direction from within a given latitude and longitude range in the sky $d\Omega$ (as opposed to the isotropic luminosity) for both the stellar GRXE and the scattered GRXE component as follows:

$$L_{\rm GRXE,stellar} = \frac{1}{4\pi}\iiint f(\nu)\rho_{\rm GRXE}(x,y,z)s^2 {\rm d}\nu {\rm d}s{\rm d}\Omega \tag{2.20}$$

$$L_{\rm GRXE,scatt} = \iint [\epsilon_{\rm XBs}(s,\nu) + \epsilon_{\rm stellar}(s,\nu)]s^2 {\rm d}\nu {\rm d}s{\rm d}\Omega, \tag{2.21}$$

where the total volume emissivity due to scattering $\epsilon(s,\nu)$ includes the contribution from both XB (Eq. 2.15) and low-luminosity stellar source (Eq. 2.16) components. The luminosity/sr profiles are plotted and compared in Fig. 2.15. The scattered radiation is on average $\sim 10\%$ as luminous as the stellar component of the GRXE in the inner $\sim 1^\circ$ of the Galactic plane.

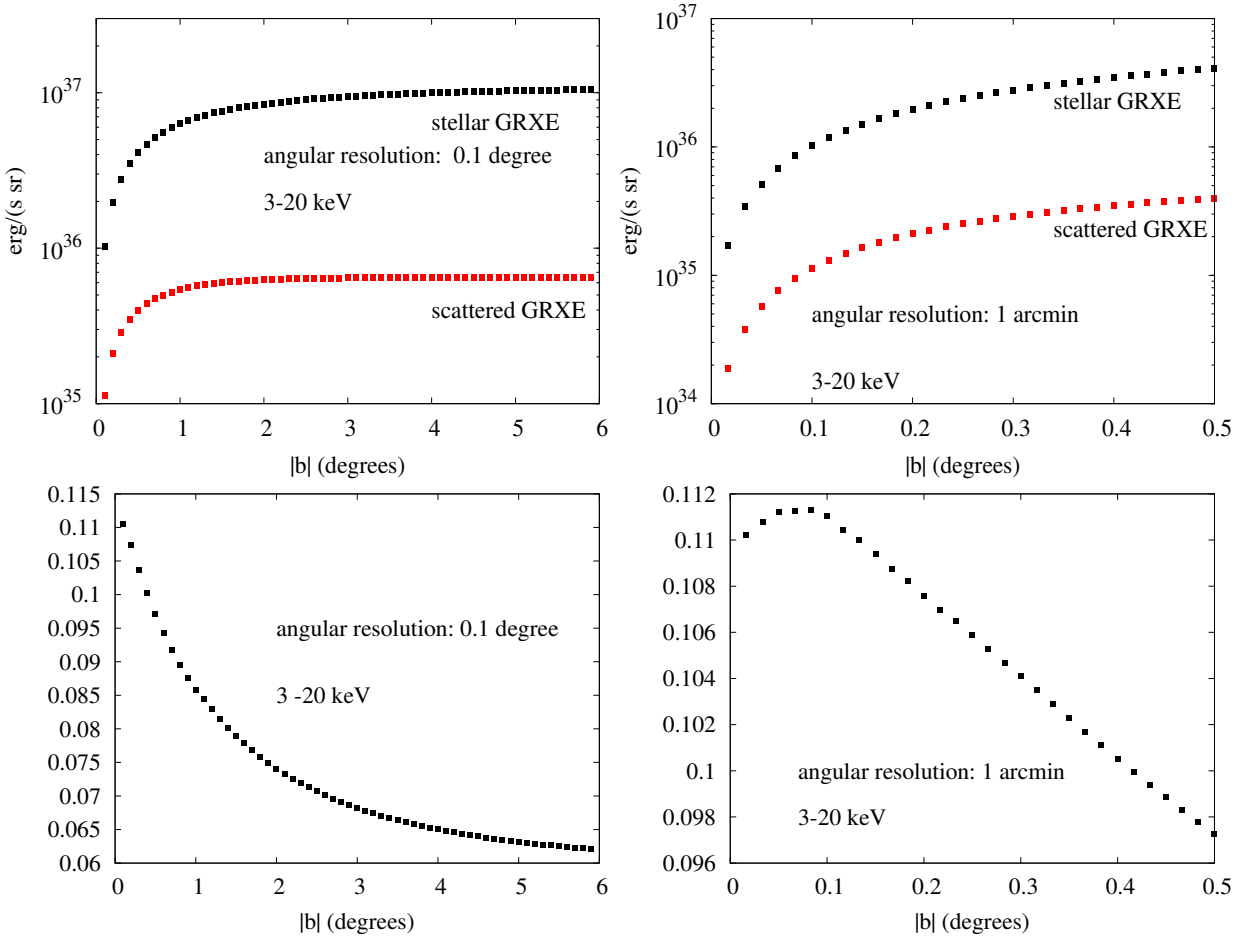

Figure 2.15: *Top panels*: Luminosity/sr radiated in our direction from the stellar GRXE and the scattered GRXE component (including stellar and XBs contributions) in the 3-20keV range integrated over the longitude range ($l < |180°$—) and latitude range $-b$ to b. The difference in the scale height of the scattered component compared with a GRXE of stellar origin is clearly visible. *Bottom panels*: Ratio of the two profiles. The peak in the ratio profile is caused by the elevation of the Sun above the Galactic plane by 15 pc.

2.4 Conclusions

Weak X-ray sources such as cataclysmic variables (CVs) and coronally active binaries are currently believed to be the main contributors to the GRXE. We investigate the scattering by the interstellar medium of X-rays produced by Galactic X-ray sources as a possible truly diffuse component of the GRXE emission. We include contributions from coherent scattering from molecular hydrogen, helium and heavy elements in addition to the atomic hydrogen. The scattering of X-rays from luminous sources results in bright regions around the sources, the proximity zones, similar to the dust halos, but extending to much larger scattering angles than the $\lesssim 1°$ for dust halos. The scattered photons from the ISM originating in the known X-ray binary sources and stellar sources in the Galaxy are able to

contribute, on average, $10 - 30\%$ of the flux currently identified as GRXE in the Galactic plane. The profile of the scattered intensity follows the distribution of gas in the Galaxy with a scale height of 80 pc (0.6° at 8 kpc distance), which is much sharper than the profile of stellar distribution with a scale height of ~ 130 pc. Therefore we expect the stellar point sources to dominate away from the Galactic plane, while the scattered X-rays would be concentrated within the central 1° of the plane. Molecular clouds locally enhance the scattered intensity, imprinting their morphology on the GRXE. The coherent scattering by electrons in the molecular hydrogen operates on a comparatively wide range of scattering angles at low energies than at high energies, making the scattered spectrum softer than the incident spectrum.

We only calculate the X-ray flux integrated over particular X-ray bands because this will be more readily observable in reasonable observation time with telescopes in operation now or expected in the near future, such as NuSTAR (Harrison et al., 2013), Spectrum-RG/ART-XC (Pavlinsky et al., 2008) and Astro-H (Takahashi et al., 2010). There is additional information in the spectrum of the scattered emission that may help to distinguish between the scattered GRXE and stellar GRXE. Of particular interest in this regard is the emission of fluorescent lines of neutral elements such as iron, sulphur and silicon. We have also assumed that the sources are persistent. The transient nature of most X-ray binary sources as well as extreme events such as gamma-ray bursts and giant flares from magnetars will leave unique signatures in the morphology of the scattered GRXE. We will consider these effects in a separate publication.

Compared with other galaxies, the Milky Way is underluminous in X-rays according to current observations. It is possible that the Milky Way is just going through a phase of low X-ray activity at present but was more luminous in the past. In particular, if the time-averaged luminosity of Milky Way is the same as inferred from averaged relations between X-ray luminosity and star formation rate/stellar mass of other galaxies, then the scattered component will on average contribute to more than 50% to the GRXE in the galactic plane and would dominate the stellar component in a significant part of the Galaxy. This hypothesis is allowed by current observations and is testable by observations of the Galactic plane with high angular resolution and sensitivity, similar to the study by Revnivtsev et al. (2009) below the Galactic plane.

Chapter 3

Contribution of XBs to the ISM heating

3.1 Heating processes in the ISM

The competition between different heating processes (e.g. by irradiation, cosmic rays, turbulent dissipation) and cooling processes (e.g. by atomic lines such as CII,OI, Ly-α) plays a crucial role in determining the multiphase structure of the interstellar medium, and hence the formation of molecular clouds and stars (Pikel'Ner, 1968; Field et al., 1969; McKee & Ostriker, 1977; Wolfire et al., 1995; Spitzer, 1978; Cox, 2005; Snow & McCall, 2006; McKee & Ostriker, 2007). The contribution of soft X-rays with energies $\lesssim 1$ keV is taken into account in standard calculations (Wolfire et al., 1995, 2003) by assuming a quasi-homogeneous X-ray background, which varies smoothly with distance from the Galactic center, arising from the Local Bubble, the Galactic halo and the extragalactic background. The contribution of photons with higher energies, on the other hand, is generally ignored in these models.

In the case of high-density gaseous regions, the heating from UV photons and soft X-rays is confined to the outer layers, where they are almost completely absorbed. Harder X-rays with energies $\gtrsim 1$ keV, on the other hand, would be able to penetrate dense regions of gas, such as GMCs, and significantly contribute to the heating of their interiors. The study of the gas heating resulting from illumination by hard sources could therefore represent an important step towards improving our understanding of the ISM heating mechanisms which determine its chemical evolution. As discussed in Chapter 2, X-ray binaries are the strongest sources of X-rays at these energies in galaxies similar to the Milky way, and should therefore have a significant effect on the structure and chemistry of the ISM. In Molaro et al. (2014) we estimated their possible contribution to ISM heating, as we report in this chapter.

3.2 Relative contribution from XBs

Energy deposition by X-rays takes place through photoionisation of tightly bound electrons in the atoms' innermost shells, as well as through inelastic scattering.

Photoabsorption of X-rays results in the release of a free electron in the ISM, as well as the emission of an additional electron through the Auger effect, with probability 1-Y (see Chapter 1). It is important to note that not all energy deposited in the gas this way will necessarily go into heating. Part of it will, in fact, be radiated away as low-frequency photons, produced by the consequent excitation, ionisation and recombination of the secondary electrons (Shull & van Steenberg, 1985). The efficiency of conversion between X-ray energy deposition and heating is therefore significantly dependent upon local conditions. In particular, the conversion will be more efficient if i) the ionisation fraction is large, so that most of the initially absorbed energy is dissipated via electron-electron collision and not through excitation, and ii) the hydrogen column density or dust opacity is so high that photons with energy Ly-α or higher cannot escape the region. Assuming either or both of these conditions hold, we can then assume that most of the energy deposited will be converted into heating.

In addition to the photoabsorption, hard X-rays also transfer energy to the gas through inelastic scattering with both free and bound electrons, due to the recoil effect. The average energy transferred by a photon of energy E is $E \times E/(m_{\rm e}c^2)$, where $m_{\rm e}$ is the mass of the electron and c is the speed of light in a vacuum (see e.g. Pozdnyakov et al., 1983). The average energy deposition rate is therefore given by:

$$\Gamma_{\rm recoil} = \int {\rm d}E F_{\rm X} \sigma_{\rm KN}\left(\frac{E}{m_{\rm e}c^2}\right)\left[1 - 2.2\left(\frac{E}{m_{\rm e}c^2}\right)\right], \tag{3.1}$$

where $F_{\rm X}$ is the specific X-ray flux in units of erg s^{-1} cm^{-2} keV^{-1} and $\sigma_{\rm KN}$ is the Klein-Nishina cross section (see Chapter 1), and where we include the lowest-order Klein-Nishina correction to the average recoil energy. Assuming a solar metallicity used in Morrison & McCammon (1983), the heating from recoil dominates the heating from photoabsorption at ≈ 28 keV. Because the photoabsorption cross section rapidly decreases with photon energy (see Chapter 1), and is therefore effectively negligible at this energy, the fact that recoil will only become comparable above ≈ 28 keV is indicative of the fact that its contribution to the heating should be very small. To demonstrate this, we take the example of the CXB. For this X-ray emission, the contribution of the recoil effect to the heating rate is $\approx 4 \times 10^{-32}$ erg/s/electron, counting free electrons as well as those bound in hydrogen and helium and in the outer shells of heavier elements, whereas its contribution due to photoabsorption is $\approx 2 \times 10^{-29}$ erg/s/electron, as shown in Fig. 3.1. The contribution due to recoil is indeed very small compared to the heating resulting from photoionisation. We therefore generally expect the recoil effect to be negligible, and ignore it in our calculations. It might however become important in the vicinity of hard X-ray sources.

Under the above assumptions, the energy deposition rate from X-rays at a point in the

Galaxy can be approximated by:

$$\Gamma_{\rm X} = \sum_i \frac{L_i(\nu)}{4\pi R_i^2}\left[\sigma_{\rm abs}(\nu) - \sum_Z \frac{n_Z}{n_H}\frac{E_{{\rm K}-\alpha,Z}}{E_\nu} Y_Z \times \sigma_{nl,Z}(\nu)\right], \tag{3.2}$$

where the sum computed is over the X-ray sources i, R_i is the distance of the source i to the point of absorption and L_i is its luminosity, $\sigma_{\rm abs}$ is the photoelectric absorption cross section given in Morrison & McCammon (1983), the sum Z over heavy elements, $\sigma_{{\rm abs},Z}$ is the analytic fit to the partial photoionisation cross section of the $n = 1, l = 0$ state of element Z as given in Verner & Yakovlev (1995), Y_Z is the K-α yield, $E_{{\rm K}-\alpha,Z}$ is the energy of the K-α line, and n_Z/n_H is the relative abundance for solar abundance estimates considered in Morrison & McCammon (1983). Above 10 keV we approximate the partial K-shell ionisation cross sections with that of Fe and Ni, which dominate the absorption cross section at these energies.

3.3 Results

We calculate the energy deposition rate from Galactic XBs using Eqn. 3.2 and the two catalogues of XB sources discussed in Chapter 2, one based on observed XB sources in the Milky Way, and one produced using a Monte-Carlo simulation of theoretical models of the XB population in the Milky Way.

For reference, we also plot the heating rate from the CXB, using the spectral fit of Gruber et al. (1999). The CXB, in contrast to X-ray binaries, uniformly heats the intergalactic medium everywhere, due to the isotropic nature of the emission. The energy density in CXB peaks around $z \sim 0.7 - 1$ (Ueda et al., 2003; Hasinger et al., 2005; Barger et al., 2005) and its contribution might therefore be significantly more important in galaxies at those redshifts. We compare these heating rates with that of cosmic rays, estimated to be - on average in the solar neighborhood - $\Gamma_{CR} \approx 10^{-28}$ erg/s/HI (Spitzer, 1978; Wolfire et al., 2003).

In Fig. 3.1, we consider the contribution of the XB sources from the observed catalog only. This, due to incompleteness issues, which affects in particular the estimate of the HMXBs contribution, will allow us to place a lower bound on the contribution of XBs to the heating of the ISM. We plot these energy deposition rates as profiles along the x-axis for different y-values in the Galactic plane, with coordinates for the Galactic centre at $(x, y) = (0, 0)$ and position of the Sun at $(x, y) = (-8, 0)$ kpc. From these plots, we can make the following observations:

- The contribution to ISM heating from these sources is highly variable in space, due to the rapid decrease of the source's X-ray flux with distance. The contribution of individual sources is therefore easily identifiable from proximity effects;

- The range of influence of individual sources extends quite far, up to a few kpc away for the most luminous ones;

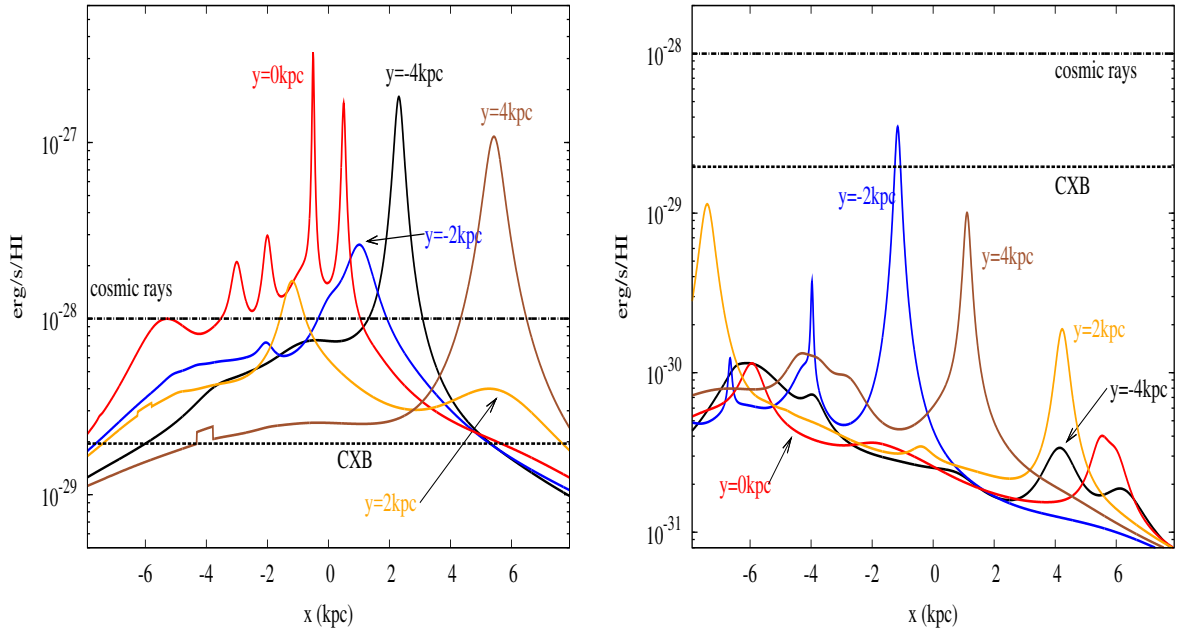

Figure 3.1: Heating of the ISM per hydrogen atom from photoabsorption of X-rays from observed LMXBs *(left panel)* and observed HMXBs *(right panel)*. For comparison, the contribution from cosmic rays following Spitzer (1978) and Wolfire et al. (2003) and CXB is also shown. The X-ray ($\gtrsim$ 1 keV) contribution dominates compared with the cosmic rays (assuming the same energy density as the solar neighborhood) in a significant part of the Galaxy.

- The X-ray heating contributed by LMXBs is comparable with and even stronger than the cosmic ray heating (assuming a solar neighbourhood energy density) in a significant part of the Galaxy, and may therefore be higher than other heating mechanisms typically considered. The contribution of HMXBs, more severely affected by incompleteness issues, is significantly lower.

In Fig. 3.2, we show maps of the heating rates on the Galactic plane comparing the contributions of the observed and Monte-Carlo-simulated catalogues. The latter, as discussed in Chapter 2, considers the case where the X-ray luminosity of the Milky Way is scaled to match the activity in the other galaxies. From these plots, we can clearly see that, despite the incompleteness issues mostly affecting the HMXBs in our observed catalog, the combined contribution of the two classes of observed XBs still dominates the cosmic rays contribution in a good part of the Galaxy. In the case of the Monte-Carlo simulated catalogues, on the other hand, the X-ray heating from XBs is found to dominate over the solar neighbourhood energy density of cosmic rays in almost the whole Galaxy.

X-ray heating contributed by XBs should therefore play at least some part in ISM heating in proximity of luminous sources. If the average activity of Milky Way is close to levels observed in other galaxies, which was considered by the simulated sources case, X-ray heating could on the other hand play an important role in the energetics of the

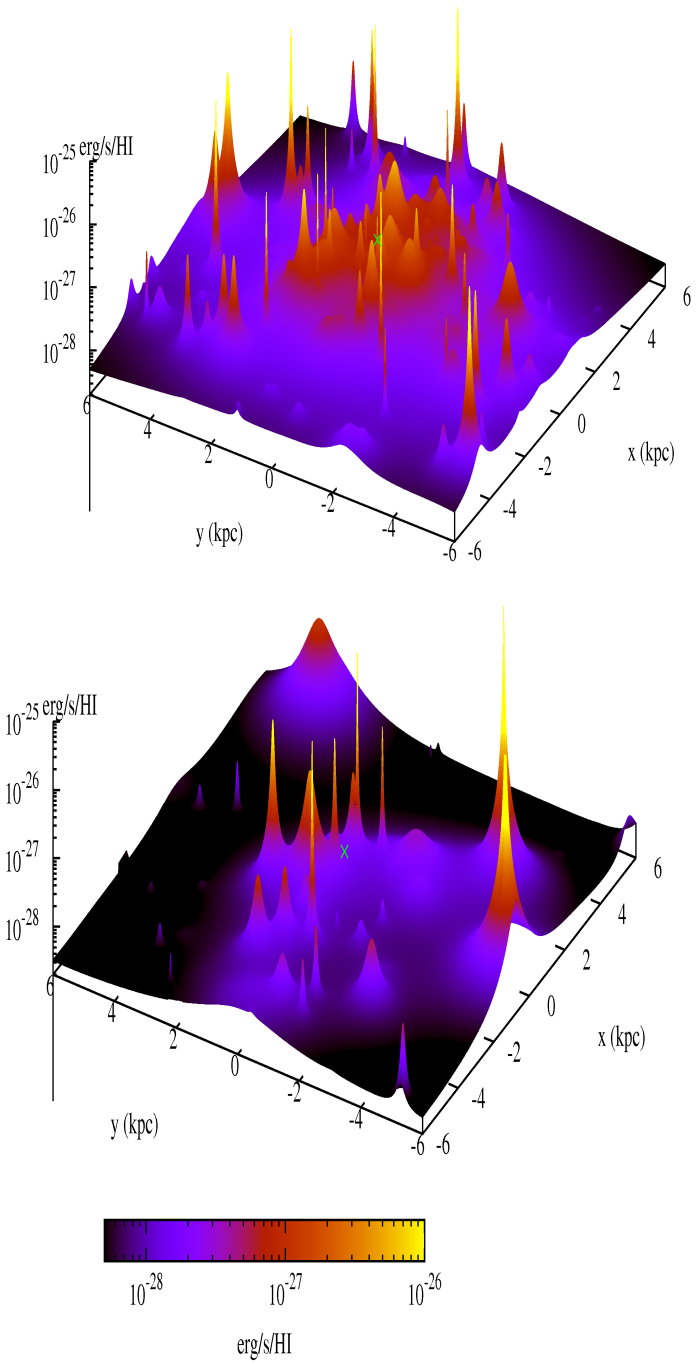

Figure 3.2: Three-dimensional maps of the heating of the ISM per hydrogen atom from photoabsorption of X-rays from LMXBs, HMXBs and CXB on the Galactic plane for Monte Carlo sources (*top panel*) and observed sources (*bottom panel*). In the outer regions of the Galaxy the heating rate approaches the lower bound of $\sim 1.9 \times 10^{-29}$ ergs/s/HI coming from absorbed CXB photons. The green cross indicates the position of the Galactic center in each map.

different phases of the ISM throughout the whole Galaxy. In star-forming galaxies, which have a much higher X-ray luminosity than even the simulated case for the Milky Way, the X-ray heating should therefore play a crucial role in the evolution of their ISM.

3.4 Conclusions

In conclusion, we find that the photoabsorption of hard ($\gtrsim$ 1 keV) X-rays emitted by luminous binary sources in the Galaxy can contribute significantly to the heating rate in the interstellar medium. The contribution of XBs to ISM heating should be highly variable both in space, due to proximity effects, and in time, because of the transient nature of most X-ray binaries. Using our catalogue of observed XBs, we find that the lower bound on the energy deposition rate contributed by these sources is comparable, and perhaps even higher than, that of cosmic rates in regions extending as far as a few kpc from the XB sources. In the case of the simulated XB catalog, which reproduces the expected luminosity of the Galactic XB population based on observations of other galaxies, this effect dominates the contribution of cosmic rays throughout the entire Galactic plane (Fig. 3.2).

This contribution of XBs to the heating has so far been ignored in the standard studies of the multiphase ISM (McKee & Ostriker, 1977; Wolfire et al., 1995, 2003), and could play a particularly important role in heating the interiors of GMCs, where UV photons or softer X-rays are unable to penetrate. This effect should be even higher in star-forming galaxies, which have a much higher X-ray luminosity than the Milky Way.

Chapter 4

Probing the clumping structure of GMCs through the spectrum, polarisation and morphology of X-ray Reflection Nebulae

4.1 Introduction

Understanding the internal structure of GMCs, which is driven by the interplay of turbulence, self-gravitation, and magnetic fields, is crucial when studying star formation processes in galaxies. It is, in fact, inside GMCs that dense, gravitationally unstable regions of gas, known as prestellar cores, form and collapse to give birth to stars (Williams et al., 2000).
Direct and exhaustive studies of the internal structure of GMCs are severely limited by issues of spatial and mass resolution when observing small-scale gas substructures. This is particularly true for GMCs that are located at a great distance, for example those found in the central molecular zone (CMZ), the region within the central ∼400 pc by ∼80 pc of the Galaxy (Langer et al., 2015). Dense regions inside GMCs, often studied as discrete objects loosely classified as clumps and cores, span spatial ranges of 0.2-2 pc and 0.02-0.4 pc and mass ranges of $10 - 10^3 M_\odot$ and $0.3 - 10^2 M_\odot$, respectively (Draine, 2011). At distances comparable to that from the Sun to the Galactic centre (GC), subarcsec angular resolution is therefore required to study these structures in detail. Despite the challenge that such high-resolution observations pose, obtaining a clear and complete picture of the overall properties of the clump and core populations in GMCs remains a significant effort in developing theoretical models of star formation (Williams et al., 2000).
In Molaro et al. (2015), we suggested a new method for probing global properties of the clump and core population in GMCs in the case where these act as X-ray reflection nebulae (XRNe), based on the study of their overall effect on the reflected X-ray signal.
The X-ray emission from XRNe is composed both of a continuum, shaped by the interplay

of scattering and absorption of the illuminating X-rays by atoms and molecules in the GMC, and by characteristic spectral features in the keV regime. The latter are caused by the emission of fluorescent photons by heavy elements, which follows the photoionisation of tightly bound electrons by hard X-rays. The inelastic scattering of fluorescent photons down to lower energies results in a characteristic increase in the continuum at energies lower than the fluorescent features - the so called "shoulder". This feature is most easily visible in the case of bright fluorescent lines, such as the Fe K-α line. Therefore, in the case of a small optical depth ($\tau < 1$), the intensity of the reflected continuum, fluorescent lines and shoulders will depend on $\sim \tau_T$, $\tau_{\rm abs}$ and $\tau_{\rm T} \times \tau_{\rm abs}$ respectively (where $\tau_{\rm T}$ and $\tau_{\rm abs}$ are the Thomson scattering and photoabsorption optical depths).
Fluorescent emission following illumination by X-rays was predicted by Sunyaev et al. (1993) in support of the claim that GMCs that surround the Galactic centre (GC) should act as XRNe of past flares of Sgr A*, the super-massive black hole located at the centre of the Galaxy. If this were the case, then part of the diffuse, hard, X-ray emission observed from these GMCs should be composed of a flux in the neutral Fe fluorescent line energy (6.4 keV), which is caused by the imprint of past, prequiescent activity of Sgr A* on the present-day (due to time delays) X-ray emission of GMCs that are located in its proximity. A high, time-varying flux at 6.4 keV was indeed observed in the GMC Sgr B2 by Koyama et al 1996, and has been extensively studied ever since (Murakami et al., 2000; Muno et al., 2007; Inui et al., 2009; Ponti et al., 2010; Terrier et al., 2010; Capelli et al., 2012; Nobukawa et al., 2011; Gando Ryu et al., 2012; Clavel et al., 2013; Ponti et al., 2013; Zhang et al., 2015). Scattered flux from Sgr B2 in hard X-rays has also been detected using Integral (Revnivtsev et al., 2004). Similarly, other GMCs in the CMZ (Murakami et al., 2001; Marin et al., 2015) have since been shown to act as XRNe. An alternative scenario to the reflection of past Sgr A* flares, which explains the 6.4 keV emission in Sgr B2 as the result of the interaction of low-energy cosmic ray electrons with matter in the GMCs, has also been proposed (Valinia et al., 2000; Yusef-Zadeh et al., 2002; Dogiel et al., 2009; Yusef-Zadeh, 2013). Both scenarios will equally be affected by the clumping of gas inside Sgr B2 discussed in this work. The two cases can however be differentiated by considering of the different energy deposition rates resulting from either X-ray or cosmic ray propagation, and by the speed of propagation of the Fe K-α front. In particular, the observation of a superluminal echo (Sunyaev & Churazov, 1998; Sunyaev et al., 1999a; Ponti et al., 2010) in the 6.4 keV brightness cannot be explained by any model of line excitation other than the one resulting from illumination by an external source. In addition, studies of the polarisation and spectral absorption edges in the X-ray continuum, both of which would be expected in the reflection scenario but not in the cosmic-ray one, can further help distinguish the two effects. NuSTAR-type hard X-Ray grazing incidence telescopes should be able to detect absorption edges for a few heavy elements, including Fe and Ni.

Both the continuum and fluorescent spectral features of the reflected X-ray spectrum are dependent on the structure and composition of the gas itself, as well as on the properties of the X-ray source illuminating the gas, and on the relative position of the source and the gas with respect to the observer. They therefore contain a wealth of information both on the source itself and on the gas structures surrounding it.

Several models (Sunyaev & Churazov, 1998; Murakami et al., 2000; Churazov et al., 2002; Odaka et al., 2011; Marin et al., 2014a,b; Marin, 2015; Marin et al., 2015) have been developed to simulate the reflection of Sgr A* flares by Sgr B2, the brightest of the CMZ XRNe. These models considered different relative positions of the GMC with respect to the source, different total masses of the GMC and different density gradients of its gas.
In this work, we wish to expand on these models to investigate how more realistic models of the substructure of molecular clouds, in particular their clumpiness, would affect the reflected X-ray signal. (From now on we refer to both clumps and cores as clumps for simplicity, as the latter term merely refers to the low-mass end of the same population of overdensities.)

We use a 3D grid-based Monte Carlo radiative transfer code to compute the reflected energy spectrum and polarisation of Sgr B2's X-ray emission. In Section 4.2 we discuss the physical processes accounted for and the Monte Carlo method used in our calculations. In Section 4.3, we discuss the models for Sgr B2 considered, including the parameters used and the assumptions made in simulating its clump population (Section 4.3.1). In Section 4.4 we discuss the results obtained.

Finally, in Section 4.5, we discuss the time-variability of the X-ray morphology of XRNe in the case of clumps. We suggest that, under illumination by a non-persistent, flaring source such as Sgr A*, the evolution of reflected X-ray intensity can reveal information about the location of the clumps along their line of sight, and therefore about the 3D distribution of these substructures inside GMCs.

Even though we simulate the particular case of Sgr B2, our results are more generally applicable to other GMCs in the Galaxy when illuminated by other X-ray sources such as X-ray binaries. Notice that in such cases, however, the polarisation of the primary radiation due to scattering onto the corona and accretion disk, as well as due to relativistic effects, would need to be carefully taken into account (Meszaros et al., 1988; Haardt & Matt, 1993; Poutanen & Vilhu, 1993; Taverna et al., 2014). Assumptions on the polarisation state of Sgr A* flares assumed in our calculations are discussed in Section 4.4.

4.2 Monte Carlo simulation of X-ray propagation in inhomogeneous media

In this Section, we describe the physical processes accounted for to simulate the propagation of X-ray photons in neutral gas (Section 4.2.1) and the the Monte Carlo radiative transfer code used (Section 4.2.2).

4.2.1 X-ray interaction with neutral matter

X-rays interaction with atoms and molecules in the interstellar gas takes place through two processes: scattering and absorption through photoionisation.
Scattering processes of X-ray photons on bound electrons are classified as Rayleigh in the

case of elastic scattering, Raman for scattering that results in the excitation of electrons in the atom or molecule, and Compton for scattering that results in the ionisation of the atom (Sunyaev & Churazov, 1996). In our code, we account for these scattering processes on neutral HI, H2 and He using the results for the doubly differentiated cross section of Vainshtein et al. (1998). The contribution of heavier elements to the total scattering cross section, for which such results are not currently available, is accounted for by approximating the interaction of X-rays with their electrons as if they were unbound. We also include the effect of polarisation in Rayleigh and Compton scattering processes using the prescription of Namito et al. (1993). For simplicity, we ignore the polarisation dependence of Raman scattering, which can cause a depolarisation of the scattered radiation (Allemand, 1970; Szymanski, 1970). Raman scattering contributes less than 1% to photons observed after a single scattering for the geometry considered in this work (average angle $\sim 90°$), and will only contribute 10-15% in a narrow ($\sim 20°$) angular range in the scattering of secondary photons. This approximation therefore will not significantly affect our results, although it may affect the polarisation of the reflected spectrum under a different geometry.
Photoionisation, on the other hand, takes place through the ionisation by X-ray photons of tightly bound electrons in the atoms' innermost shells, which results in the release of a free electron. We use cross sections from Verner & Yakovlev (1995), and include both K- and L-shell photoabsorption. The unstable electron configuration of the ionised atom prompts the filling of the K-shell vacancy by an electron in one of the higher energy levels, which causes a release of energy. This energy can either be released through the emission of a photon in the X-ray range (fluorescence) or be transferred to another electron, which is then ejected from the atom (Auger effect). The probability of either process taking place varies depending on the atomic configuration and on the original energy level of the electron that fills the K-shell vacancy. The probability of fluorescence is called the radiative yield (Y). In our calculation, K-shell fluorescence yields are taken from Krause et al 1979, and K-$_\beta$-to-K-$_\alpha$ ratios are taken from Ertugral et al 2007. K-$_{\alpha 2}$-to-K-$_{\alpha 1}$ ratios are decided by the degeneracy of $2_{p_{1/2}}$ and $2_{p_{3/2}}$ levels, which we fix to 0.5. The energies of the fluorescent lines are taken from Thompson et al 2001.
We assume a chemical composition of the Sgr B2 cloud given by a factor of 1.5 compared to protosolar abundance, as estimated by Lodders (2003).

4.2.2 Photon weighing method

We use a Monte Carlo grid-based radiative transfer code to simulate the propagation of X-ray photons through a cloud of complex internal structure, containing both diffuse and dense regions. We use an octree-based approach (Meagher, 1980) to grid the cloud's internal structure, which allows us to have finer grids in high density regions.
The Monte Carlo code makes use of the Pozdnyakov et al. (1983) prescription for Monte Carlo methods of X-ray propagation. This applies a weight-based approach to the radiative transfer, in which photon packages, rather than individual photons, are followed. Each package is described by a statistical weight w, which reflects the relative probability of photons undergoing different types of interactions, a position, $\mathbf{r}$, a direction of travel, $\mathbf{\Omega}$,

and an energy, hv.
Photon-packages are initially emitted by the source with weight 1. Their starting position is the source's own position, and their energy is randomly sampled from the source's spectrum. Finally, their initial direction is randomly sampled from an isotropic distribution (assuming the source radiates isotropically).
To compute the propagation of photon packages in our grid, we estimate the relative probability of different processes occurring at each step. A photon package $\mathbf{P}$, found in a given grid-cell g, has, in fact, a probability of:

- escaping the grid-cell g, (L);
- not escaping the grid-cell g, $(1 - L)$;

and, if not escaping the grid-cell g, a probability of:

- being scattered, $(p_{scatt,Z})$;
- being absorbed by a K or an L shell, $(p_{abs,Z} = p_{Kion,Z} + p_{Lion,Z})$;

By considering photon packages rather than single photons, we are able to account for all the above events at once by splitting the initial photon package weight w as follows:

- $w_u = wL$ is the probability of $\mathbf{P}$ crossing the grid-cell without undergoing any interaction;
- $w_s = w(1 - L)p_{scatt,Z}$ is the probability of $\mathbf{P}$ undergoing a scattering event inside the grid-cell;
- $w_{fluo,Z} = w(1-L)p_{Kion,Z}Y$ is the probability of $\mathbf{P}$ photoionising the K shell of element Z,resulting in a fluorescent emission;

We can account for these events by assigning their weight to secondary packages $\mathbf{P_u}$,$\mathbf{P_s}$, and $\mathbf{P_{f,Z}}$s, which will represent the relative probability of each one of those physical events taking place. Parameters $\mathbf{r}$, $\mathbf{\Omega}$ and hv in $\mathbf{P_u}$,$\mathbf{P_s}$, and $\mathbf{P_{f,Z}}$s of course have to be updated, each according to the physical processes that are relevant for that secondary package.
Once all the parameters have been updated, the calculation is iterated by taking each one of the secondary packages as an initial package $\mathbf{P}$, and so on, for the secondary packages that are then produced. To limit the number of secondary photon packages that the code has to follow, we define a statistical threshold ϵ, below which secondary packages are discarded.
We note that other possible events, for example the emission of an Auger electron, which is not listed above, as well as any secondary processes they may cause, will not result in the emission of X-ray radiation, and can therefore be safely ignored in the processing of the X-ray radiation field. They will however contribute to the deposition of X-ray energy to the interstellar gas. The convergence of the code with respect to the threshold ϵ and other parameters was verified, as well as the consistency of our results with those of Odaka et al. (2011) (for the energy spectrum) and Churazov et al. (2002) (for the polarisation spectrum).

4.3 Sgr B2 model

Sgr B2 is not only one of the most massive, but also one of the most complex molecular structures observed in our Galaxy, containing ∼10% of the molecular mass in the CMZ (Gordon et al., 1993). It is also one of the brightest XRNe observed, making it an ideal target for our study.

Located at a projected distance from the GC of ∼ 100 pc, its exact position on the line of sight still remains uncertain. In a coordinate system in which the GC is located at (0,0,0), the observer at the Sun's location (0,-8kpc, 0), and the Galactic longitude is defined in the direction of the positive y axis, we assume a fixed position of the GMC at (0,100 pc,0), so that the angle between the source, the cloud and the observer is $\sim 90^{\circ}$. Discussions on how different geometries affect the reflected X-ray signal can be found in Churazov et al. (2002), Odaka et al. (2011) and Marin et al. (2014a).

Studies of the large scale morphology of Sgr B2 (Lis & Goldsmith, 1990) show it is surrounded by a diffuse gas envelope, extending up to 22.5 pc in radius, with a near-uniform density of $n_{H2} \sim 10^3 \mathrm{cm}^{-3}$. What is generally referred to as the Sgr B2 cloud, and where most of the reflected X-ray signal originates, is a dense region within this envelope, of density $n_{H2} \sim 10^{4-5} \mathrm{cm}^{-3}$ and extending out to a radius of 10 pc (Hasegawa et al., 1994). Within this region, multiple dense clumps can be observed. The Sgr B2 GMC contains three well-known dense clumps, named B2(N), Sgr B2(M) and Sgr B2(S). These are known to host clusters of compact HII regions, which provide evidence for star-formation activity within this GMC (Gordon et al., 1993). Two of these cores, SgrB2(N) and SgrB2(M) (with masses of $3313 M_{\odot}$ and 3532 $M_{\odot}$ (Qin et al., 2011) and radii 0.47 pc and 0.62 pc (Etxaluze et al., 2013) respectively), have been resolved at a subarcmin scale in X-rays (Zhang et al., 2015) and at a subarcsec scale using the Submillimeter Array (SMA) by Qin et al. (2011). The high angular resolution reached by the latter study reveals a remarkable difference in the internal structure of the two cores, with SgrB2(M) appearing to be highly fragmented into 12 sub-cores and SgrB2(N) appearing to be divided into only two sub-cores, one of which contains most of the mass. The very different morphologies of the two have been speculated as evidence in support of the idea that the two cores may represent different evolutionary stages of basically the same core, given that SgrB2(N) and SgrB2(M) are of comparable size and mass.

In our calculations, we assume Sgr B2 to have a mass of $M_{B2} = 2.5 \times 10^6 M_{\odot}$ within radius 10 pc, and a diffuse H2 envelope around it as described above. In our calculations, we approximate this envelope following Odaka et al. (2011)'s prescription, by considering an initial absorption to the incoming spectrum owing to a column density of $N_{H2} = 6 \times 10^{22}$ cm^{-2}. We note that this initial absorption will only affect the incoming spectrum below ~ 4 keV energies.

Given this mass and size, we then consider different possible models for the clump population inside the cloud, as discussed in the next section. The gas is assumed to be cold and neutral.

In our model, the optical depth of the gas located between Sgr A* and Sgr B2 is assumed to be negligible. This is a clear simplification of the gas distribution in the Galactic centre

region, and there is indeed a possibility that part of other important molecular structures located in the vicinity of Sgr B2, such as the Bridge, the MC 2, or the G0.11-0.11 cloud, could intervene between the two (Capelli et al., 2012; Clavel et al., 2013; Ponti et al., 2010, 2014). If the optical depth of the intervening gas were significant, it would obviously contribute towards the absorption and scattering of the incoming radiation. This would modify the radiation reaching Sgr B2, whose illumination would then become dependent on the morphology of the intervening gas. In particular, different parts of Sgr B2 would, in this case, be illuminated by X-rays described by different spectral energy distributions. We however do not consider such complications in the present work.

4.3.1 Simulating Sgr B2's clump population

Since the outset of this field, statistical descriptions of the internal structure of GMCs have been formulated in terms of discrete over-dense regions within GMCs (i.e. clumps and cores). More recently, a growing number of studies have adopted a different approach and described these density fields in terms of fractals, placing emphasis on the self-similarity of structural features at all scales (see Williams, 1999). In our work we will use the former approach.

The statistical study of these discrete over-dense regions has been applied to a number of nearby Galactic plane GMCs, such as Orion and W51 (eg. Parsons et al., 2012). This has led to the formulation of standard population properties and relations, which have been generalised from studies of Galactic molecular clouds (eg. Larson, 1981): the clump mass function (CMF) and mass-size relation of individual clumps. These studies, along with simulations, suggest that similarities exist both in the CMF and mass-size relations between different GMCs, and therefore point towards a universal structure of GMCs in the Galactic plane. The internal structure of GMCs in the CMZ, on the other hand, is likely to differ greatly from that observed in Galactic plane GMCs, because of the extreme environment, both in density (Lis & Goldsmith, 1990) and pressure (Kruijssen et al., 2014). Understanding how the clump population of these objects differs from the ones found in Galactic plane GMCs, would, therefore, provide an important insight into how environmental factors affect the process of internal structure formation.

As previously discussed, the studies of GMCs in the CMZ are rather more difficult to perform, on account of the large distance and mass of these complexes: catalogues of clump and core populations in these GMCs are known to be incomplete, and therefore don't allow for a reliable estimate of their statistical properties.

In our calculations, we consider the different possible shapes of the CMF and mass-size relation. We also consider the different levels of fragmentation of the cloud into clumps by considering different possible values of the dense gas-mass fraction, or the fraction of the cloud's mass found in clumps, $f_{\rm DGMF}$ (see Fig. 4.1). In particular, we investigate the effects of the following clump population model parameters on the XRNe's X-ray emission:

- Slope of the clump mass function (α);
- Minimum clump mass in the clump mass function (m_{min});

- Fraction of the total cloud's mass found in clumps, or dense gas mass fraction ($f_{\rm DGMF}$);
- The mass-size relation of individual clumps ($m = m_{norm}(r/pc)^{\gamma}$);

The simulation of different clump population models for Sgr B2 is then performed as follows: given a $f_{\rm DGMF}$ and CMF, we sample the clumps' masses from the CMF in the mass range $m_{min} - m_{max}$, with $m_{max} = 10^4$ M$_\odot$, until we obtain a total mass of $M_{DGMF} \sim f_{\rm DGMF} \times M_{B2}$. We then proceed to assign each clump with a size that is based on its mass assuming a mass-size relation. Finally, we uniformly distribute the resulting clumps inside the cloud and calculate the interclump density using the 'left-over' mass, $M_{interclump} \sim (1 - f_{\rm DGMF}) \times M_{B2}$ and the 'empty' (i.e. not occupied by clumps) volume, assuming the interclump density is homogeneously distributed.
In the following sections, we discuss the details of this procedure, together with the range of parameters that we considered and the assumptions made in doing so.

Clump mass function

The clump mass function (CMF) of clump populations, which can be observed in Galactic plane GMCs, takes the following form (McKee & Ostriker, 2007):

$$m\frac{{\rm d}N}{{\rm d}m} \propto m^{-\alpha} \tag{4.1}$$

The slope of the clump mass function is similar to that for GMCs as a whole, possibly because both are determined by turbulent processes within larger, gravitationally bound systems (McKee & Ostriker, 2007). The parameter α takes different values in different mass ranges. The low mass end of the function is known as the core mass function. Its shape is particularly important in relation to the initial mass function (IMF) of stellar populations (McKee & Ostriker, 2007). Evidence of similarity in the core mass function with the IMF were first studied by Nutter & Ward-Thompson (2007) in the Orion complex, which for the first time observed a turnover at $\sim 1.3M_\odot$, which mimics the turnover seen in the stellar IMF at 0.1 $M_\odot$. Fitting the data with a three-part power law function similar to that observed in the stellar IMF, they obtain the following parameters:

$$\alpha = \begin{cases} -0.3 & \text{if } 0.4M_\odot < m < 1.3M_\odot \\ 0.3 & \text{if } 1.3M_\odot \leq m \leq 2.4M_\odot \\ 1.35 & \text{if } m > 2.4M_\odot \end{cases} \tag{4.2}$$

for clump mass ranges below $100M_\odot$. The physical significance of the turnover mass is not clear, since the same work highlights that similar studies in the lower-mass and nearer cloud complex ρ Ophiuchi showed no turnover in their CMF (Motte et al., 1998). Later studies on the low-mass end of the CMF in the Aquila rift cloud complex also confirmed a variation in this parameter: Könyves et al. (2010) found a turnover mass of $\sim 0.6M_\odot$ in the starless core sample, and $\sim 0.9M_\odot$ prestellar (starless and gravitationally bound)

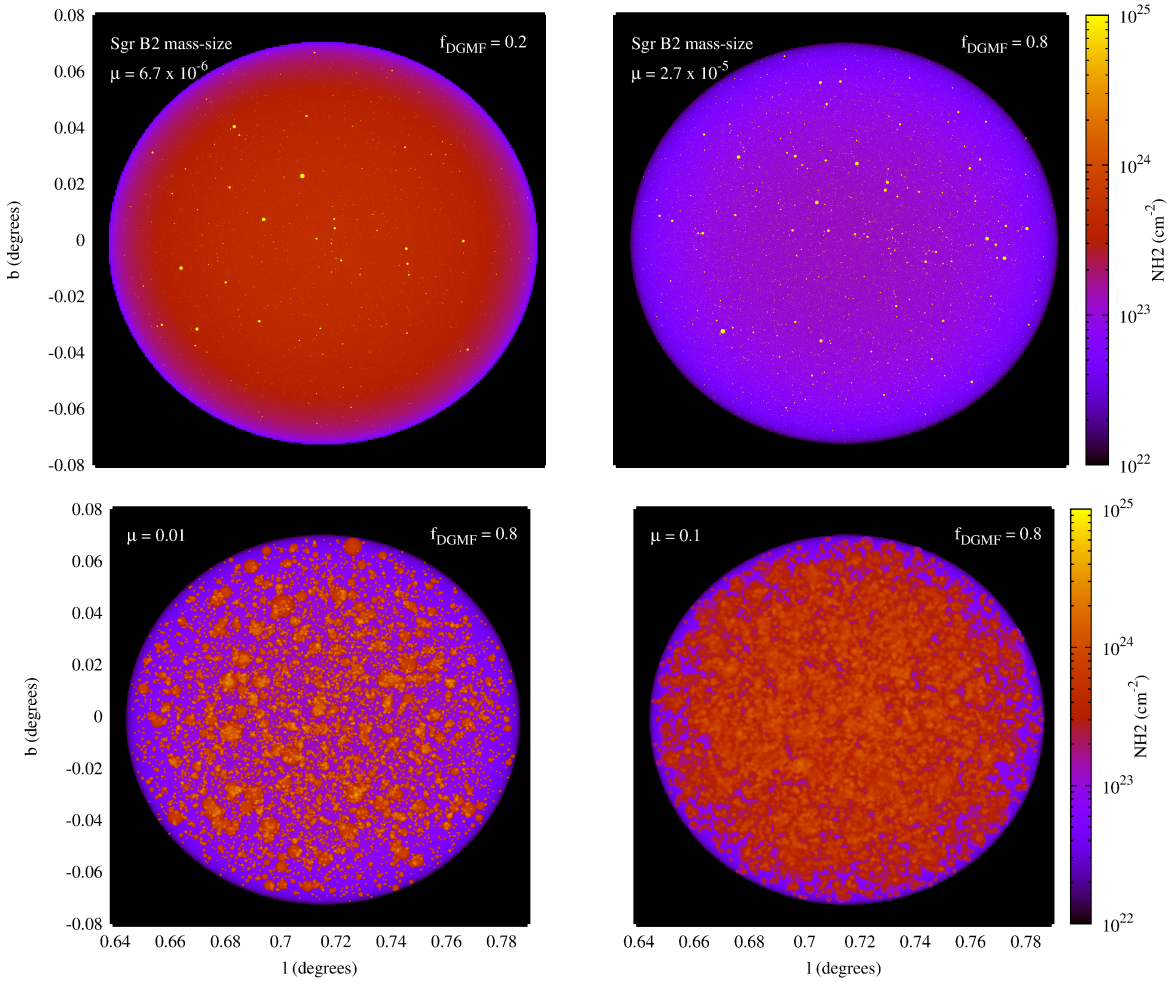

Figure 4.1: Cumulative column density ($N_{\rm H2}$) along line of sights, excluding ISM and diffuse envelope contributions. The maps show Sgr B2 models with fixed parameters $\alpha = 1.35$, $m_{min} = 10 M_{\odot}$ and Sgr B2 mass-size relation, and two values of $f_{\rm DGMF}$. The concentration of mass into small dense regions reduces the interclump density, as seen from the figures. In the case of $f_{\rm DGMF} = 0.8$, we also show clump populations with mass-size relations tuned to obtain a volume-filling fraction of $\mu = 0.01$ and $\mu = 0.1$. At a distance to the centre of Sgr B2 of ~ 8000 pc, 1 arcmin corresponds to a size of ~ 2.3 pc.

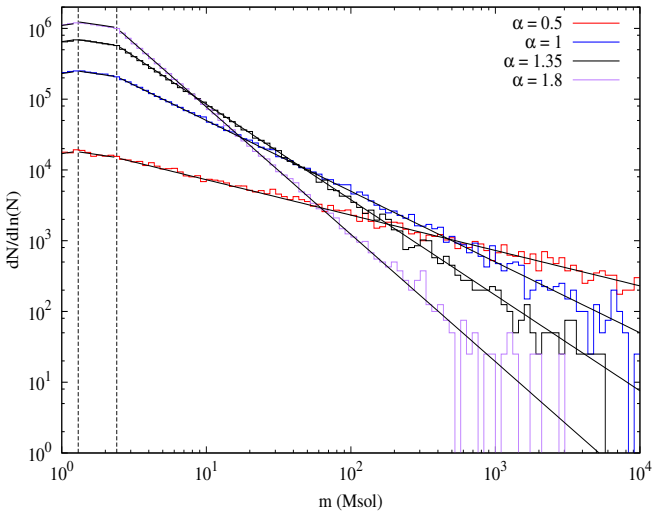

Figure 4.2: Clump mass functions for different α with $f_{\rm DGMF} = 0.4$. The grey solid lines show the distributions sampled, while the coloured lines show the actual realisation. The vertical lines show the values at which the CMF changes in slope. As the slope of the function steepens, more clumps are selected from the lower-mass range. This leads to a progressive increase in the numerical noise in the sampled population at higher masses with increasing α, as seen in the plot.

sub-sample.
The similarity of the CMF with the Salpeter (1955) stellar IMF has been further confirmed in higher mass ranges by Tsuboi & Miyazaki (2012) (range $> 900\ M_{\odot}$) and Parsons et al. (2012) (range $> 200\ M_{\odot}$).
Despite the fact that the CMF appears to be consistent throughout Galactic plane GMCs, the extreme environment of Sgr B2, as previously discussed, suggests the CMF for this GMC could be significantly different. Unfortunately, because of a lack of exhaustive data, how this function could differ is not obvious. We therefore adopt the Nutter & Ward-Thompson (2007) three-part power-law fitting, but consider different α values in the highest mass interval. In particular, we consider $\alpha = 1.35$ (i.e. Galactic plane value), $1, 0.5, 1.8$ (see Fig. 4.2). We sample this range up to clump masses $10^4 M_{\odot}$, to be consistent with the observed massive cores in Sgr B2 (eg. Qin et al., 2011). We maintain the low-mass threshold of the CMF as a parameter in the model, m_{min}, and investigate its effect on the reflected X-ray signal.

Clumps mass-size relation

The mass-size relation of individual clumps is particularly important for our study, as it determines the volume-filling fraction, μ, of the clump population given its α, m_{min} and $f_{\rm DGMF}$ parameters. The volume-filling fraction, in return determines how effectively clumps 'hide' part of the cloud's mass, by concentrating it into small volumes which X-rays have

a low probability of intercepting.
For clumps formed inside GMCs via turbulent fragmentation, we would expect to find a mass-density, or similarly a mass-size, relation (Donkov et al., 2011). A first suggestion of this relation based on observations was formulated in the seminal paper of Larson (1981), which claimed a universal power-law mass-size relationship should describe all clouds and clumps found in the Galaxy. This is commonly referred to as "Larson's third law", and it suggested that the relation should go as

$$m = m_{norm} r^{\gamma} \tag{4.3}$$

with $\gamma = 2$. Since being first formulated, this empirical observation has been extensively studied both in observations (eg. Kauffmann et al., 2010; Lombardi et al., 2010) and in simulations (Shetty et al., 2010; Donkov et al., 2011), which all find a deviation from the power of 2 originally found by Larson (1981). The latter two studies find that on scales < 1pc, the mass-size relation studied in 11 different GMC structures in the Galactic plane, can be described as $m(r) = 400 M_{\odot}(r/pc)^{1.7}$ and $m(r) = 380 M_{\odot}(r/pc)^{1.6}$ respectively. By looking at these clouds individually, Lombardi et al. (2010) find that these clouds have quite similar exponents, but rather different normalisation masses (ranging from 170 to 710 $M_{\odot}$).
Although these studies haven't been performed for the clump population of Sgr B2, we can use observational data that is currently available to get a rough estimate of what this relation would look like for this GMC.
We use the data available from the 14 cores within Sgr B2(N) and SgrB2(M) which are resolved in the subarsec observations of Qin et al. (2011) to infer a mass-size relation for Sgr B2. Assuming a homogeneous density distribution inside the clumps, we fit the power law to these observations and find:

$$m(r) = 4.68 \times 10^5 M_{\odot}(r/pc)^{1.77} \tag{4.4}$$

which we refer to henceforth as the "Sgr B2 mass-size relation". We find that the exponent is consistent with the results of Lombardi et al. (2010), but that the normalisation mass is considerably higher. This is somehow to be expected, considering that the average density in Sgr B2 is considerably higher than that found in Galactic plane GMCs. We note that the range of sizes of these cores is considerably below the Lombardi et al. (2010) range. Furthermore, the assumption of gas being homogeneously distributed inside the clumps is also a clear simplification, which could have an impact on our results (see Odaka et al. (2011) for considerations on the effect of density gradient on reflected X-ray emissions). In our model, we assume this relation, inferred in a somewhat limited mass range, holds for all possible clump masses.
As already mentioned, the mass-size relation is particularly important for our study as it effectively determines the volume-filling factor of a given population. The volume-filling factor, μ, can be expressed in terms of other clump population parameters as follows:

$$\mu = \frac{4\pi}{3V_{SgrB2}} \frac{C}{m_{norm}^{3/\gamma}} \frac{[m^{-\alpha+3/\gamma}]_{m_{min}}^{m_{max}}}{-\alpha + 3/\gamma} \tag{4.5}$$

where

$$C = \begin{cases} M_{DGMF}(1-\alpha)([m^{-\alpha+1}]_{m_{min}}^{m_{max}})^{-1} & \text{if } \alpha \neq 1 \\ M_{DGMF}[\ln m]_{m_{min}}^{m_{max}} & \text{if } \alpha = 1 \end{cases} \tag{4.6}$$

Using Eq. 4.5, and assuming the mass-size relation given in Eq. 4.4,we obtain a maximum filling fraction of only 10^{-4} (see Fig. 4.3) among all $f_{\rm DGMF}, \alpha$ and m_{min} values considered. Therefore the probability of X-rays intercepting the clumps is extremely low. Hence, we don't expect parameters related to the mass distribution of the clumps, i.e. α and m_{min}, to significantly affect the X-ray signal when assuming this mass-size relation. We also consider how the X-ray signal could be affected by increasingly large values of μ, by varying the m_{norm} value in the mass-size relation accordingly (see Section 4.4.2).
The mass-size relation can be alternatively expressed as a column density-mass relation to the centre of the cloud. Defining $\tau_{\rm H2} = r n_{\rm H2} \sigma$, this takes the following form:

$$\tau_{\rm H2} = m_{norm}^{2/\gamma} \frac{3\sigma}{m 4\pi} m^{-2/\gamma+1} \tag{4.7}$$

The effect of the mass-size relation on the clumps' contribution to the column density of the GMC is shown in Fig. 4.1.

Dense gas mass fraction

Studies of this parameter in Galactic GMCs, eg. in W51 (Battisti & Heyer, 2014; Ginsburg et al., 2015), show a variety of possible stages of fragmentation in different clouds, which reflects the different evolutionary stages GMCs can be found in. We therefore span a wide range of $f_{\rm DGMF}$ values: $f_{\rm DGMF} = 0.2, 0.4, 0.6$, and 0.8.

Spatial distribution of clumps

In our model we assume clumps are not overlapping and are isotropically distributed inside the cloud.
The latter assumption is a clear simplification of what is currently being observed in CMZ GMCs (eg. Chen & Ostriker, 2015). In the case of very low volume-filling factors, as in the case of clumps that follow the Sgr B2 mass-size relation, this assumption should have a negligible effect on the reflected signal. On the other hand, this may become relevant in the case of larger volume-filling factors. The percolation of the X-ray photons is dependent on the projected area filling on the plane perpendicular to the source-cloud direction, rather than on the volume-filling factor itself. The maximum possible projected area occupied by the clumps, in the case where no line of sight from the source intercepts more than one clump, is $\propto \pi \sum_{i=1}^{N} v_i^{2/3}$, where v_i is the volume of the single clump i, and N is the total number of clumps. The minimum possible project area on the other hand, in the case where all clumps are centred along a single line of sight, is $\propto \pi v(r_{max})^{2/3}$, where $v(r_{max})$ is the volume of the largest clump in the population. The actual value of the projected area occupied by the clumps will be somewhere between these two extremes, and will be determined by the distribution of the clumps inside the cloud. We defer an investigation of

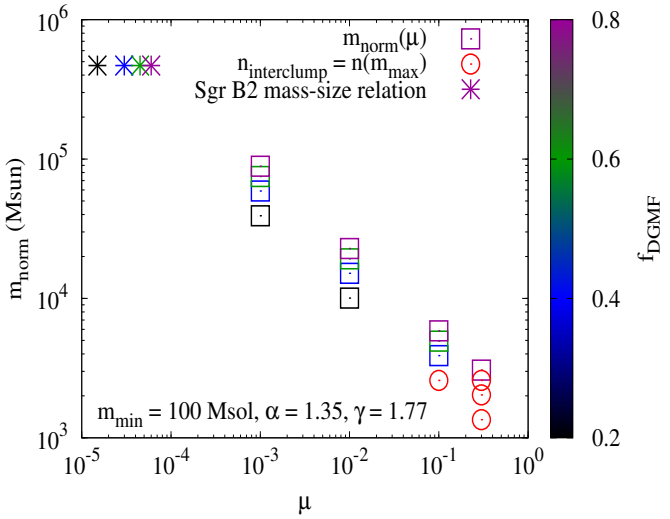

Figure 4.3: Normalisation parameter m_{norm} in the mass-size relation as a function of the volume-filling factor μ, calculated using Eq. 4.5, for different $f_{\rm DGMF}$ at fixed $\alpha = 1.35$, $m_{min} = 100 M_{\odot}$ and $\gamma = 1.77$. We also show the μ values, obtained using the fixed Sgr B2 relation. Note that for high μ and low $f_{\rm DGMF}$ values, we obtain mass-size relations yielding clump populations where the least dense clump, given by the clump with the highest mass (m_{max}), is less dense than the interclump density $n_{interclump}$, in contradiction with the very definition of a clump as an overdensity; we clearly indicated these models in red in the plot. We will use the $f_{\rm DGMF}$ value that allows us to explore a widest possible range of μ, $f_{\rm DGMF} = 0.8$, to investigate the impact of increasing μ on the reflected X-ray signal (see Fig. 4.8).

how the spatial distribution of discrete over-dense regions affects the reflected X-ray signal to a later study.

4.4 Results

We consider a persistent, unpolarised Sgr A* flare of luminosity 1.3×10^{39} erg/s (Revnivtsev et al., 2004), modelled with a power law photon index of 1.8 (Baganoff et al., 2001). The photon index assumed in this work allows for a direct comparison with the results of other works on the reflected Sgr B2 X-ray emission (Churazov et al., 2002; Odaka et al., 2011). While more recent works seem to support a somewhat steeper slope (2.5 ± 0.3) of the incoming spectrum (Porquet et al., 2003a, 2008; Nowak et al., 2012), features like the width of the shoulder relative to that of the line, which are important for morphological studies, are not very sensitive to the slope of the initial spectrum. The initial spectrum also wouldn't affect the variation of these features due to variation in the density structures, which are the main focus of this work. Finally, the inclusion of considerations of the polarisation fraction of the reflected emission can help break some of the degeneracy of

the reflected spectrum with the incoming one. We therefore believe the assumption of a 1.8 slope to be justified in this work. We note that, while we assume the source to be unpolarised for simplicity, there is a possibility that X-ray emission of Sgr A* could be partially polarised. In this work, however, we limit the scope of the parameters that we investigated to those of the molecular structure, and postpone the investigation of the effect of the source's initial level of polarisation to a later study.

For each model considered, we plot the energy spectrum and polarisation fraction of the reflected X-ray emission. The polarisation fraction is calculated as the fraction of the Stokes Q parameter (with the frame of reference chosen so that U=0) intensity over the total intensity reaching the observer.
First, we consider the case where the mass-size relation of the clumps is the Sgr B2 relation discussed in Section 4.3.1. We then consider, for fixed $f_{\rm DGMF}, \alpha$ and m_{min} parameters, the effect of varying the normalisation of the mass-size relation, and therefore the volume-filling factor of the clump population, on the reflected signal.

4.4.1 Fixed Sgr B2 mass-size relation

We consider a fiducial model given by $f_{\rm DGMF} = 0.4, m_{min} = 10 M_\odot, \alpha = 1.35$, and vary each parameter individually around it while maintaining the mass-size relationship constant at $m_{norm} = 4.68 \times 10^5 M_\odot$ and $\gamma = 1.77$ according to Eq. 4.4.

In Fig. 4.4, we compare the reflected X-ray emission for different values of the fragmentation parameter $f_{\rm DGMF}$. For all models considered, we observe that an increase in the fragmentation level of the cloud into clumps results in: a slight increase in the flux of low energy photons, a decrease in the flux of higher energy photons, and a decrease in the Fe shoulder's flux (see Figs. 4.5 and 4.6).

These three effects can all be accounted for by considering percolation: because the probability of intercepting the clumps is extremely low, owing to the small ($< 10^{-4}$) volume-filling fraction of the clumps, the X-ray photons will mainly interact with the atoms and molecules in the interclump medium. The resulting reflected spectra will therefore be consistent with those resulting from reflection off homogeneous clouds with the same size, and density equal to the interclump density. In Fig. 4.7 we compare the X-ray emission obtained from cloud models where a fraction $f_{\rm DGMF}$ of the total cloud's mass is found in clumps and homogeneous cloud models with a total mass of $M_{B2} \times (1 - f_{\rm DGMF})$. We find indeed that the fractional difference between the two cases is negligible for all energies, and that the $f_{\rm DGMF} = 0.2, 0.4, 0.6$ and 0.8 models can be approximated by homogeneous clouds with $\tau_{\rm HI} \sim 0.32, 0.24, 0.16$ and 0.08 respectively (where $\tau = R \times n_{\rm HI} \times \sigma_{Thoms}$).

The decrease in the number of scatterings that resulted from an increase in the dense gas mass fraction can also be observed in the plots of the polarisation fraction of the reflected spectra (Fig. 4.4). An analytic approximation to the polarisation fraction of an

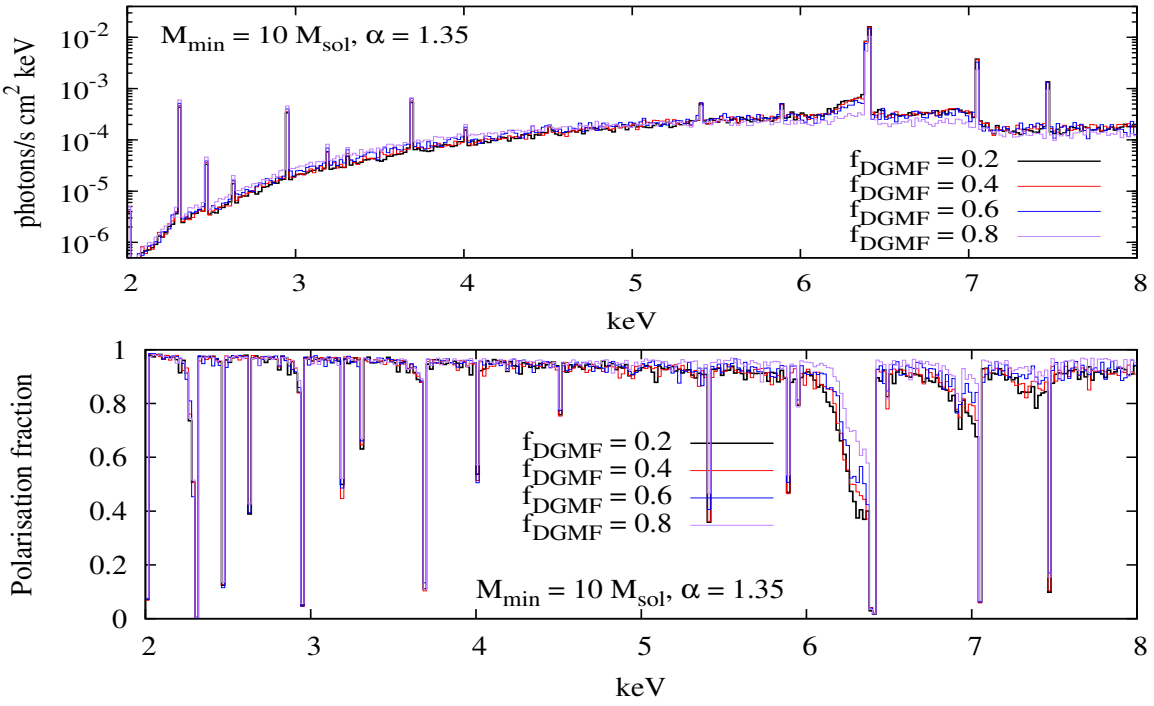

Figure 4.4: Reflected energy spectrum and polarisation fraction for varying f_{DGMF} cloud models. The energy spectrum is shown with a resolution of 20 eV.

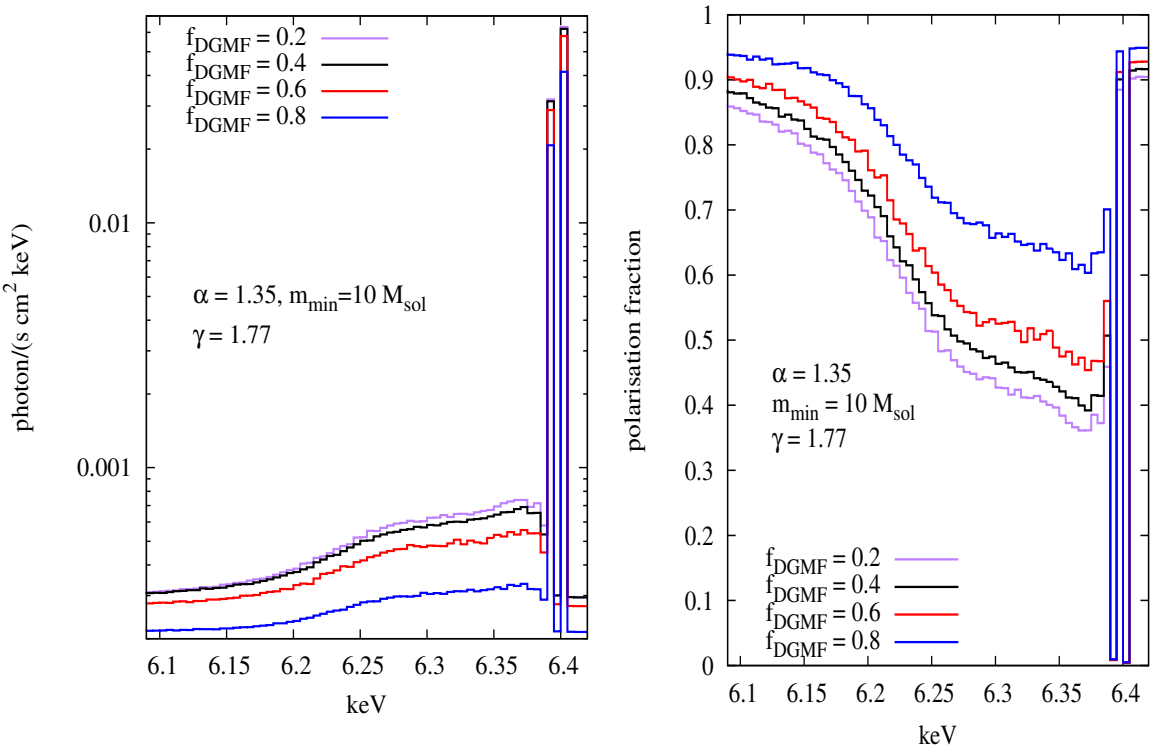

Figure 4.5: Reflected energy spectrum and polarisation around the 6.4 keV Fe K-α line for varying f_{DGMF}. The spectral resolution is 5 eV.

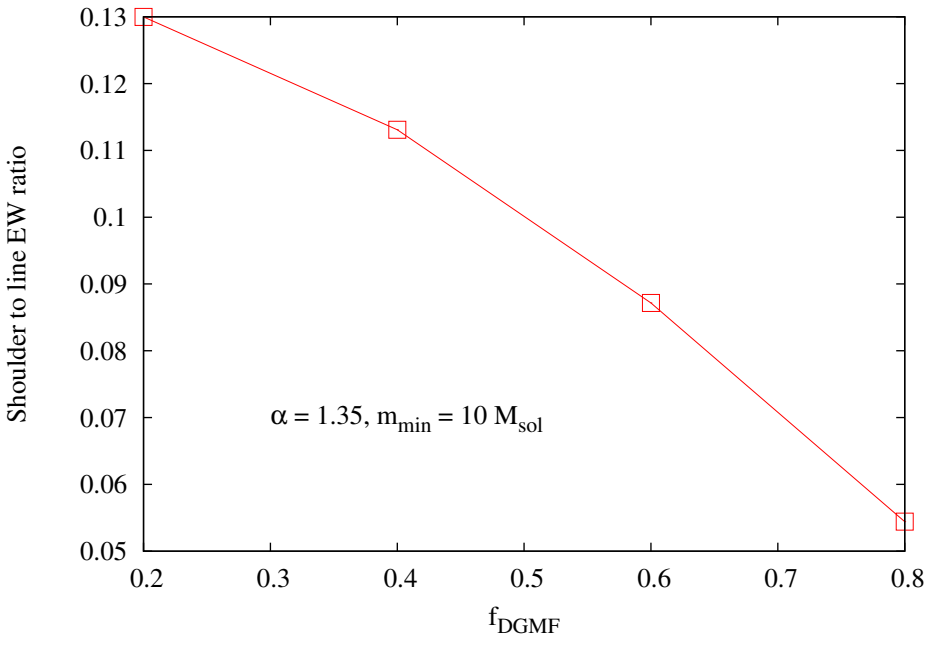

Figure 4.6: Ratio of the Fe K-α shoulder's EW to line's EW for varying f_{DGMF}.

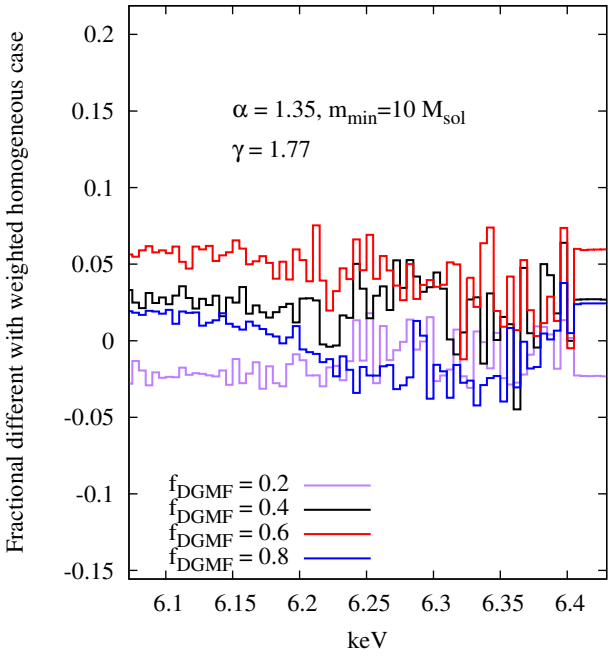

Figure 4.7: Fractional difference between the reflected energy spectrum for a cloud model with mass M_{B2} and a fraction $f_{\rm DGMF}$ of its mass found in clumps and a homogeneous cloud model with total mass $M_{B2} \times (1 - f_{\rm DGMF})$. The fractional difference is negligible for all energies, reinforcing the idea that the clumping of part of the cloud's mass into very dense region effectively "hides" that mass from the incoming X-rays.

X-ray photon that is undergoing n scatterings is given by (Churazov et al., 2002):

$$P_n = \frac{1-\eta^2}{1+\eta^2+\frac{20}{15}\left(\left(\frac{10}{7}\right)^{n-1}-1\right)} \tag{4.8}$$

where $\eta = cos(\theta)$ and θ is the average scattering angle. From this analytic prescription, it is indeed for the geometry considered in these calculations, the polarisation fraction should be close to unity for singly scattered photons, in the case of scattering close to $90°$ as is the case here, as and should progressively decrease from unity as the number of scatterings increases. With increasing energy the absorption optical depth decreases and the relative contribution to the radiation escaping from the cloud from multiple scatterings increases. This is evident in Fig. 4.4 as a decrease in the degree of polarisation of the spectrum with increasing energy.

In Fig. 4.4, we can clearly see that the polarisation fraction of the shoulder progressively increases with the dense gas mass fraction. This means that the higher the fraction of the cloud's gas found in dense regions, the lower the number of multiple scatterings that photons experience, which is in agreement with a picture of an increasing rate of percolation. Fluorescent photons, on the other hand, are emitted isotropically by photoionised atoms, and therefore are completely unpolarised. For varying α and m_{min} parameters we find that, on the other hand, these have no effect on the overall reflected signal. This reinforces the idea that the dominant effect of clumping within the XRN (in the case of the Sgr B2 mass-size relation) is percolation, and that the mass concentrated in clumps is effectively "hidden" from incoming X-ray photons because of the small volume it occupies.

4.4.2 Variable mass-size relation

Of course the picture painted in Section 4.4.1 of course only holds if the volume-filling fraction of the clump population is low enough to effectively reduce the probability of interaction between photons and overdensities to a negligible value. Should the volume-filling fraction increase, as would result from a variation in the mass-size relation of the clumps (see Section 4.3.1), then X-rays should start intercepting the clumps at a more significant rate, with consequences to the reflected energy and polarisation spectrum.
In particular, an increase in the absorption probability should result in an increase in the fluorescent lines, while an increase in the scattering probability should result in an increase in the fraction of fluorescent photons scattered, and therefore of the flux of the fluorescent line's shoulder. In Fig. 4.8, we show the energy and polarisation spectrum around the 6.4 keV K-α line for cases of increasing high volume-filling factor. We find that, as expected, both the line and the shoulder's flux increase with increasing μ.
Once the probability of intercepting clumps increases, we expect properties of the clump populations such as m_{min} and α to play a more significant role in shaping the reflected X-ray signal. In Fig. 4.9, we compare the reflected signal in the case of varying α and m_{min} parameters, respectively, for fixed $\mu = 0.01$. Indeed, for this volume-filling fraction we already observe that the slope shows a dependence on the two population parameters:

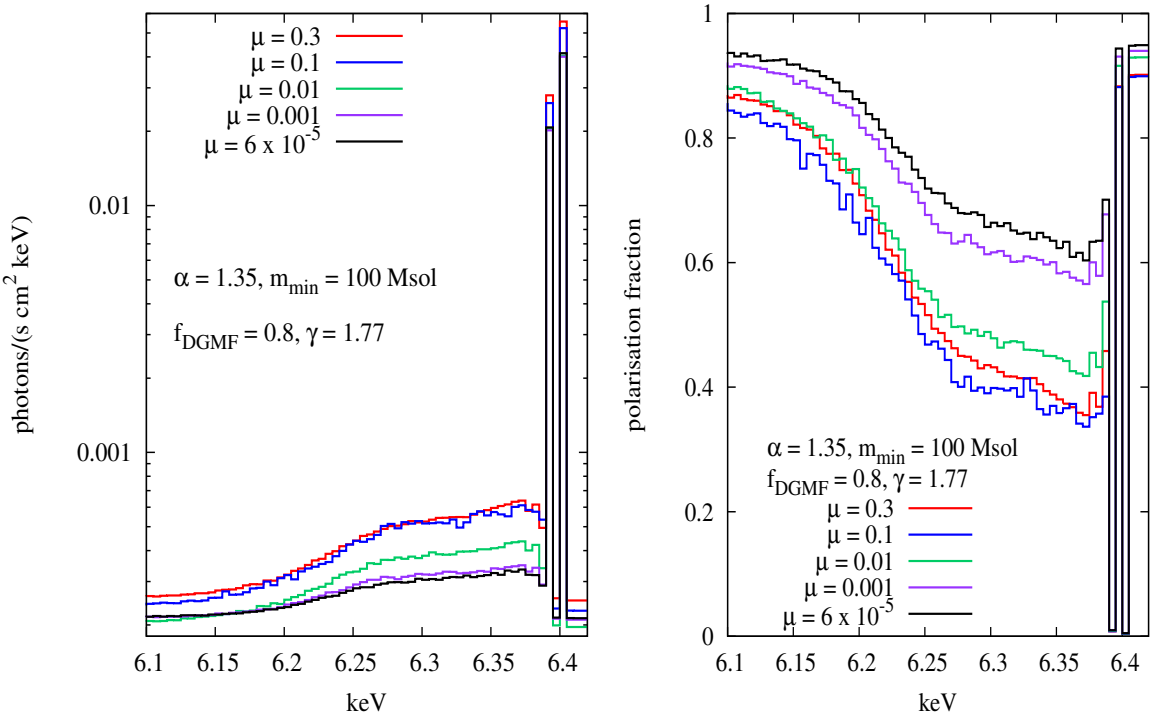

Figure 4.8: Reflected energy *(left plot)* and polarisation *(right plot)* around the 6.4 keV Fe K-α line for varying μ, shown with a resolution of 5 eV. The values of μ illustrated were obtained by adjusting the m_{norm} parameter in the mass-relation of clumps using Eq. 4.5. As expected, for increasingly large volume-filling factors, the probability of fluorescent photons intercepting the clumps increases, resulting in an increase in the shoulder's flux. Note that, because the X-ray signal is really dependent on the projected area (see Section 4.3.1), which roughly goes as $\mu^{2/3}$, we would expect a volume-filling factor of $\mu \sim 0.001$ (project area ~ 0.01) to already produce a visible signature in the X-ray spectrum. Indeed, from the polarisation fraction plot, it is clear that at $\mu = 0.001$ the signal starts deviating from the virtually homogeneous case.

a higher CMF slope results in a higher number of clumps with larger masses (and hence radii) being selected. Because these are more likely to intercept the incident X-rays, we expect an increase in the Fe shoulder's flux in correspondence with increasing α, as it is indeed observed in the figure. A decrease in m_{min} puts more mass in smaller clumps, resulting in a decrease in the fluorescent lines and shoulders in Fig. 4.9. However, a photon which is emitted inside a denser clump is also more likely to be scattered before it escapes, and therefore the ratio of the shoulder to line increases with decreasing m_{min}, as seen in the equivalent width (EW) ratio plot in the same figure.

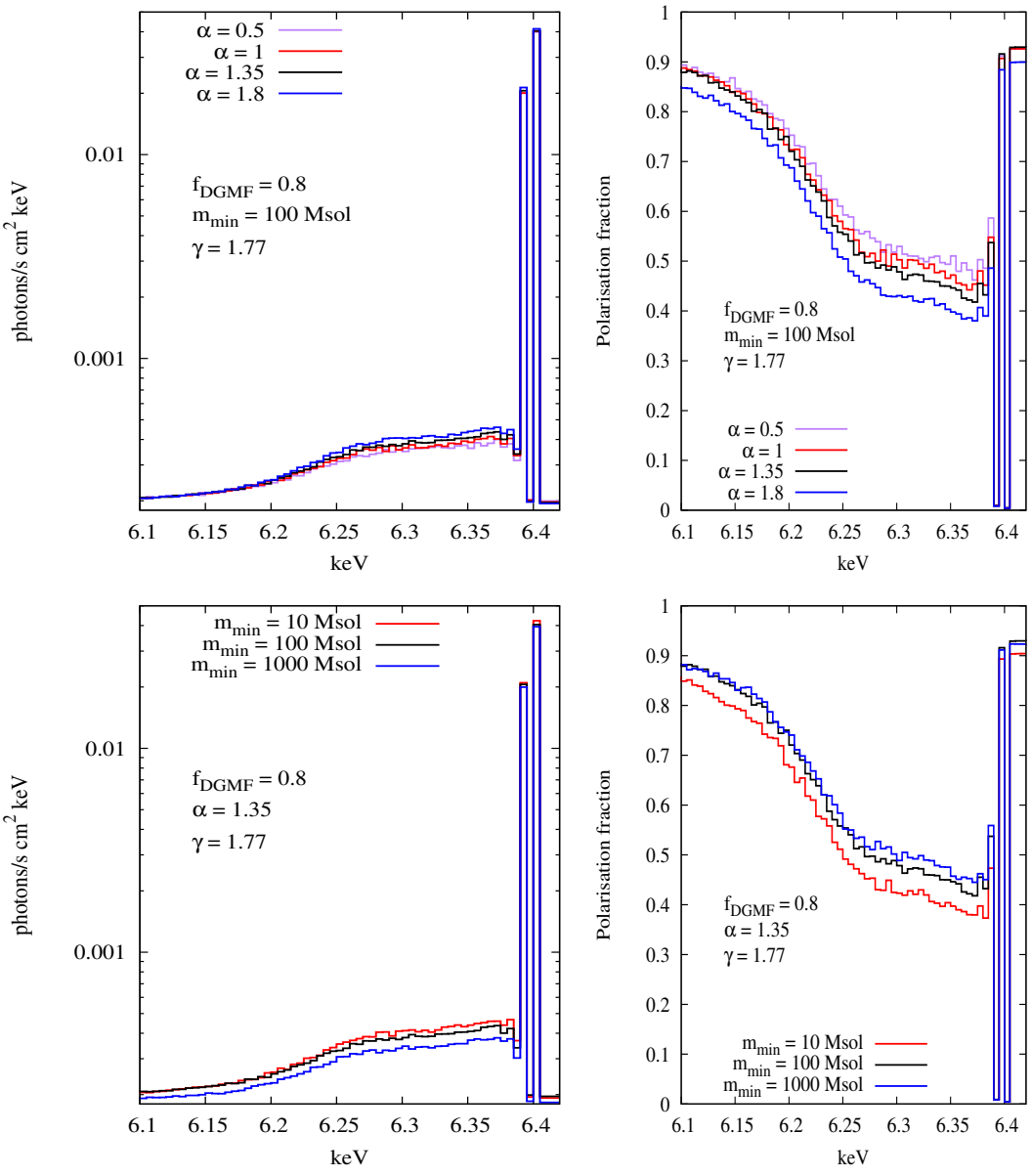

Figure 4.9: Reflected energy *(left plots)* and polarisation *(right plots)* around the 6.4 keV Fe K-α line (shown with resolution of 5 eV) for varying α *(top plots)* and m_{min} *(bottom plots)* parameters at fixed $\mu = 0.01$. Values of μ illustrated were obtained by adjusting the m_{norm} parameter in the mass-relation of clumps using Eq. 4.5. For increasing α, we expect an increase in the number of clumps being sampled from the higher mass range, resulting in a greater average size of the clumps in the population. In return, this results in an increase in the probability of X-rays intercepting them. Indeed, an increase in the Fe shoulder for increasing α is observed both in the energy and polarisation spectrum. The fragmentation of the clumps to lower and lower m_{min}, on the other hand, results in a larger projected area of the clump population, which increases the probability of interaction with incoming X-rays. This effect in also observed in the plots.

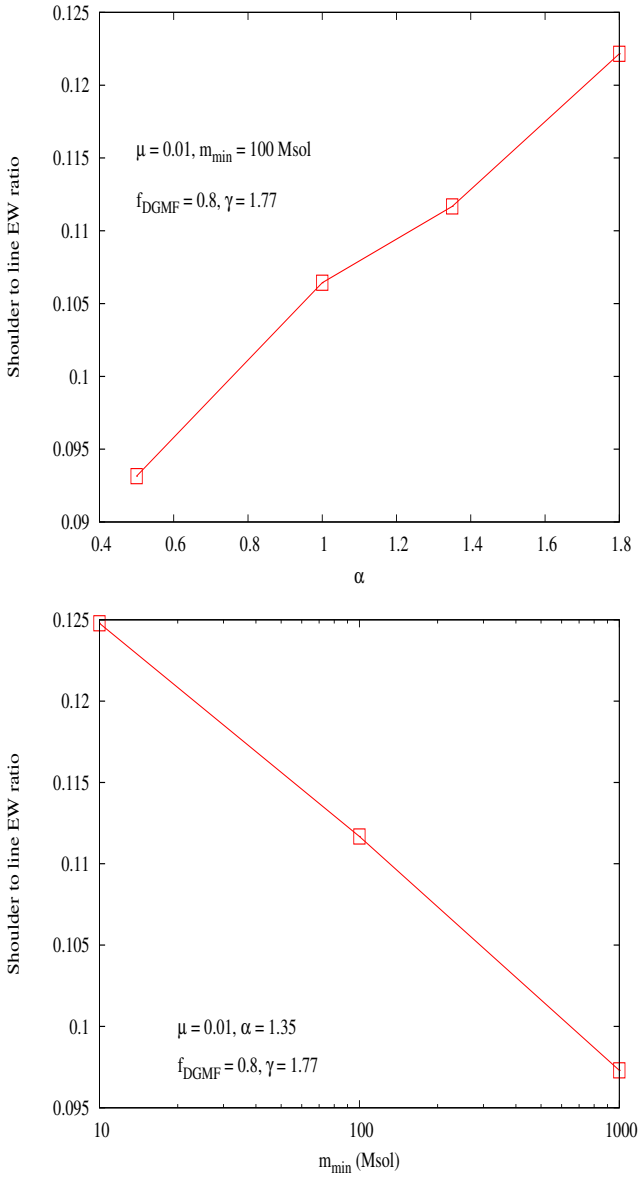

Figure 4.10: Ratio of the Fe K-α shoulder's EW to line's EW for varying α *(top plot)* and m_{min} *(bottom plot)* parameters at fixed $\mu = 0.01$.

4.5 Time-evolution of the XRN morphology as a probe of the 3D distribution of substructures

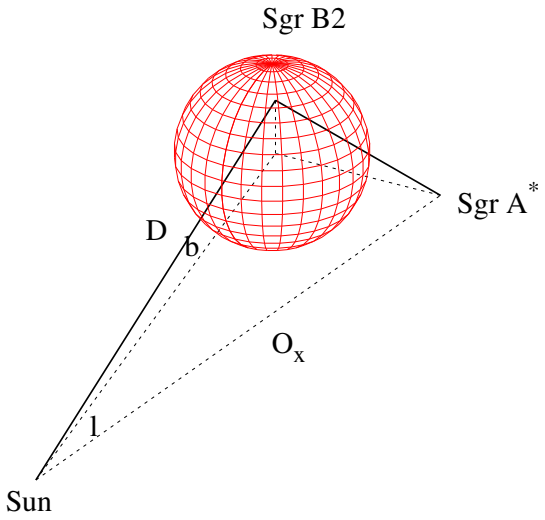

Figure 4.11: Schematic representation (not to scale) of parameters used in Eq. 4.9

As a result of the finite speed of light, the illumination by a flare of duration shorter than the light-crossing time of the cloud results in different regions of the GMC being visible to the observer, in the form of reflected X-ray emission, at different times. The evolution of the reflected X-ray intensity, therefore, acts as a scan of the density structure of the cloud as the wavefront propagates through it (Sunyaev & Churazov, 1998). In this section we discuss the importance of this effect in the context of the study of the GMC's clump properties and distribution.

For these calculations we focus on three of the Sgr B2 models that were considered in the previous sections:

- the fiducial model, which assumes parameters $f_{\rm DGMF} = 0.4$, $m_{min} = 10 M_{\odot}$, $\alpha = 1.35$ and the Sgr B2 mass-size relation that is consistent with observations of real Sgr B2 clumps (see Section 4.3.1), which corresponds to a volume-filling fraction of $\mu \sim 1.3 \times 10^{-5}$. We refer to this model as the Sgr B2 mass-size model;

- the homogeneous model, where we assume no clumps at all;

- a more 'visible' clump population model, which considers a case in which most of the gas ($f_{\rm DGMF} = 0.8$) is contained in relatively massive ($m_{min} = 100 M_{\odot}$) clumps, which are described by a mass-size relation that is constrained to obtain a volume-filling fraction as large as $\mu = 0.01$ (see Section 4.3.1). This case ensures clumps will be

numerous and voluminous enough to be easily recognisable in our calculations. We refer to this model as the "$\mu = 0.01$" model;

While these calculations were being performed, NuSTAR was able to resolve the Sgr B2 clumps Sgr B2(N) and Sgr B2(M) in X-rays for the first time (Zhang et al., 2015). This new result shows the feasibility and potential that high-resolution studies of the X-ray morphology of GMCs in the CMZ have in the study of the internal structure of these XRNe. We emphasise, however, that the mass-size relation assumed in our Sgr B2 mass-size model makes use of the Qin et al. (2011) observations of the clumps, which were able to resolve the Sgr B2(N) and Sgr B2(M) clumps into distinct and independent substructures. The clumps for this model that we obtained in our simulation are therefore more compact than the region of gas considered by the Zhang et al. (2015) observations.

In a single scattering approximation, the distance D along the line of sight (l, b) at which light has to be scattered to reach the observer at time t, defined such that $t = 0$ is the time at which the flare was last observed directly, is given by

$$D(t, t') = \frac{ct^2 - O_x^2 + 2ct(|O_x| - t'c) + (|Ox| - t'c)^2}{2(ct + (|O_x| - t'c) + O_x \cos(b)\cos(l))} \tag{4.9}$$

where $O_x = -8$ kpc is the Sun's location with respect to the emitting source (assuming $O_y = O_z = 0$), and $-T \leq t' \leq 0$ is the time during the flare of duration T at which the photon was emitted, as illustrated in Fig. 4.11. The region illuminated at a given time is therefore an ellipsoid, with its focus at the observer's position. For the case of an observer located at the Sun's position, this can be approximated, in the proximity of Sgr B2, by a paraboloid (Cramphorn & Sunyaev, 2002). The propagation of the section of the ellipsoid on the x-y plane is illustrated in the left panel of Fig. 4.12 for the case of an instantaneous flare ($T = 0$).

In the case of a flare with finite duration, i.e. $T > 0$, the duration of the flare determines the 'thickness' of the ellipsoid, or in other words the thickness of the region that is simultaneously visible to the observer, as illustrated in the right panel of Fig. 4.12.

The surface brightness observed along a line of sight at a given moment, $I(l, b, t)$, will therefore be determined not by the total optical depth of the cloud in that direction, but rather by the surface density in the section of the cloud that is delimited by the thick paraboloid (Sunyaev & Churazov, 1998), whose boundaries are determined by the beginning and end of the flare. The reflected intensity can therefore be described, under a single scattering approximation, as:

$$I(l, b, t, \nu) = \int_{-T}^{0} \sum_{Z} \frac{\rho(\nu)}{4\pi R^2} n_Z \frac{\mathrm{d}\sigma_Z}{\mathrm{d}\Omega} \exp(-\tau_Z) c \mathrm{d}t' \tag{4.10}$$

where $\rho(\nu)$ is the number of photons/(s keV) emitted by the source, R is the distance from the source to the point of scattering, n_z is the density at the point of scattering, $\frac{\mathrm{d}\sigma_Z}{\mathrm{d}\Omega}$ is the singly-differentiated cross section, computed using the public library xraylib (Schoonjans et al., 2011) and:

$$\tau_Z = \mathrm{NHI}(\sigma_{abs,Z} + \sigma_{scatt,Z}) \tag{4.11}$$

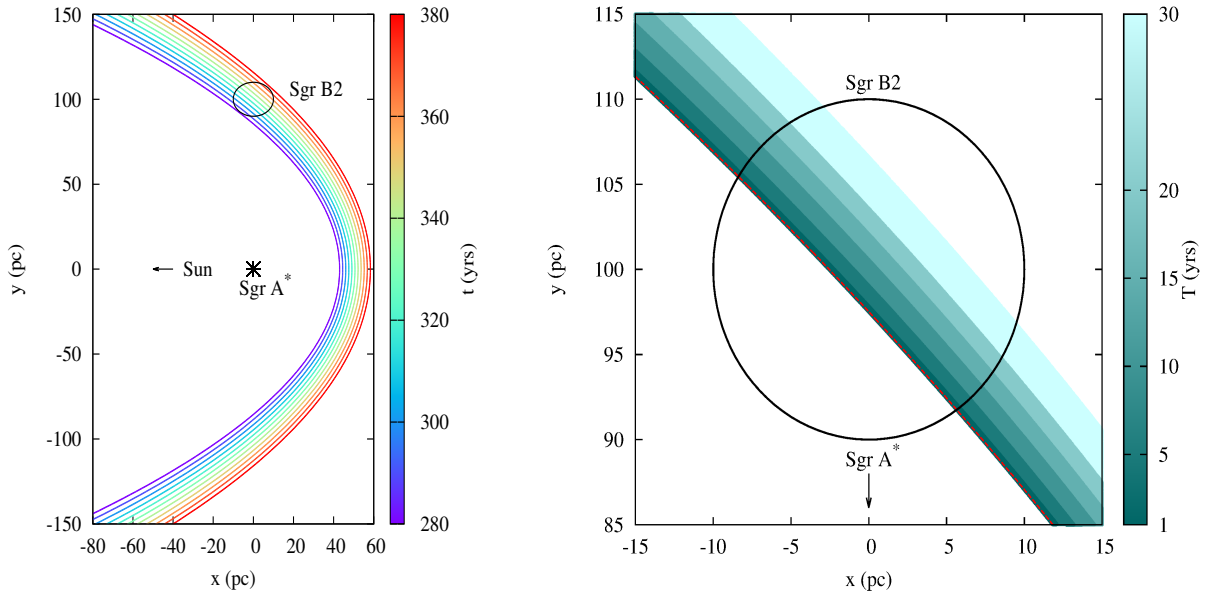

Figure 4.12: *Left plot:* Regions of the x-y plane visible to the observer at different times through scattered X-ray photons, in the case of photons originally emitted by an instantaneous flare of Sgr A* (i.e. all photons emitted at $t = 0$). *Right plot:* Regions of the x-y plane visible to the observer through scattered X-rays at time $t = 320$ yrs in the case of an instantaneous flare (dashed line) and in the case of flares of duration T (coloured maps). The longer the duration of the flare, the thicker the region of the sky observable simultaneously.

is the total optical depth, from the point of emission to the point of observation. To speed-up the calculations, we ignore the contribution of Raman scattering to σ_{scatt}, whose contribution is negligible for this particular geometrical set-up (i.e. for an average scattering angle of $\sim 90°$).

Owing to their higher average density, clumps are able to contribute significantly towards I, by scattering more X-ray flux towards the observer compared to the interclump medium, and hence should be clearly recognisable in the morphology of the XRN at times when they are intercepted by the propagating paraboloid, as first suggested by Sunyaev & Churazov (1998). Once the paraboloid has passed them, the clumps should significantly contribute towards the intervening column density NHI, and therefore still be visible in the morphology of the XRN as regions of absorption.

In Fig. 4.13, we illustrate this in the case of the three clump models that are described at the beginning of the section, both in the case of a short ($T = 1$ yr) and longer ($T = 20$ yr) flare, in a snapshot at time $t = 320$ yr. The intensity and column density for the equatorial, vertical and edge profiles that are indicated on the maps are shown in Figs. 4.14 and 4.15, respectively.

On the maps, the main visible effects are as follows:

- the contribution of clumps towards the scattered intensity is indeed clearly visible in the form of bright spots, consistently with the findings of Zhang et al. (2015);
- intervening clumps located between the source and the point of scattering, or between the point of scattering and the observer (see Fig. 4.15) contribute considerably to the absorption of the X-ray radiation, and are, therefore, observable as regions of absorption in the maps;
- The effect of the duration of the flare is also recognisable: the longer the duration of the flare, the thicker the region of the cloud that is probed by the ellipsoid at the same time, hence the higher the number of clumps that are probed by the paraboloid simultaneously, as clearly seen in the $\mu = 0.01$ model maps.
- In the case of clumps with Sgr B2 mass-size relation, the very small volume they occupy means the probability of a short flare intercepting them is very low, and in fact very few clumps are intercepted at all for this particular distribution, and most clumps are therefore only seen in absorption;
- the intensity of the interclump regions in the Sgr B2 mass-size model (average density $n_{H2} \sim 1 \times 10^3$ cm^{-3}), is higher than that of the homogeneous model (average density $n_{H2} \sim 1 \times 10^4$ cm^{-3}) in the central region of the cloud. This is due to the fact that, although contributing a larger surface density within the thick paraboloid, the homogeneous cloud also results in a larger absorbing column density, as shown in Fig. 4.15;

The reflected intensity at a given time can therefore reveal information on the column density of both the clump and the interclump medium. But it also contains information on the distribution of the clumps inside the cloud.

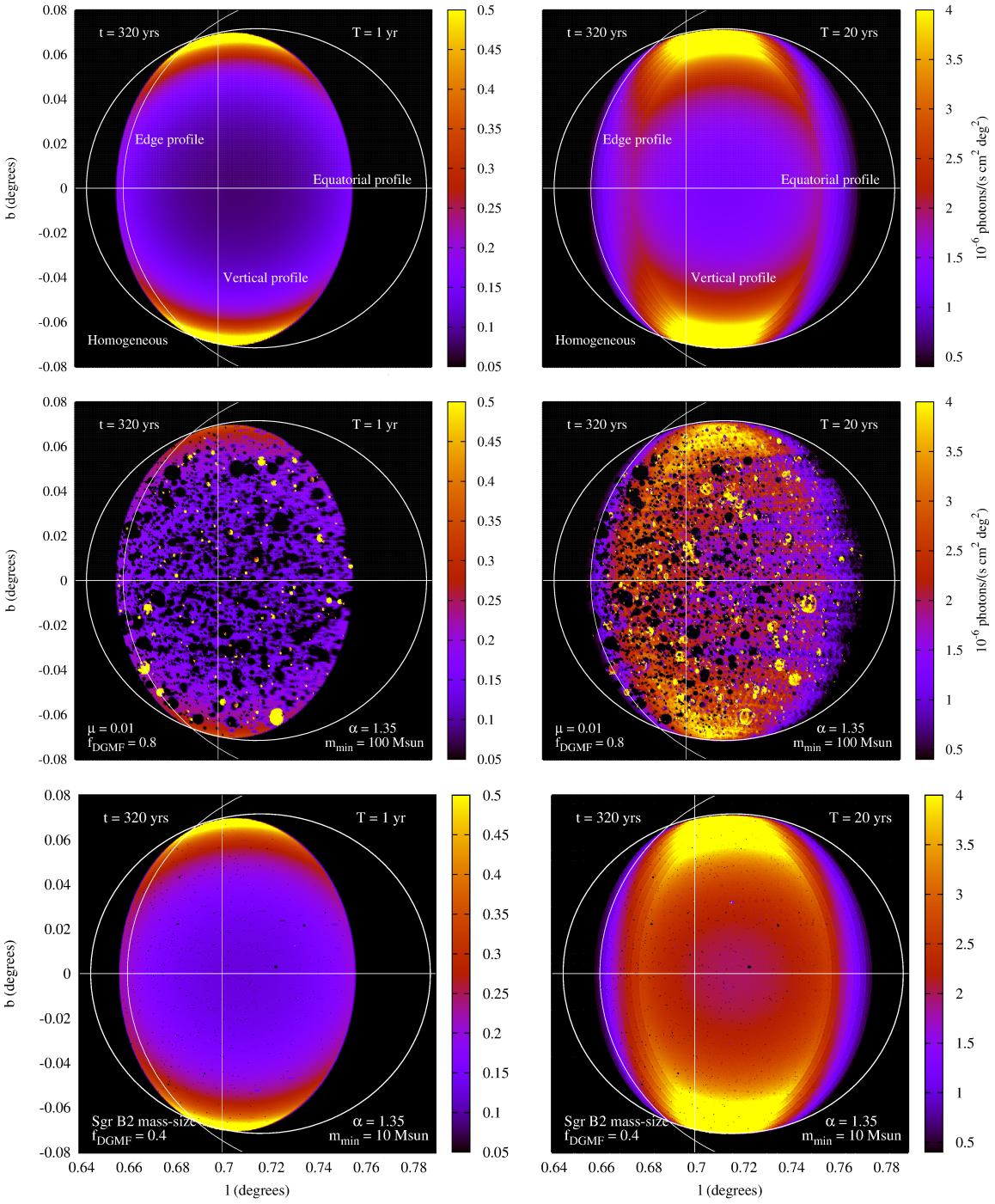

Figure 4.13: Analytic, single scattering approximation of the 3-20keV reflected X-ray intensity observed at time $t = 320$ yrs for the three cloud models discussed in the text, and for the case of a short (1 yr) and long (20 yr) flare.

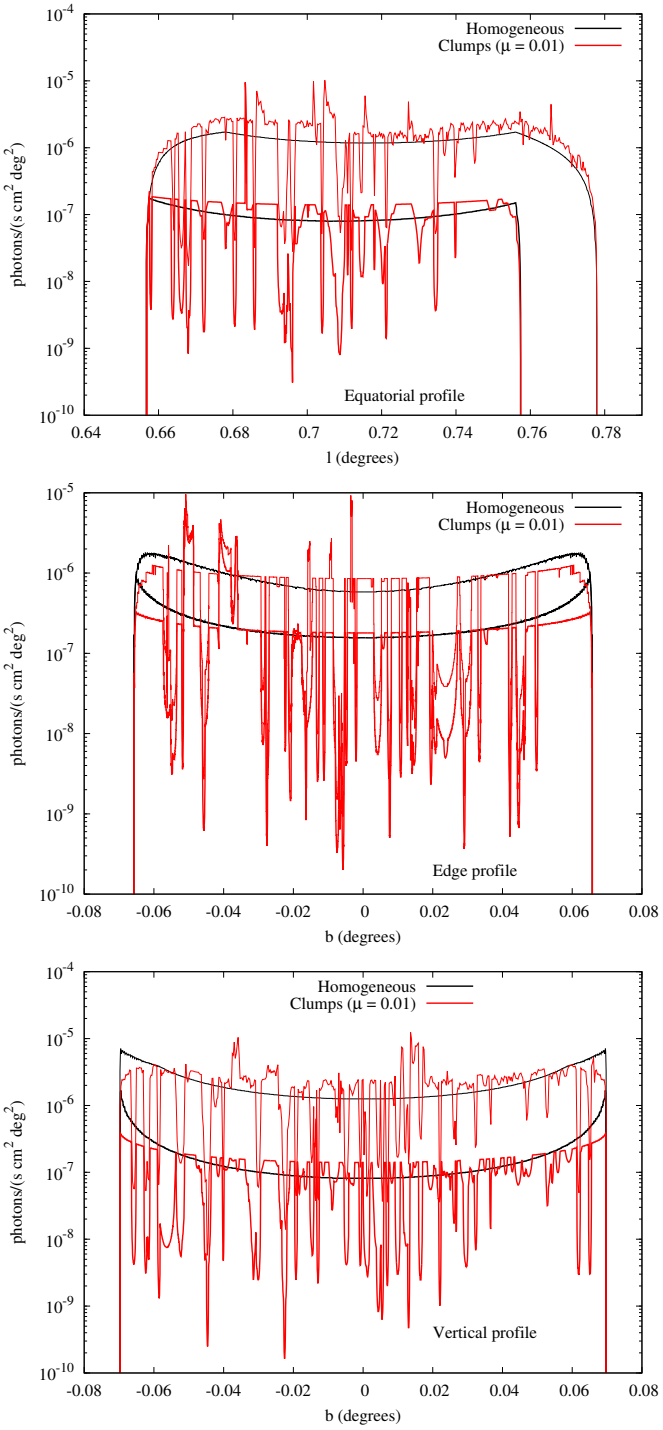

Figure 4.14: Scattered intensity profiles for the homogeneous and $\mu = 0.01$ model for the $T = 1$ yr (thick lines) and $T = 20$ yrs (thin lines).

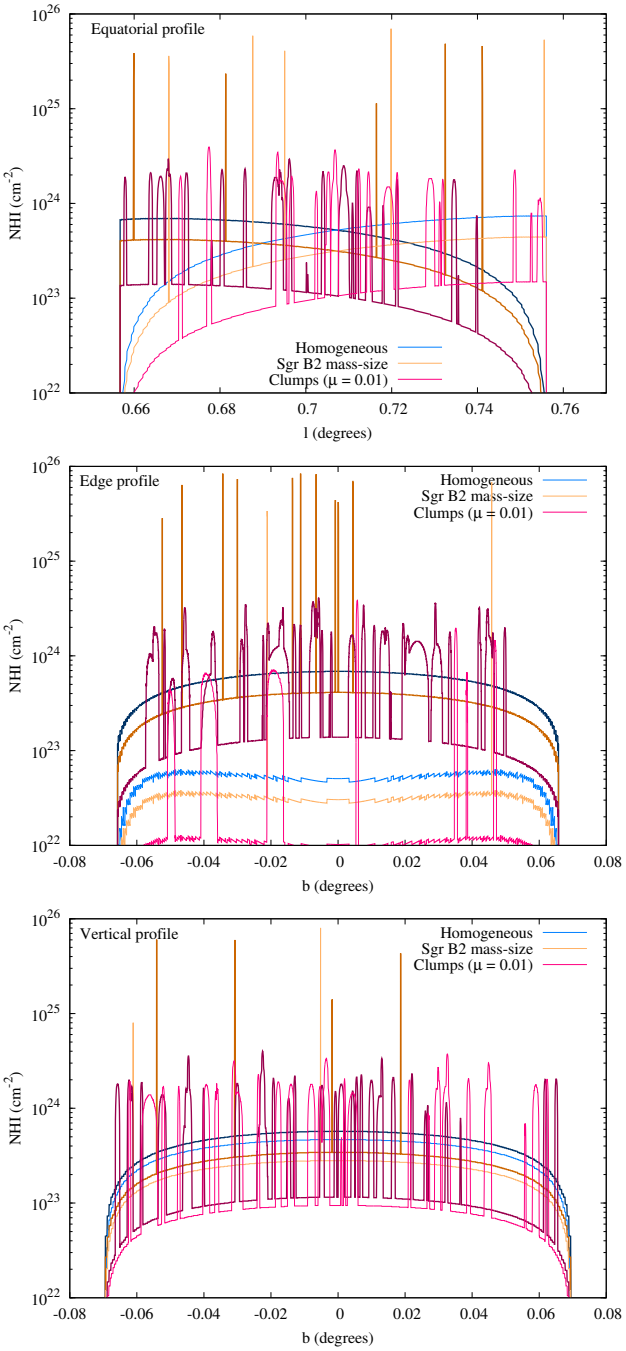

Figure 4.15: Column density from the source to the point of scattering (darker colours) and from the point of scattering to the observer (lighter colours) along profiles indicated in Fig. 4.13 (diffuse envelope not included). The plots show the case of minimum column density ($t' = 0$) at time $t = 320$ yrs.

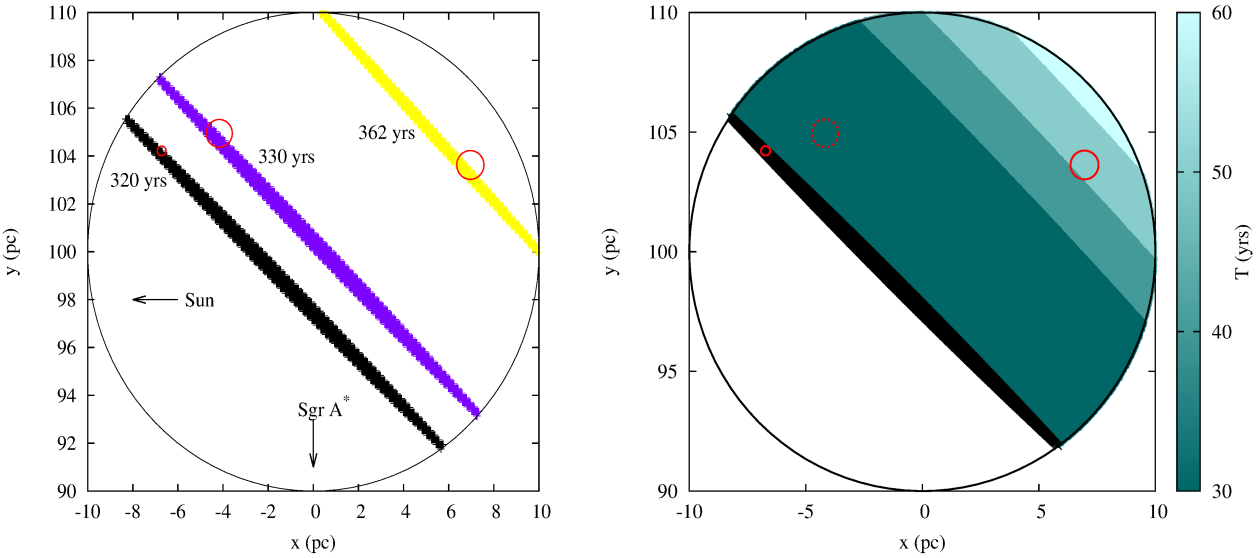

Figure 4.16: *Left plot*: projected location of the clumps inside Sgr B2 and regions inside Sgr B2 visible to the observer at times when the substructures should become visible (assuming illumination by an instantaneous flare). *Right plot*: Projected regions inside the cloud observed simultaneously at time 320 yrs by flares of different durations T (where the black region corresponds to illumination by an instantaneous flare). In the case of the three clumps considered in Fig. 4.17, the minimum flare duration required for the two most further apart clumps (shown with solid red lines in the plot) to both be visible to the observer at the same time is $T \sim 40$ yrs. In the case in which both substructures are visible simultaneously in the reflected X-ray intensity maps, one can infer that the source's flare must have lasted at least $T \sim 40$ yrs.

In the case of a short flare, the distance along the line of sight that is observed at a given time is uniquely defined by the time of observation, since $D(t, t') \sim D(t, t' = 0)$. In this case, by comparing the time at which a clump becomes visible on the reflected intensity map with its location on the sky, it is possible to constrain its position D along the line of sight, as illustrated in the left panel of Fig. 4.16. This kind of analysis could therefore prove to be important when studying the 3D distribution of substructures within GMCs.

For flares of finite duration, on the other hand, a range of distances will be observable at the same time along a given line of sight, as photons are emitted by the source over a period of time T, which determines the 'thickness' of the region observed at a given time. In the case of the known duration of flares, as is the case for many X-ray sources in the Galaxy, the time-evolution of the reflected intensity could still be used in this kind of analysis. On the other hand, in the case of illumination by a flare of unknown duration, on the other hand, it would be impossible to constrain the distance D of each clump along its line of sight, since the range of possible values will be proportional to the duration of the flare itself. On the other hand, if the position of at least two clumps is known, it would

be possible to reverse the problem and infer a lower-bound to the duration of the flare, as illustrated in Fig. 4.16.

The visibility of clumps in the reflected X-ray intensity, their localised nature, and the non-persistent illumination from external flaring sources such as Sgr A*, make the time-evolution of the X-ray morphology of Sgr B2 and similar XRNe an ideal target in the study of the spatial distribution of clumps within them. We leave the study of the intensity light curve of individual clumps, as a function of photon energy, for different clump sizes and optical depths, for future work.

4.6 Conclusions

We studied the effect of clumps on the X-ray emission of GMCs that act as XRNe by modelling Sgr B2, one of the brightest and most massive XRNe in our Galaxy.
In particular, we studied the effect of the internal structure of GMCs on the properties of X-ray spectrum, polarisation and morphology reflected from them. We have considered both persistent sources and transients, in particular giant flares, as the source of incident X-rays. We use Sgr B2 as a case study, but most of our results are generally applicable to any GMC in the Galaxy. We defined a simple clump model for simplicity. We investigated the effect of different clump population model parameters on the reflected X-ray energy and polarisation spectrum. The parameters that we investigated included the fraction of the total mass of the cloud contained in clumps ($f_{\rm DGMF}$), the slope of the clump mass function (α), the minimum mass of clumps found in the population (m_{min}), and the mass-size relation of individual clumps ($m = m_{norm}(r/pc)^{\gamma}$). First, we considered a fixed mass-size relation that was consistent with the clumps observed in Sgr B2, and varied each of the remaining parameters around a fiducial model given by $_{DGMF} = 0.4$, $m_{min} = 10M_{\odot}$, and $\alpha = 1.35$, assessing their effect on the overall reflected X-ray spectrum.
In this case, the volume-filling fraction of the clumps, and therefore the relative probability of X-rays being scattered by gas in clumps compared to the interclump medium, is negligible. The cloud therefore appears in X-rays as having a mass smaller than the total mass by the amount that is clumped. The extremely low volume-filling fraction, which was obtained when assuming the mass-size relation observed in Sgr B2, allows these clumps to effectively 'hide' a fraction $f_{\rm DGMF}$ of the cloud's mass in an extremely small fraction of the cloud's volume. We explicitly check this hypothesis by considering the case of homogeneous clouds containing (1-$f_{\rm DGMF}$) of the cloud's original mass and no clumps at all. In cases where the mass-size relation of clumps means these occupy a much higher volume-filling fraction, we find that clumps do contribute towards reflection, and that the reflected X-rays contain information about the internal structure of the cloud. The parameters of the clumping model could therefore be constrained by X-ray observations.

We also investigated how the time evolution of the spatially-resolved images of the reflected X-ray intensity can be used to probe the location of individual substructures along the line of sight in the case where the incident X-rays have a transient origin, such as a short-duration flare from a X-ray binary or the supermassive black hole at the centre of

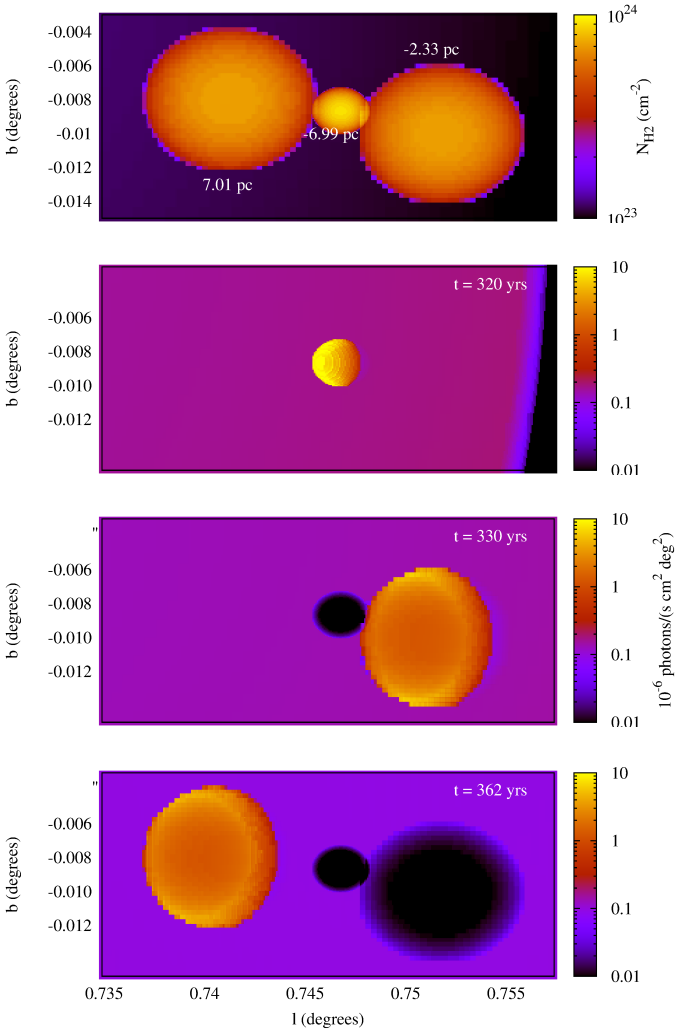

Figure 4.17: *Top plot*: Column density map of three simulated clumps within Sgr B2, found in a small region of the sky (labels in plot indicate the clumps' distance from the centre of the cloud, approximated as $D - D_{\mathrm{SgrB2}}$). *Second, third and fourth plot*: reflected X-ray intensity reaching the observer at different times. Despite the apparent proximity of the clumps on the sky, because of the different distance at which they are located along the line of sight, the clumps are visible through their reflected X-ray emission at different times, so that when one is visible, the others are not.

our Galaxy. We have shown that in the case of transient sources, the timing information, retrievable both in emission and in absorption, can be used to probe the third dimension along the line of sight, opening up the possibility of 3D tomography of the cloud. Future X-ray observatories such as Astro-H (Takahashi et al., 2010), Athena (Barcons et al., 2012), and the X-ray Surveyor (Weisskopf et al., 2015) could therefore open up a new probe of the internal structure of GMCs. The recent pre-selection of the X-ray polarimeters IXPE (Weisskopf et al., 2014), XIPE (Soffitta et al., 2013), PRAXyS (Jahoda et al., 2015) or the XTP (Wang et al., 2014) instruments could further complement spectrographic studies to polarimetric ones.

Chapter 5

ISM distortion of the CXB spectrum

5.1 The CXB emission

In Chapter 2, I discussed the nature of the two large-scale, apparently diffuse X-ray emission components that are observed across the sky: the GRXE, which is highly anisotropic and characteristically concentrated on the plane of the Galaxy, and the CXB, which is remarkably isotropic in the 3-300 keV band on subarsec scales. While the former is believed to result from the direct and, as demonstrated in this thesis, indirect contribution of sources located in the Galaxy (see Chapter 2), the latter is believed to result from the superposition of a large number of extragalactic sources (Giacconi et al., 2002). In particular, the CXB is believed to represent the radiative imprint of the growth of supermassive black holes across cosmic time, as they shine inside AGN (Gilli, 2013). We can, therefore, use the CXB to quantify the efficiency of accretion, which is believed to drive the majority of SMBH growth, throughout the Universe's evolution (Brandt & Alexander, 2015; Harrison et al., 2015).

When studying this emission, we are, however, limited by the fact that photons emitted by extragalactic sources must travel through the Galactic ISM before being observed inside the Galaxy. The image of the CXB that we observe therefore contains the imprint of the interaction photons had with this interstellar gas. This interaction may indeed result in distortions which need to be quantified in order to differentiate the original spectral properties of the sources from the effect of photon propagation inside the Galaxy. In this Chapter, we provide a quantitative estimate for what this distortion should be, and discuss its relevance in potentially giving rise to anisotropies in the CXB emission.

5.2 CXB interaction with the ISM

If we assume that the emission is isotropic, CXB photons illuminate the gas in the ISM with equal intensity from all directions. This results in an equal probability of the incoming radiation being scattered away from, and into, the line of sight of the observer by the intervening gas, as illustrated in Fig. 5.1. In the case of elastic scattering, this causes

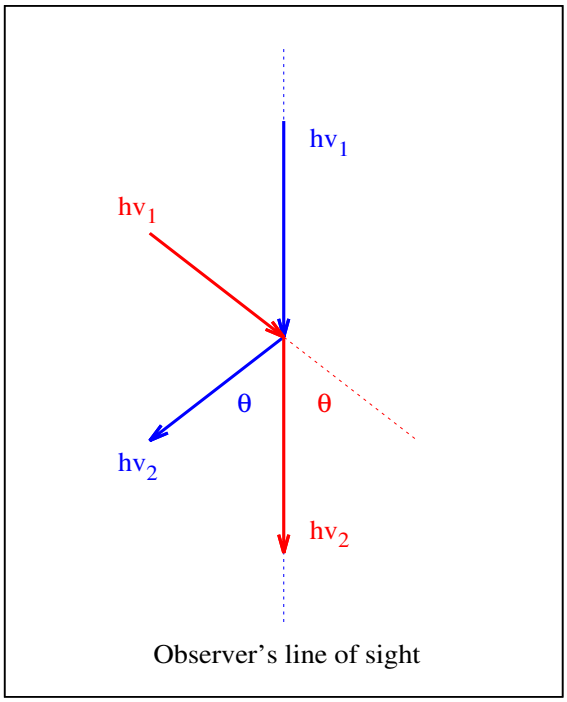

Figure 5.1: Diagram describing the effect of ISM scattering under illumination by an isotropic emission such as the CXB. Because the probability of scattering at angle θ is the same for all incoming ($h\nu_1$) photons, the probability of a photon being scattered away from the observer's line of sight (blue in the diagram) is the same as that of a photon coming from a different direction being scattered into the observer's line of sight (red in the diagram). If the scattering process is elastic, that is $h\nu_2 = h\nu_1$, the interaction leaves no observational signatures. If, on the other hand, the scattering is inelastic, and $h\nu_2 \neq h\nu_1$, the observed spectrum along that line of sight will be distorted by its interaction with the ISM.

the interaction of CXB photons with the gas to leave no observational signature on the emission as it propagates through the scattering medium, even though the ISM is highly anisotropic and mostly concentrated in the Galactic plane. Inelastic scattering, on the other hand, would result in a net distortion of the original CXB spectrum, and therefore leave an observable imprint on the radiation. This process is similar - but opposite - to the distortion of the cosmic microwave background (CMB) spectrum caused by upscattering of cold CMB photons by the energetic electrons (e.g. in clusters of galaxies) through inverse Compton scattering, known as the Sunyaev-Zeldovich effect (Zeldovich & Sunyaev, 1969). In this chapter, we briefly consider and quantify this effect by studying the possible distortions in the spectral emission resulting from the Compton scattering of CXB photons by electrons in the Galaxy's ISM.

In our calculations, we assume an initial spectrum described by the exponential $\times$

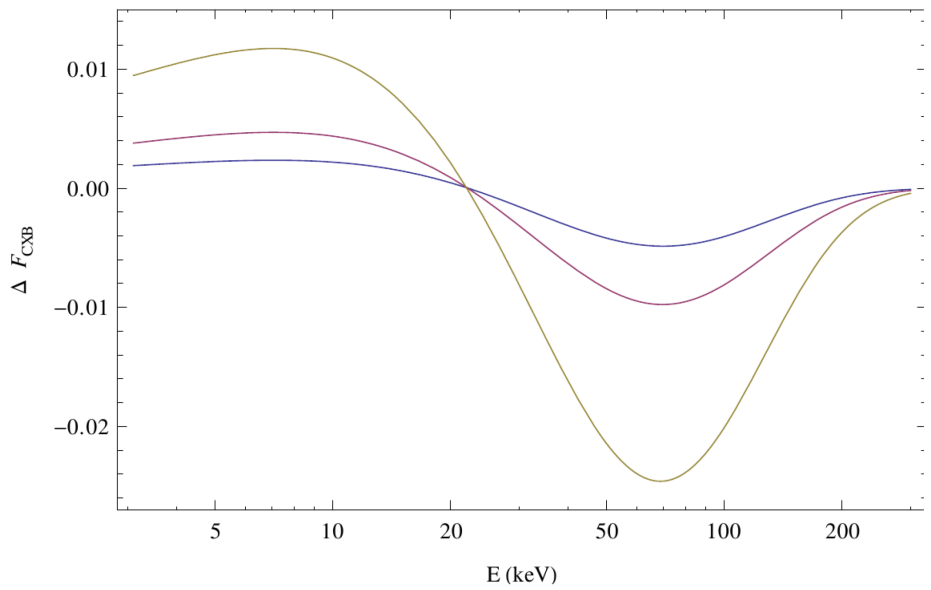

Figure 5.2: Difference between the original and distorted CXB specific intensity $\Delta F_{\rm CXB}(E)$ in units of keV cm^{-2} s^{-1} sr^{-1} keV^{-1}, for $\tau_{\rm max} = 0.1$ (*blue*), $\tau_{\rm max} = 0.2$ (*red*), $\tau_{\rm max} = 0.5$ (*green*).

power-law fit suggested by Gruber et al. (1999), described by:

$$3 - 60\text{keV} : F_{\rm CXB}(t=0,E) = 7.877\left(\frac{E}{1\text{keV}}\right)^{-0.29} e^{(-E/41.13\text{keV})} \frac{\text{keV}}{\text{keV cm}^2\text{ s sr}} \tag{5.1}$$

$$> 60\text{keV} : F_{\rm CXB}(t=0,E) = 0.0259\left(\frac{E}{60\text{keV}}\right)^{-5.5} + 0.504\left(\frac{E}{60\text{keV}}\right)^{-1.58} \tag{5.2}$$

$$+ 0.0288\left(\frac{E}{60\text{keV}}\right)^{-1.05} \frac{\text{keV}}{\text{keV cm}^2\text{ s sr}} \tag{5.3}$$

We calculate the time evolution of the CXB spectrum, $F_{\rm CXB}(t,E)$, by making use of Eq. 25 in Illarionov & Syunyaev (1972), which includes relativistic corrections, derived in Cooper (1971), to the kinetic equation for Compton interaction of Maxwellian electrons with an isotropic radiation field calculated in Kompaneets (1957). The effect of electrons being bound in atoms will only be significant at a photon energy ~ 1 keV, and can therefore be assumed to be negligible at the energy range considered here (3-300 keV). The equation we solve is the following:

$$\frac{\partial f}{\partial t} = \frac{\sigma_T N_e}{m_e c} \frac{E^2}{1+\beta E+\gamma E^2} \frac{\partial f}{\partial E} \tag{5.4}$$

where $f = EF_{\rm CXB}(t,E)/(1+\beta E+\gamma E^2)$, N_e is the electron density, σ_T is the Thomson scattering cross section, m_e is the electron mass, and constant factors have values $\beta = 9\times10^{-3}\text{keV}^{-1}$ and $\gamma = 4.2\times10^{-6}\text{keV}^{-2}$, as estimated in Illarionov & Syunyaev (1972).

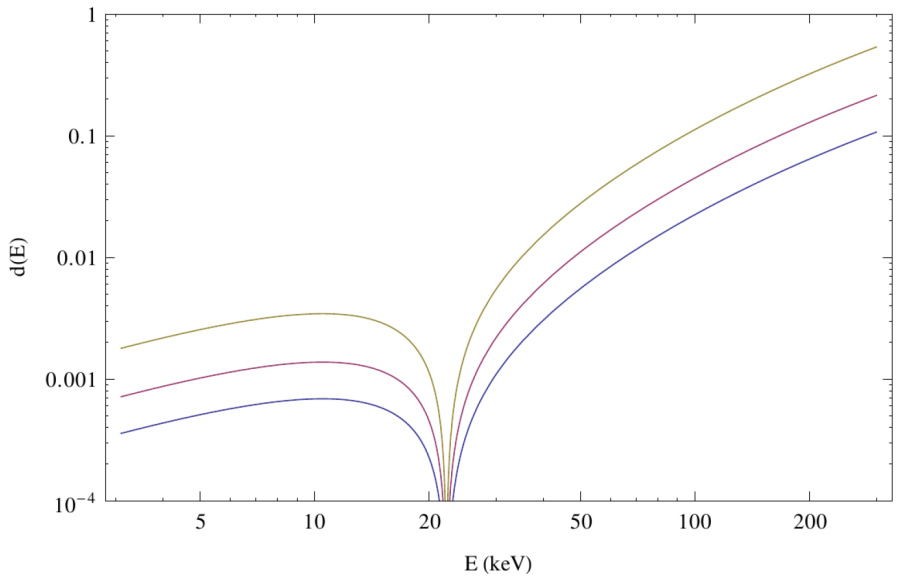

Figure 5.3: Distortion in the CXB spectrum due to ISM Compton scattering, plotted as the fractional difference $d(E)$ between the initial and final spectra for $\tau_{\max} = 0.1$ (*blue*), $\tau_{\max} = 0.2$ (*red*), $\tau_{\max} = 0.5$ (*green*).

By substituting $\tau(t) = \sigma_T N_e ct$ into Eq. 5.4, this reduces to:

$$\frac{\partial f}{\partial \tau} = \frac{1}{m_e c^2} \frac{E^2}{1 + \beta E + \gamma E^2} \frac{\partial f}{\partial E} \tag{5.5}$$

We find an approximate analytic solution for this equation following a method analogous to the CMB y-distortion solution of the Kompaneets equation (Zeldovich & Sunyaev, 1969). The average fractional energy transferred in each scattering is $\sim h\nu/m_e c^2$, where $h\nu \sim 20$ keV is the average photon energy; since τ represents the average number of scattering processes undergone by each photon, the total change in the signal can be parametrised as $y_X = \tau \times (h\nu/m_e c^2)$.

Assuming the deviations from the original spectrum are small, we can approximate the solution by considering a zeroth order expansion of the spectrum around $\tau = 0$ and integrating Eq. 5.5 over the time dependent variable. Because the average change in the spectrum is parametrised by $y_X \propto \tau$, we would then expect the error in this approximation to be linear in y_X.

By applying this method, we obtain the following linear approximation to the change in the spectrum $\Delta F_{\rm CXB}$:

$$\Delta F_{\rm CXB} = \frac{\tau E}{m_e c^2} \frac{\partial}{\partial E} f(0, E) \left[\frac{b - cE - dE^2 - eE^3}{(1 + \beta E + \gamma E^2)^2} \right] \tag{5.6}$$

where b, c, d, and e are constants fixed by initial conditions.

This is shown for values of $\tau = 0.1$, 0.2, 0.5 in Fig. 5.2. These values correspond to relatively high optical depths, which are only found in the most extreme Galactic environments, such as GMCs in the Galactic centre region (see Chapter 4). The distortions in the CXB spectrum considered at these optical depths can therefore be considered to be an upper-bound to the possible distortion effect.

For the same values of τ, we also show (see Fig. 5.3) the fractional difference $d(E)$ between the spectrum at a time $t_{\rm f} = t_{\rm f}(\tau)$ and the initial spectrum at $\tau = 0$, as follows:

$$d(E) = |F_{\rm CXB}(t_{\rm f}, E)/F_{\rm CXB}(0, E) - 1| \tag{5.7}$$

5.3 Conclusions

From Figs. 5.2 and 5.3, we notice that there is a change in the sign of the distortion of the photon spectrum at $E \sim 20$keV, where the distortion changes from positive to negative as photons lose energy to the ISM. This is in itself a demonstration of the fitness of the y_X parametrisation in the description of the Compton scattering effect. We also notice that the maximum possible distortion to the spectrum that we would observe due to the travelling of photons through some of the most dense regions of the Galaxy (eg. for $\tau = 0.5$), is very small: the greatest distortion obtained at this optical depth is $\Delta_{\rm CXB} = 0.025$ keV cm^{-2} s^{-1} sr^{-1} keV^{-1} at 70 keV. This small effect could not be observed with present day instruments. This interesting effect is unfortunately very small even for relatively large optical depths, and will therefore be extremely challenging to observe.

In conclusion, our modelling indicates that the Galactic ISM does not have a significant effect on the observed CXB spectrum.

Chapter 6

Conclusions

In this thesis, I have endeavoured to illustrate the versatility offered by models of the interaction between X-rays and the ISM. I have discussed a number of applications relevant on all galactic scales, and involving a wide range of X-ray sources. In this section, we summarise the main results discussed in this thesis, and discuss future work relevant to each case.

A truly diffuse component of the Galactic Ridge X-ray emission

- The reprocessing by the ISM of X-rays emitted by the brightest class of X-ray sources in the Milky Way, XBs, gives rise to a Galactic-scale diffuse emission whose surface density is dependent on the total luminosity of the XB population averaged over the past 1000-10000 yrs.

- This emission should constitute a truly diffuse component of the GRXE, until now believed to be of discrete origin and to result solely from the the cumulative emission of low-luminosity stellar sources in the Galaxy, namely CVs and ASBs (Revnivtsev et al., 2009). The lower bound on the relative contribution of the truly diffuse component is 10-30% of the stellar one on the Galactic plane in the 3-20 keV range.

- The diffuse and discrete components are distinguishable by the morphology of the gas and stellar mass distribution from which they respectively originate. In particular: a) the different scale height of the two components, due to the scale height of the gaseous disk ($\sim$ 80 pc) being lower than that of the stellar disk ($\sim$ 130 pc) and b) the sub-degree fluctuation of the scattered component due to the clumping of atomic and molecular gas in the Galaxy, which cannot occur in the case of contribution from discrete sources (Sugizaki et al., 2001).

- The quantitative comparison of the discrete and diffuse components can help constrain the population properties of XBs, CVs and ASBs in the Milky Way. In particular, we have shown that current observations of the GRXE are consistent with

an average Milky Way XB activity more similar to those of other galaxies than it is possible to directly observe.

- **Future work:** The contribution of the stellar component to the 6.4keV neutral-iron fluorescent line is believed to be insufficient in explaining its observed equivalent width (EW) in the GRXE spectrum (Warwick, 2014). The scattered component is expected to contribute significantly towards this line, as a result of the photoionisation of the cold ISM by hard X-ray photons. However, theoretical predictions of this contribution are presently not available. Future work should focus on obtaining an estimate of the 6.4keV line contribution from the scattered GRXE. This would allow us to a) compare the contribution of the scattered component to the 6.4 keV line's EW in regions of the sky in which both GRXE observations and estimates of the stellar contribution are available. And b) obtain a Galactic-scale morphology of the line that can be compared to those of other emission lines - mainly contributed to by the stellar GRXE - as a probe of the relative contribution of the two components at different locations.

Contribution of XBs to the ISM heating

- The illumination of the ISM by XB radiation results in the heating of the gas through photoionisation and inelastic scattering. The energy deposition rate is comparable to that of cosmic rays, although its distribution is morphologically extremely different, as it is highly localised around bright sources, whereas cosmic-rays, due to the fact that they propagate for a long time, deposit energy in a more uniform way throughout the Galaxy.

- **Future work:** Studies of the chemical composition of GMCs in the Central Molecular Zone (CMZ) of the Milky Way, in particular within the dense cores of Sgr B2, have revealed a far more complex chemistry than initially expected (eg Belloche et al 2009). In order to understand the formation process of these molecules within the dense regions of Sgr B2, it is necessary to understand the role that heating played in the evolution of the cloud. Sources of heating normally considered include UV radiation from nearby young stars, shocks, and cosmic rays. But another important source of heating, which must have contributed towards the chemical evolution of Sgr B2, is the supermassive black hole at the centre of the Galaxy, Sgr A*. Although presently under-luminous, indirect evidence suggests that Sgr A* must have been brighter in the past (eg. Ponti et al 2013), and emitted bright X-ray flares which illuminated the surrounding GMCs. X-ray photons emitted during such flares should have reached the cloud and, due to their relatively long mean free path, penetrated deep into the dense regions of gas which would have otherwise been screened from all sources of heating but cosmic rays.

  In this thesis, I have shown that, in a general context, heating by hard ($\gtrsim$ 1 keV) photons should dominate heating by cosmic rays in the proximity of X-ray sources.

An important next step would therefore be to model the Sgr B2 - Sgr A* system itself, to determine if Sgr A* is a dominant source of heating in this specific case. This would allow us to investigate the morphology of the energy deposition distribution for different models of the cloud's internal structure and of the flaring activity of Sgr A*, and to compare it to other sources of heating. The comparison of the resulting X-ray heating morphology with that of other sources of heating (eg Etxaluze et al. (2013)) could further provide us with an indirect probe of the past flaring activity of Sgr A*.

Probing the clumping structure of Giant Molecular Clouds through the spectrum, polarisation and morphology of X-ray reflection nebulae

- The clumping structure of GMCs which act as XRNe has an observable effect on the polarisation and energy spectrum of the reflected X-ray emission, and should therefore be accounted for in models of this phenomenon.

- For mass-size relations observed in clumps inside Sgr B2, the most massive XRN in the Galactic centre region, the reflected X-ray emission is expected to only be sensitive to the interclump medium inside the XRN. By comparing estimates of the interclump mass obtained from the reflected X-ray emission with independent estimates of the overall mass of the XRN, it should therefore possible to obtain estimates for the fraction of mass of the XRN inside overdense regions, $f_{\rm DGMF}$.

- The volume filling fraction of dense regions within these molecular complexes can be estimated from considerations of the relative EWs of the Fe K-α's shoulder and line in the reflected spectrum.

- For mass-size relations yielding volume filling factors larger than those observed in Sgr B2, the reflected X-ray emission becomes sensitive to clump population parameters such as the CMF and minimum clump mass. Studies of the reflected X-ray energy and polarisation spectra from XRNe can therefore help constrain these parameters.

- The time-evolution of the X-ray morphology of XRN under illumination by short flares can be used to infer the 3D distribution of the clumps inside the cloud, which are visible both as bright spots and regions of absorption in the GMC's X-ray emission.

- **Future work:** Future X-ray polarimeters, such as IXPE, XIPE, PRAXyS or the XTP, will also open up the possibility of observationally investigating such molecular structures through their polarisation of the reflected emission. Theoretical models investigating the polarisation of the reflected emission, however, have so far neglected to include the effect of source polarisation on the reflected light. The polarisation of the flares emitted by Sgr A* should have an, as yet unknown, effect on both the observed polarisation and spectrum. This effect should be modelled in order to quantify its impact and allow it to be incorporated into the analysis of future observational studies.

ISM distortion of the CXB spectrum

- The propagation of CXB photons through the ISM results in small distortions to the spectrum, due to the inelastic scattering on electrons. Such distortions are characterised by a small decrease of CXB flux above - and increase in the flux below - ~ 20 keV, as energetic photons lose their energy to cold electrons through Compton scattering.

- This effect is proportional to the optical depth of the ISM, and therefore introduces an element of anisotropy in this extragalactic emission.

- For an optical depth of $\tau = 0.5$, as it is observed in some of the most dense Galactic environments, the maximum distortion obtained is $\Delta_{\mathrm{CXB}} = 0.025$ keV cm^{-2} s^{-1} sr^{-1} keV^{-1} at 70 keV. This small effect could not be observed with present day instruments.

Bibliography

Allemand, C. D., Depolarization Ratio Measurements in Raman Spectrometry, Applied Spectroscopy **24** (1970) 348–353

Asplund, M., Grevesse, N., Sauval, A. J., & Scott, P., The Chemical Composition of the Sun, ARA&A **47** (Sep. 2009) 481–522, arXiv:0909.0948 [astro-ph.SR]

Baganoff, F. K., Bautz, M. W., Brandt, W. N., et al., Rapid X-ray flaring from the direction of the supermassive black hole at the Galactic Centre, Nature **413** (Sep. 2001) 45–48, astro-ph/0109367

Baganoff, F. K., Maeda, Y., Morris, M., et al., Chandra X-Ray Spectroscopic Imaging of Sagittarius A* and the Central Parsec of the Galaxy, ApJ **591** (Jul. 2003) 891–915, astro-ph/0102151

Bahcall, J. N. & Soneira, R. M., The universe at faint magnitudes. I - Models for the galaxy and the predicted star counts, ApJS **44** (Sep. 1980) 73–110

Bambynek, W., Crasemann, B., Fink, R. W., et al., X-ray Fluorescence Yields, Auger, and Coster-Kronig Transition Probabilities, Rev. Mod. Phys. **44** (Oct. 1972) 716

Bandyopadhyay, R. M., Shahbaz, T., Charles, P. A., & Naylor, T., Infrared spectroscopy of low-mass X-ray binaries - II, MNRAS **306** (Jun. 1999) 417–426, astro-ph/9901327

Barcons, X., Barret, D., Decourchelle, A., et al., Athena (Advanced Telescope for High ENergy Astrophysics) Assessment Study Report for ESA Cosmic Vision 2015-2025, ArXiv e-prints (Jul. 2012), arXiv:1207.2745 [astro-ph.HE]

Barger, A. J., Cowie, L. L., Mushotzky, R. F., et al., The Cosmic Evolution of Hard X-Ray-selected Active Galactic Nuclei, AJ **129** (Feb. 2005) 578–609, astro-ph/0410527

Battisti, A. J. & Heyer, M. H., The Dense Gas Mass Fraction of Molecular Clouds in the Milky Way, ApJ **780** (Jan. 2014) 173, arXiv:1312.0643

Bergstrom, P. M., Surić, T., Pisk, K., & Pratt, R. H., Physical Review A **48** (1993) 1134–1162

Bildsten, L. & Chakrabarty, D., A Brown Dwarf Companion for the Accreting Millisecond Pulsar SAX J1808.4-3658, ApJ **557** (Aug. 2001) 292–296, astro-ph/0104153

Binney, J. & Tremaine, S. 2008, Galactic Dynamics: Second Edition, , Princeton University Press

Blitz, L., Giant molecular clouds, in Protostars and Planets III, ed. E. H. Levy & J. I. Lunine. 1993, 125–161, ADS

Brandt, W. N. & Alexander, D. M., Cosmic X-ray surveys of distant active galaxies. The demographics, physics, and ecology of growing supermassive black holes, A&A Rev. **23** (Jan. 2015) 1, arXiv:1501.01982 [astro-ph.HE]

Capelli, R., Warwick, R. S., Porquet, D., Gillessen, S., & Predehl, P., The X-ray lightcurve of Sagittarius A* over the past 150 years inferred from Fe-Kα line reverberation in Galactic centre molecular clouds, A&A **545** (Sep. 2012) A35, arXiv:1207.1436 [astro-ph.HE]

Chen, C.-Y. & Ostriker, E. C., Anisotropic Formation of Magnetized Cores in Turbulent Clouds, ApJ **810** (Sep. 2015) 126, arXiv:1508.02710

Churazov, E., Sunyaev, R., & Sazonov, S., Polarization of X-ray emission from the Sgr B2 cloud, MNRAS **330** (Mar. 2002) 817–820, astro-ph/0111065

Clavel, M., Terrier, R., Goldwurm, A., et al., Echoes of multiple outbursts of Sagittarius A* revealed by Chandra, ArXiv e-prints (Jul. 2013), arXiv:1307.3954 [astro-ph.HE]

Cohen, R. S. & Thaddeus, P., An out-of-plane galactic carbon monoxide survey, ApJ **217** (Nov. 1977) L155–L159

Colbert, E. J. M., Heckman, T. M., Ptak, A. F., Strickland, D. K., & Weaver, K. A., Old and Young X-Ray Point Source Populations in Nearby Galaxies, ApJ **602** (Feb. 2004) 231–248, arXiv:astro-ph/0305476

Cooper, G., Physical Review D **3** (1971) 2312–2316

Cox, D. P., The Three-Phase Interstellar Medium Revisited, ARA&A **43** (Sep. 2005) 337–385

Cramphorn, C. K. & Sunyaev, R. A., Interstellar gas in the Galaxy and the X-ray luminosity of Sgr A* in the recent past, A&A **389** (Jul. 2002) 252–270, astro-ph/0108294

Dalton, W. W. & Sarazin, C. L., High-mass X-ray binary populations. 1: Galactic modeling, ApJ **440** (Feb. 1995) 280–296

Dame, T. M., Hartmann, D., & Thaddeus, P., The Milky Way in Molecular Clouds: A New Complete CO Survey, ApJ **547** (Feb. 2001) 792–813, astro-ph/0009217

Dehnen, W. & Binney, J., Mass models of the Milky Way, MNRAS **294** (Mar. 1998) 429, astro-ph/9612059

Dobbs, C. L. & Burkert, A., The myth of the molecular ring, MNRAS **421** (Apr. 2012) 2940–2946, arXiv:1201.1775 [astro-ph.GA]

Dogiel, V., Cheng, K.-S., Chernyshov, D., et al., Origin of 6.4keV Line Emission from Molecular Clouds in the Galactic Center, PASJ **61** (Aug. 2009) 901–907

Donkov, S., Veltchev, T. V., & Klessen, R. S., Mass-density relationship in molecular cloud clumps, MNRAS **418** (Dec. 2011) 916–928, arXiv:1010.5622 [astro-ph.SR]

Draine, B. T. 2011, Physics of the Interstellar and Intergalactic Medium, , Princeton University Press

Dwek, E., Arendt, R. G., Hauser, M. G., et al., Morphology, near-infrared luminosity, and mass of the Galactic bulge from COBE DIRBE observations, ApJ **445** (Jun. 1995) 716–730

Ebisawa, K., Maeda, Y., Kaneda, H., & Yamauchi, S., Origin of the Hard X-ray Emission from the Galactic Plane, Science **293** (Aug. 2001) 1633–1635, astro-ph/0108406

Ebisawa, K., Tsujimoto, M., Paizis, A., et al., Chandra Deep X-Ray Observation of a Typical Galactic Plane Region and Near-Infrared Identification, ApJ **635** (Dec. 2005) 214–242, astro-ph/0507185

Ebisawa, K., Yamauchi, S., Tanaka, Y., et al., Spectral Study of the Galactic Ridge X-Ray Emission with Suzaku, PASJ **60** (Jan. 2008) 223, arXiv:0711.2962

Eisenberger, P. & Platzman, P. M., Compton Scattering of X Rays from Bound Electrons, Phys. Rev. A **2** (Aug. 1970) 415–423

Etxaluze, M., Goicoechea, J. R., Cernicharo, J., et al., Herschel observations of the Sagittarius B2 cores: Hydrides, warm CO, and cold dust, A&A **556** (Aug. 2013) A137, arXiv:1307.0335 [astro-ph.GA]

Field, G. B., Goldsmith, D. W., & Habing, H. J., Cosmic-Ray Heating of the Interstellar Gas, ApJ **155** (Mar. 1969) L149

Filippova, E. V., Tsygankov, S. S., Lutovinov, A. A., & Sunyaev, R. A., Hard Spectra of X-ray Pulsars from INTEGRAL Data, Astronomy Letters **31** (Nov. 2005) 729–747, astro-ph/0509525

Freudenreich, H. T., The Shape and Color of the Galactic Disk, ApJ **468** (Sep. 1996) 663

Gando Ryu, S., Nobukawa, M., Nakashima, S., et al., X-ray Echo from the Sagittarius C Complex and 500-year Activity History of Sagittarius A*, ArXiv e-prints (Nov. 2012), arXiv:1211.4529 [astro-ph.GA]

Giacconi, R., Gursky, H., Paolini, F. R., & Rossi, B. B., Evidence for x Rays From Sources Outside the Solar System, Physical Review Letters **9** (Dec. 1962) 439–443

Giacconi, R., Zirm, A., Wang, J., et al., Chandra Deep Field South: The 1 Ms Catalog, ApJS **139** (Apr. 2002) 369–410

Gilfanov, M., Low-mass X-ray binaries as a stellar mass indicator for the host galaxy, MNRAS **349** (Mar. 2004) 146–168, arXiv:astro-ph/0309454

Gilfanov, M., Grimm, H.-J., & Sunyaev, R., Statistical properties of the combined emission of a population of discrete sources: astrophysical implications, MNRAS **351** (Jul. 2004) 1365–1378, astro-ph/0312540

Gilfanov, M., Revnivtsev, M., & Molkov, S., Boundary layer, accretion disk and X-ray variability in the luminous LMXBs, A&A **410** (Oct. 2003) 217–230, astro-ph/0207575

Gilli, R., The cosmic X-ray background: abundance and evolution of hidden black holes., Mem. Soc. Astron. Italiana **84** (2013) 647, arXiv:1304.3665 [astro-ph.CO]

Ginsburg, A., Bally, J., Battersby, C., et al., The dense gas mass fraction in the W51 cloud and its protoclusters, A&A **573** (Jan. 2015) A106, arXiv:1411.1756

Gordon, M. A., Berkermann, U., Mezger, P. G., et al., Anatomy of the Sagittarius complex. 3: Morphology and characteristics of the SGR B2 giant molecular giant molecular cloud, A&A **280** (Dec. 1993) 208–220, ADS

Grimm, H.-J. 2003, PhD thesis, Ludwig-Maximilians-Universitat, Munchen

Grimm, H.-J., Gilfanov, M., & Sunyaev, R., The Milky Way in X-rays for an outside observer. Log(N)-Log(S) and luminosity function of X-ray binaries from RXTE/ASM data, A&A **391** (Sep. 2002) 923–944, astro-ph/0109239

Grimm, H.-J., Gilfanov, M., & Sunyaev, R., High-mass X-ray binaries as a star formation rate indicator in distant galaxies, MNRAS **339** (Mar. 2003) 793–809, arXiv:astro-ph/0205371

Gruber, D. E., Matteson, J. L., Peterson, L. E., & Jung, G. V., The Spectrum of Diffuse Cosmic Hard X-Rays Measured with HEAO 1, ApJ **520** (Jul. 1999) 124–129, astro-ph/9903492

Haardt, F. & Matt, G., X-ray polarization in the two-phase model for AGN and X-ray binaries, MNRAS **261** (Mar. 1993) 346–352, ADS

Harrison, F. A., Aird, J., Civano, F., et al., The NuSTAR Extragalactic Surveys: The Number Counts of Active Galactic Nuclei and the Resolved Fraction of the Cosmic X-ray Background, ArXiv e-prints (Nov. 2015), arXiv:1511.04183 [astro-ph.HE]

Harrison, F. A., Craig, W. W., Christensen, F. E., et al., The Nuclear Spectroscopic Telescope Array (NuSTAR) High-energy X-Ray Mission, ApJ **770** (Jun. 2013) 103, arXiv:1301.7307 [astro-ph.IM]

Hasegawa, T., Sato, F., Whiteoak, J. B., & Miyawaki, R., A large-scale cloud collision in the galactic center molecular cloud near Sagittarius B21, ApJ **429** (Jul. 1994) L77–L80

Hasinger, G., Miyaji, T., & Schmidt, M., Luminosity-dependent evolution of soft X-ray selected AGN. New Chandra and XMM-Newton surveys, A&A **441** (Oct. 2005) 417–434, astro-ph/0506118

Heitler, W. 1954, Quantum theory of radiation, , Dover Publications

Iben, Jr., I., Tutukov, A. V., & Yungelson, L. R., A Model of the Galactic X-Ray Binary Population. II. Low-Mass X-Ray Binaries in the Galactic Disk, ApJS **100** (Sep. 1995) 233

Illarionov, A. F. & Sunyaev, R. A., Why the Number of Galactic X-ray Stars Is so Small?, A&A **39** (Feb. 1975) 185, ADS

Illarionov, A. F. & Syunyaev, R. A., Compton Scattering by Thermal Electrons in X-Ray Sources., Soviet Ast. **16** (Aug. 1972) 45, ADS

Inui, T., Koyama, K., Matsumoto, H., & Tsuru, T. G., Time Variability of the Neutral Iron Lines from the Sagittarius B2 Region and Its Implication of a Past Outburst of Sagittarius A, PASJ **61** (Jan. 2009) 241, ADS

Iso, N., Ebisawa, K., & Tsujimoto, M., Intensity variation of the Fe K emission lines along the Galactic latitude, in American Institute of Physics Conference Series, Vol. 1427, American Institute of Physics Conference Series, ed. R. Petre, K. Mitsuda, & L. Angelini. 2012, 288–289

Jackson, J. M., Rathborne, J. M., Shah, R. Y., et al., The Boston University-Five College Radio Astronomy Observatory Galactic Ring Survey, ApJS **163** (Mar. 2006) 145–159, arXiv:astro-ph/0602160

Jahoda, K., Kouveliotou, C., Kallman, T. R., & Praxys Team, Polarization from Relativistic Astrophysical X-raY Sourses: The PRAXYS Small Explorer Observatory, in American Astronomical Society Meeting Abstracts, Vol. 225, American Astronomical Society Meeting Abstracts. 2015, 338.40, ADS

Jonker, P. G. & Nelemans, G., The distances to Galactic low-mass X-ray binaries: consequences for black hole luminosities and kicks, MNRAS **354** (Oct. 2004) 355–366, astro-ph/0407168

Kalberla, P. M. W., Burton, W. B., Hartmann, D., et al., The Leiden/Argentine/Bonn (LAB) Survey of Galactic HI. Final data release of the combined LDS and IAR surveys with improved stray-radiation corrections, A&A **440** (Sep. 2005) 775–782, arXiv:astro-ph/0504140

Kalberla, P. M. W. & Kerp, J., The Hi Distribution of the Milky Way, ARA&A **47** (Sep. 2009) 27–61

Kauffmann, J., Pillai, T., Shetty, R., Myers, P. C., & Goodman, A. A., The Mass-size Relation from Clouds to Cores. II. Solar Neighborhood Clouds, ApJ **716** (Jun. 2010) 433–445, arXiv:1004.1170 [astro-ph.GA]

Kent, S. M., Dame, T. M., & Fazio, G., Galactic structure from the Spacelab infrared telescope. II - Luminosity models of the Milky Way, ApJ **378** (Sep. 1991) 131–138

Kompaneets, A. S., Soviet Physics **4** (1957) 730

Könyves, V., André, P., Men'shchikov, A., et al., The Aquila prestellar core population revealed by Herschel, A&A **518** (Jul. 2010) L106, arXiv:1005.2981 [astro-ph.SR]

Koyama, K., Hyodo, Y., Inui, T., et al., Iron and Nickel Line Diagnostics for the Galactic Center Diffuse Emission, PASJ **59** (Jan. 2007) 245–255, astro-ph/0609215

Koyama, K., Kawada, M., Kunieda, H., Tawara, Y., & Takeuchi, Y., Is the 5-kpc Galactic arm a colony of X-ray pulsars?, Nature **343** (Jan. 1990) 148

Koyama, K., Maeda, Y., Sonobe, T., et al., ASCA View of Our Galactic Center: Remains of Past Activities in X-Rays?, PASJ **48** (Apr. 1996) 249–255

Koyama, K., Makishima, K., Tanaka, Y., & Tsunemi, H., Thermal X-ray emission with intense 6.7-keV iron line from the Galactic ridge, PASJ **38** (1986) 121–131, ADS

Krivonos, R., Revnivtsev, M., Churazov, E., et al., Hard X-ray emission from the Galactic ridge, A&A **463** (Mar. 2007) 957–967, astro-ph/0605420

Krivonos, R., Revnivtsev, M., Lutovinov, A., et al., INTEGRAL/IBIS all-sky survey in hard X-rays, A&A **475** (Nov. 2007) 775–784, astro-ph/0701836

Krivonos, R., Tsygankov, S., Lutovinov, A., et al., INTEGRAL/IBIS nine-year Galactic hard X-ray survey, A&A **545** (Sep. 2012) A27, arXiv:1205.3941 [astro-ph.IM]

Kruijssen, J. M. D., Longmore, S. N., Elmegreen, B. G., et al., What controls star formation in the central 500 pc of the Galaxy?, MNRAS **440** (Jun. 2014) 3370–3391, arXiv:1303.6286

Langer, W. D., Goldsmith, P. F., Pineda, J. L., et al., Ionized gas at the edge of the central molecular zone, A&A **576** (Apr. 2015) A1, arXiv:1501.06832

Larson, R. B., Turbulence and star formation in molecular clouds, MNRAS **194** (Mar. 1981) 809–826, ADS

Lehmer, B. D., Alexander, D. M., Bauer, F. E., et al., A Chandra Perspective on Galaxy-wide X-ray Binary Emission and its Correlation with Star Formation Rate and Stellar Mass: New Results from Luminous Infrared Galaxies, ApJ **724** (Nov. 2010) 559–571, arXiv:1009.3943 [astro-ph.CO]

Levine, E. S., Blitz, L., & Heiles, C., The Spiral Structure of the Outer Milky Way in Hydrogen, Science **312** (Jun. 2006) 1773–1777, astro-ph/0605728

Lis, D. C. & Goldsmith, P. F., Modeling of the continuum and molecular line emission from the Sagittarius B2 molecular cloud, ApJ **356** (Jun. 1990) 195–210

Liu, Q. Z., van Paradijs, J., & van den Heuvel, E. P. J., Catalogue of high-mass X-ray binaries in the Galaxy (4th edition), A&A **455** (Sep. 2006) 1165–1168, arXiv:0707.0549

Liu, Q. Z., van Paradijs, J., & van den Heuvel, E. P. J., A catalogue of low-mass X-ray binaries in the Galaxy, LMC, and SMC (Fourth edition), A&A **469** (Jul. 2007) 807–810, arXiv:0707.0544

Lodders, K., Solar System Abundances and Condensation Temperatures of the Elements, ApJ **591** (Jul. 2003) 1220–1247

Lombardi, M., Alves, J., & Lada, C. J., Larson's third law and the universality of molecular cloud structure, A&A **519** (Sep. 2010) L7, arXiv:1008.4251 [astro-ph.GA]

Lutovinov, A., Revnivtsev, M., Gilfanov, M., et al., INTEGRAL insight into the inner parts of the Galaxy. High mass X-ray binaries, A&A **444** (Dec. 2005) 821–829, astro-ph/0411550

Lutovinov, A. A., Revnivtsev, M. G., Tsygankov, S. S., & Krivonos, R. A., Population of persistent high-mass X-ray binaries in the Milky Way, MNRAS **431** (May 2013) 327–341, arXiv:1302.0728 [astro-ph.HE]

Marin, F., X-ray Polarimetry - a Tool for the Galactic center diagnosis, ArXiv e-prints (Aug. 2015), arXiv:1508.00405 [astro-ph.HE]

Marin, F., Karas, V., Kunneriath, D., & Muleri, F., Prospects of 3D mapping of the Galactic Centre clouds with X-ray polarimetry, MNRAS **441** (Jul. 2014) 3170–3176, arXiv:1405.0898

Marin, F., Karas, V., Kunneriath, D., Muleri, F., & Soffitta, P., Probing the Galactic center with X-ray polarimetry, in SF2A-2014: Proceedings of the Annual meeting of the French Society of Astronomy and Astrophysics, ed. J. Ballet, F. Martins, F. Bournaud, R. Monier, & C. Reylé. 2014b, 109–112, arXiv:1408.0354 [astro-ph.HE]

Marin, F., Muleri, F., Soffitta, P., Karas, V., & Kunneriath, D., Reflection nebulae in the Galactic center: soft X-ray imaging polarimetry, A&A **576** (Apr. 2015) A19, arXiv:1502.04894

Markwardt, C. B., Strohmayer, T. E., & Swank, J. H., XTE J1810-189 is a Neutron Star, The Astronomer's Telegram **1443** (Mar. 2008) 1, ADS

McClure-Griffiths, N. M., Pisano, D. J., Calabretta, M. R., et al., Gass: The Parkes Galactic All-Sky Survey. I. Survey Description, Goals, and Initial Data Release, ApJS **181** (Apr. 2009) 398–412, arXiv:0901.1159 [astro-ph.GA]

McKee, C. F. & Ostriker, E. C., Theory of Star Formation, ARA&A **45** (Sep. 2007) 565–687, arXiv:0707.3514

McKee, C. F. & Ostriker, J. P., A theory of the interstellar medium - Three components regulated by supernova explosions in an inhomogeneous substrate, ApJ **218** (Nov. 1977) 148–169

McKee, C. F. & Williams, J. P., The Luminosity Function of OB Associations in the Galaxy, ApJ **476** (Feb. 1997) 144–165, ADS

McMillan, P. J., Mass models of the Milky Way, MNRAS **414** (Jul. 2011) 2446–2457, arXiv:1102.4340 [astro-ph.GA]

Meagher, D., Octree Encoding: A New Technique for the Representation, Manipulation and Display of Arbitrary 3-D Objects by Computer, Technical Report IPL-TR-80-11 I (Oct. 1980)

Meszaros, P., Novick, R., Szentgyorgyi, A., Chanan, G. A., & Weisskopf, M. C., Astrophysical implications and observational prospects of X-ray polarimetry, ApJ **324** (Jan. 1988) 1056–1067

Mineo, S., Gilfanov, M., Lehmer, B. D., Morrison, G. E., & Sunyaev, R., X-ray emission from star-forming galaxies - III. Calibration of the L_X-SFR relation up to redshift z $\approx$ 1.3, MNRAS **437** (Jan. 2014) 1698–1707, arXiv:1207.2157 [astro-ph.HE]

Mineo, S., Gilfanov, M., & Sunyaev, R., X-ray emission from star-forming galaxies - I. High-mass X-ray binaries, MNRAS **419** (Jan. 2012) 2095–2115, arXiv:1105.4610 [astro-ph.HE]

Misiriotis, A., Xilouris, E. M., Papamastorakis, J., Boumis, P., & Goudis, C. D., The distribution of the ISM in the Milky Way. A three-dimensional large-scale model, A&A **459** (Nov. 2006) 113–123, astro-ph/0607638

Molaro, M., Khatri, R., & Sunyaev, R., Probing the clumping structure of Giant Molecular Clouds through the spectrum, polarisation and morphology of X-ray Reflection Nebulae, ArXiv e-prints (Nov. 2015), arXiv:1511.05125 [astro-ph.HE], Accepted by A&A(14/06/2015)

Molaro, M., Khatri, R., & Sunyaev, R. A., A thin diffuse component of the Galactic ridge X-ray emission and heating of the interstellar medium contributed by the radiation of Galactic X-ray binaries, A&A **564** (Apr. 2014) A107, arXiv:1312.7029 [astro-ph.HE]

Morihana, K., An X-ray and Near-Infrared Study of the Galactic Ridge X-ray Emission, PASP **124** (Oct. 2012) 1132–1132

Morihana, K., Tsujimoto, M., Yoshida, T., & Ebisawa, K., X-Ray Point-source Populations Constituting the Galactic Ridge X-Ray Emission, ApJ **766** (Mar. 2013) 14, arXiv:1301.6856 [astro-ph.HE]

Morrison, R. & McCammon, D., Interstellar photoelectric absorption cross sections, 0.03-10 keV, ApJ **270** (Jul. 1983) 119–122

Motte, F., Andre, P., & Neri, R., The initial conditions of star formation in the rho Ophiuchi main cloud: wide-field millimeter continuum mapping, A&A **336** (Aug. 1998) 150–172, ADS

Muno, M. P., Baganoff, F. K., Bautz, M. W., et al., Diffuse X-Ray Emission in a Deep Chandra Image of the Galactic Center, ApJ **613** (Sep. 2004) 326–342, astro-ph/0402087

Muno, M. P., Baganoff, F. K., Brandt, W. N., Park, S., & Morris, M. R., Discovery of Variable Iron Fluorescence from Reflection Nebulae in the Galactic Center, ApJ **656** (Feb. 2007) L69–L72, arXiv:astro-ph/0611651

Murakami, H., Koyama, K., Sakano, M., Tsujimoto, M., & Maeda, Y., ASCA Observations of the Sagittarius B2 Cloud: An X-Ray Reflection Nebula, ApJ **534** (May 2000) 283–290, astro-ph/9908229

Murakami, H., Koyama, K., Tsujimoto, M., Maeda, Y., & Sakano, M., ASCA Discovery of Diffuse 6.4 KEV Emission near the Sagittarius C Complex: A New X-Ray Reflection Nebula, ApJ **550** (Mar. 2001) 297–300, astro-ph/0012310

Namito, Y., Ban, S., & Hirayama, H., Implementation of linearly-polarized photon scattering into the EGS4 code, Nuclear Instruments and Methods in Physics Research A **332** (Jul. 1993) 277–283

Narayan, R., Mahadevan, R., Grindlay, J. E., Popham, R. G., & Gammie, C., Advection-dominated accretion model of Sagittarius A*: evidence for a black hole at the Galactic center., ApJ **492** (Jan. 1998) 554–568, astro-ph/9706112

Negueruela, I., Roche, P., Fabregat, J., & Coe, M. J., The Be/X-ray transient V0332+53: evidence for a tilt between the orbit and the equatorial plane?, MNRAS **307** (Aug. 1999) 695–702, astro-ph/9903228

Nobukawa, M., Ryu, S. G., Tsuru, T. G., & Koyama, K., New Evidence for High Activity of the Supermassive Black Hole in our Galaxy, ApJ **739** (Oct. 2011) L52, arXiv:1109.1950 [astro-ph.HE]

Nowak, M. A., Neilsen, J., Markoff, S. B., et al., Chandra/HETGS Observations of the Brightest Flare Seen from Sgr A*, ApJ **759** (Nov. 2012) 95, arXiv:1209.6354 [astro-ph.HE]

Nutter, D. & Ward-Thompson, D., A SCUBA survey of Orion - the low-mass end of the core mass function, MNRAS **374** (Feb. 2007) 1413–1420, astro-ph/0611164

Odaka, H., Aharonian, F., Watanabe, S., et al., X-Ray Diagnostics of Giant Molecular Clouds in the Galactic Center Region and Past Activity of Sgr A*, ApJ **740** (Oct. 2011) 103, arXiv:1110.1936 [astro-ph.GA]

Overbeck, J. W., Small-Angle Scattering of Celestial X-Rays by Interstellar Grains., ApJ **141** (Apr. 1965) 864

Parsons, H., Thompson, M. A., Clark, J. S., & Chrysostomou, A., Molecular clumps in the W51 giant molecular cloud, MNRAS **424** (Aug. 2012) 1658–1671

Pavlinsky, M., Sunyaev, R., Churazov, E., et al., Spectrum-Roentgen-Gamma astrophysical mission, in Society of Photo-Optical Instrumentation Engineers (SPIE) Conference Series, Vol. 7011, Society of Photo-Optical Instrumentation Engineers (SPIE) Conference Series. 2008

Persic, M. & Rephaeli, Y., Galactic star formation rates gauged by stellar end-products, A&A **463** (Feb. 2007) 481–492, arXiv:astro-ph/0610321

Pikel'Ner, S. B., Heating of the Interstellar Gas by Subcosmic Rays, and the Formation of Clouds., Soviet Ast. **11** (Apr. 1968) 737, ADS

Ponti, G., Morris, M. R., Clavel, M., et al., On the past activity of Sgr A*, in IAU Symposium, Vol. 303, IAU Symposium, ed. L. O. Sjouwerman, C. C. Lang, & J. Ott. 2014, 333–343

Ponti, G., Morris, M. R., Terrier, R., & Goldwurm, A., Traces of Past Activity in the Galactic Centre, in Advances in Solid State Physics, Vol. 34, Cosmic Rays in Star-Forming Environments, ed. D. F. Torres & O. Reimer. 2013, 331, arXiv:1210.3034 [astro-ph.GA]

Ponti, G., Terrier, R., Goldwurm, A., Belanger, G., & Trap, G., Discovery of a Superluminal Fe K Echo at the Galactic Center: The Glorious Past of Sgr A* Preserved by Molecular Clouds, ApJ **714** (May 2010) 732–747, arXiv:1003.2001 [astro-ph.HE]

Porquet, D., Grosso, N., Predehl, P., et al., X-ray hiccups from Sagittarius A* observed by XMM-Newton. The second brightest flare and three moderate flares caught in half a day, A&A **488** (Sep. 2008) 549–557, arXiv:0806.4088

Porquet, D., Predehl, P., Aschenbach, B., et al., XMM-Newton observation of the brightest X-ray flare detected so far from Sgr A*, A&A **407** (Aug. 2003) L17–L20, astro-ph/0307110

Porquet, D., Rodriguez, J., Corbel, S., et al., XMM-Newton study of the persistent X-ray source 1E 1743.1-2843 located in the Galactic Center direction, A&A **406** (Jul. 2003) 299–304, astro-ph/0305489

Poutanen, J. & Vilhu, O., Compton scattering of polarized light in two-phase accretion discs, A&A **275** (Aug. 1993) 337, ADS

Pozdnyakov, L. A., Sobol, I. M., & Syunyaev, R. A., Comptonization and the shaping of X-ray source spectra - Monte Carlo calculations, Astrophysics and Space Physics Reviews **2** (1983) 189–331, ADS

Predehl, P. & Schmitt, J. H. M. M., X-raying the interstellar medium: ROSAT observations of dust scattering halos., A&A **293** (Jan. 1995), ADS

Qin, S.-L., Schilke, P., Rolffs, R., et al., Submillimeter continuum observations of Sagittarius B2 at subarcsecond spatial resolution, A&A **530** (Jun. 2011) L9, arXiv:1105.0344 [astro-ph.SR]

Ranalli, P., Comastri, A., & Setti, G., The 2-10 keV luminosity as a Star Formation Rate indicator, A&A **399** (Feb. 2003) 39–50, arXiv:astro-ph/0211304

Rathborne, J. M., Johnson, A. M., Jackson, J. M., Shah, R. Y., & Simon, R., Molecular Clouds and Clumps in the Boston University-Five College Radio Astronomy Observatory Galactic Ring Survey, ApJS **182** (May 2009) 131–142, arXiv:0904.1217 [astro-ph.SR]

Reig, P., Be/X-ray binaries, Ap&SS **332** (Mar. 2011) 1–29, arXiv:1101.5036 [astro-ph.HE]

Revnivtsev, M., Distribution of the Galactic bulge emission at —b—¿2^o according to the RXTE Galactic Center scans, A&A **410** (Nov. 2003) 865–870, astro-ph/0304351

Revnivtsev, M., Sazonov, S., Churazov, E., et al., Discrete sources as the origin of the Galactic X-ray ridge emission, Nature **458** (Apr. 2009) 1142–1144, arXiv:0904.4649 [astro-ph.GA]

Revnivtsev, M., Sazonov, S., Gilfanov, M., Churazov, E., & Sunyaev, R., Origin of the Galactic ridge X-ray emission, A&A **452** (Jun. 2006) 169–178

Revnivtsev, M. G., Churazov, E. M., Sazonov, S. Y., et al., Hard X-ray view of the past activity of Sgr A* in a natural Compton mirror, A&A **425** (Oct. 2004) L49–L52, astro-ph/0408190

Rieke, G. H. & Lebofsky, M. J., The interstellar extinction law from 1 to 13 microns, ApJ **288** (Jan. 1985) 618–621

Ritter, H. & Kolb, U., Catalogue of cataclysmic binaries, low-mass X-ray binaries and related objects (Seventh edition), A&A **404** (Jun. 2003) 301–303, astro-ph/0301444

Robitaille, T. P. & Whitney, B. A., The Present-Day Star Formation Rate of the Milky Way Determined from Spitzer-Detected Young Stellar Objects, ApJ **710** (Feb. 2010) L11–L15, arXiv:1001.3672 [astro-ph.GA]

Rolf, D. P., Evidence for the detection of X-ray scattering from interstellar dust grains, Nature **302** (Mar. 1983) 46–48

Roman-Duval, J., Jackson, J. M., Heyer, M., et al., Kinematic Distances to Molecular Clouds Identified in the Galactic Ring Survey, ApJ **699** (Jul. 2009) 1153–1170, arXiv:0905.0723 [astro-ph.GA]

Roman-Duval, J., Jackson, J. M., Heyer, M., Rathborne, J., & Simon, R., Physical Properties and Galactic Distribution of Molecular Clouds Identified in the Galactic Ring Survey, ApJ **723** (Nov. 2010) 492–507, arXiv:1010.2798 [astro-ph.GA]

Rybicki, G. B. & Lightman, A. P. 1986, Radiative Processes in Astrophysics, , Wiley-VCH

Salpeter, E. E., The Luminosity Function and Stellar Evolution., ApJ **121** (Jan. 1955) 161

Sazonov, S., Revnivtsev, M., Gilfanov, M., Churazov, E., & Sunyaev, R., X-ray luminosity function of faint point sources in the Milky Way, A&A **450** (Apr. 2006) 117–128, astro-ph/0510049

Schoonjans, T., Brunetti, A., Golosio, B., et al., Spectromchimica Acta Part B: Atomic Spectroscopy **66** (2011) 776–784

Shetty, R., Collins, D. C., Kauffmann, J., et al., The Effect of Projection on Derived Mass-Size and Linewidth-Size Relationships, ApJ **712** (Apr. 2010) 1049–1056, arXiv:1001.4549

Shtykovskiy, P. E. & Gilfanov, M. R., High-mass X-ray binaries and recent star formation history of the Small Magellanic Cloud, Astronomy Letters **33** (Jul. 2007) 437–454, arXiv:0710.3059

Shull, J. M. & van Steenberg, M. E., X-ray secondary heating and ionization in quasar emission-line clouds, ApJ **298** (Nov. 1985) 268–274

Sidoli, L., Mereghetti, S., Israel, G. L., et al., The Zoo of X-Ray Sources in the Galactic Center Region: Observations with BEPPOSAX, ApJ **525** (Nov. 1999) 215–227, astro-ph/9904393

Snow, T. P. & McCall, B. J., Diffuse Atomic and Molecular Clouds, ARA&A **44** (Sep. 2006) 367–414

Soffitta, P., Barcons, X., Bellazzini, R., et al., XIPE: the X-ray imaging polarimetry explorer, Experimental Astronomy **36** (Dec. 2013) 523–567, arXiv:1309.6995 [astro-ph.HE]

Spitzer, L. 1978, Physical processes in the interstellar medium, , Wiley-VCH

Stecker, F. W., Solomon, P. M., Scoville, N. Z., & Ryter, C. E., Molecular hydrogen in the Galaxy and galactic gamma rays, ApJ **201** (Oct. 1975) 90–97

Sugizaki, M., Matsuzaki, K., Kaneda, H., Yamauchi, S., & Mitsuda, K., The population of faint X-ray sources in the galaxy and their contribution to the galactic ridge X-ray emission, X-ray Astronomy: Stellar Endpoints, AGN, and the Diffuse X-ray Background **599** (Dec. 2001) 959–962

Sunyaev, R. & Churazov, E., Equivalent width, shape and proper motion of the iron fluorescent line emission from molecular clouds as an indicator of the illuminating source X-ray flux history, MNRAS **297** (Jul. 1998) 1279–1291, astro-ph/9805038

Sunyaev, R., Gilfanov, M., & Churazov, E., The 6.4 keV fluorescent emission from the Galactic Center molecular clouds, in Highlights in X-ray Astronomy, ed. B. Aschenbach & M. J. Freyberg, Vol. 272. 1999a, 102, ADS

Sunyaev, R. A. & Churazov, E. M., Scattering of X-ray emission lines by neutral and molecular hydrogen in the solar atmosphere and in the vicinity of active galactic nuclei and compact X-ray sources, Astronomy Letters **22** (Sep. 1996) 648–663, astro-ph/9608114

Sunyaev, R. A., Markevitch, M., & Pavlinsky, M., The center of the Galaxy in the recent past - A view from GRANAT, ApJ **407** (Apr. 1993) 606–610

Sunyaev, R. A., Uskov, D. B., & Churazov, E. M., Scattering of x-ray emission lines by molecular hydrogen, Astronomy Letters **25** (Apr. 1999) 199–205, ADS

Szymanski, H. 1970, Raman Spectroscopy: Theory and Practice, 1st edn., Vol. 2, Plenum Press, Donington House, 30 Norfolk Street, London, WC2, England

Tajima, H., Blandford, R., Enoto, T., et al., Soft gamma-ray detector for the ASTRO-H Mission, in Society of Photo-Optical Instrumentation Engineers (SPIE) Conference Series, Vol. 7732, Society of Photo-Optical Instrumentation Engineers (SPIE) Conference Series. 2010, 773216, arXiv:1010.4997 [astro-ph.IM]

Takahashi, T., Mitsuda, K., & Kelley, R., The ASTRO-H Mission, X-ray Astronomy 2009; Present Status, Multi-Wavelength Approach and Future Perspectives **1248** (Jul. 2010) 537–542

Tanaka, Y., ASCA observation of X-ray emission from the Galactic ridge, A&A **382** (Feb. 2002) 1052–1060

Tanaka, Y., Inoue, H., & Holt, S. S., The X-ray astronomy satellite ASCA, PASJ **46** (Jun. 1994) L37–L41, ADS

Tanaka, Y., Miyaji, T., & Hasinger, G., Origin of the Galactic ridge X-ray emission, Astronomische Nachrichten **320** (1999) 181, ADS

Taverna, R., Muleri, F., Turolla, R., et al., Probing magnetar magnetosphere through X-ray polarization measurements, MNRAS **438** (Feb. 2014) 1686–1697, arXiv:1311.7500 [astro-ph.HE]

Terrier, R., Ponti, G., Bélanger, G., et al., Fading Hard X-ray Emission from the Galactic Center Molecular Cloud Sgr B2, ApJ **719** (Aug. 2010) 143–150, arXiv:1005.4807 [astro-ph.HE]

Trümper, J. & Schönfelder, V., Distance Determination of Variable X-ray Sources, A&A **25** (Jun. 1973) 445, ADS

Tsuboi, M. & Miyazaki, A., Statistical Properties of Molecular Clumps in the Galactic Center 50 km s^{-1} Molecular Cloud, PASJ **64** (Oct. 2012) 111, arXiv:1204.5535

Tutukov, A. V., Fedorova, A. V., Ergma, E. V., & Yungelson, L. R., The evolutionary status of MXB 1820-30 and other short-period low-mass X-ray sources, Soviet Astronomy Letters **13** (Oct. 1987) 328, ADS

Uchiyama, H., Nobukawa, M., Tsuru, T. G., & Koyama, K., K-Shell Line Distribution of Heavy Elements along the Galactic Plane Observed with Suzaku, PASJ **65** (Feb. 2013) 19, arXiv:1209.0067 [astro-ph.HE]

Ueda, Y., Akiyama, M., Ohta, K., & Miyaji, T., Cosmological Evolution of the Hard X-Ray Active Galactic Nucleus Luminosity Function and the Origin of the Hard X-Ray Background, ApJ **598** (Dec. 2003) 886–908, astro-ph/0308140

Vainshtein, L. A., Syunyaev, R. A., & Churazov, E. M., Scattering of X-ray emission lines by atomic helium, Astronomy Letters **24** (May 1998) 271–276, astro-ph/9801202

Valinia, A., Tatischeff, V., Arnaud, K., Ebisawa, K., & Ramaty, R., On the Origin of the Iron K Line in the Spectrum of The Galactic X-Ray Background, ApJ **543** (Nov. 2000) 733–739, astro-ph/0006202

Vallee, J. P., The Milky Way's Spiral Arms Traced by Magnetic Fields, Dust, Gas, and Stars, ApJ **454** (Nov. 1995) 119

Vallée, J. P., New Velocimetry and Revised Cartography of the Spiral Arms in the Milky WAY - A Consistent Symbiosis, AJ **135** (Apr. 2008) 1301–1310

van Paradijs, J. & White, N., The Galactic Distribution of Low-Mass X-Ray Binaries, ApJ **447** (Jul. 1995) L33

Verner, D. A. & Yakovlev, D. G., Analytic FITS for partial photoionization cross sections., A&AS **109** (Jan. 1995) 125–133, ADS

Wang, Z., Shen, Z., Mu, B., et al., Development of the x-ray timing and polarization telescope optics, in Society of Photo-Optical Instrumentation Engineers (SPIE) Conference Series, Vol. 9144, Society of Photo-Optical Instrumentation Engineers (SPIE) Conference Series. 2014, 1

Warwick, R. S., Low-luminosity X-ray sources and the Galactic ridge X-ray emission, MNRAS **445** (Nov. 2014) 66–80, arXiv:1409.0747 [astro-ph.HE]

Weisskopf, M. C., Bellazzini, R., Costa, E., et al., Transforming Our Understanding of the X-ray Universe: The Imaging X-ray Polarimeter Explorer (IXPE), in AAS/High Energy Astrophysics Division, Vol. 14, AAS/High Energy Astrophysics Division. 2014, 116.15, ADS

Weisskopf, M. C., Gaskin, J., Tananbaum, H., & Vikhlinin, A., Beyond Chandra: the x-ray Surveyor, in Society of Photo-Optical Instrumentation Engineers (SPIE) Conference Series, Vol. 9510, Society of Photo-Optical Instrumentation Engineers (SPIE) Conference Series. 2015, 2, arXiv:1505.00814 [astro-ph.IM]

White, N. E. & van Paradijs, J., The Galactic Distribution of Black Hole Candidates in Low Mass X-ray Binary Systems, ApJ **473** (Dec. 1996) L25

Williams, J., The Structure of Molecular Clouds: are they Fractal?, in Interstellar Turbulence, ed. J. Franco & A. Carraminana. 1999, 190, ADS

Williams, J. P., Blitz, L., & McKee, C. F., The Structure and Evolution of Molecular Clouds: from Clumps to Cores to the IMF, Protostars and Planets IV (May 2000) 97, astro-ph/9902246

Wolfire, M. G., Hollenbach, D., McKee, C. F., Tielens, A. G. G. M., & Bakes, E. L. O., The neutral atomic phases of the interstellar medium, ApJ **443** (Apr. 1995) 152–168

Wolfire, M. G., McKee, C. F., Hollenbach, D., & Tielens, A. G. G. M., Neutral Atomic Phases of the Interstellar Medium in the Galaxy, ApJ **587** (Apr. 2003) 278–311, astro-ph/0207098

Worrall, D. M., Marshall, F. E., Boldt, E. A., & Swank, J. H., HEAO 1 measurements of the galactic ridge, ApJ **255** (Apr. 1982) 111–121

Yusef-Zadeh, F., The Consequences of the Interaction of Cosmic Rays with Galactic Center Molecular Clouds, in Astrophysics and Space Science Proceedings, Vol. 34, Cosmic Rays in Star-Forming Environments, ed. D. F. Torres & O. Reimer. 2013, 325

Yusef-Zadeh, F., Law, C., & Wardle, M., The Origin of X-Ray Emission from a Galactic Center Molecular Cloud: Low-Energy Cosmic-Ray Electrons, ApJ **568** (Apr. 2002) L121–L125, astro-ph/0202442

Zeldovich, Y. B. & Sunyaev, R. A., The Interaction of Matter and Radiation in a Hot-Model Universe, Ap&SS **4** (Jul. 1969) 301–316

Zhang, S., Hailey, C. J., Mori, K., et al., Hard X-ray Morphological and Spectral Studies of The Galactic Center Molecular Cloud Sgr B2: Constraining Past Sgr A* Flaring Activity, ArXiv e-prints (Jul. 2015), arXiv:1507.08740 [astro-ph.HE]

Acknowledgements

I would like to thank my supervisor, Rashid Sunyaev, for giving me the opportunity to do my PhD at MPA, and for his unparalleled energy and enthusiasm, which have constantly supported me in my work. I am greatly indebted to Rishi Khatri for his constant and priceless support throughout my entire PhD, and for his infinite patience in giving me all the explanations I needed. Thank you also to others in the High Energy Astrophysics group, in particular Eugene Churazov, for always being available for discussions.

I would also like to thank my family, Rob and my friends for always giving me all the support I needed to complete this thesis, and for bearing with during my most unbearable moments.